NUMERICAL MODELING OF MICROSCALE PLASMA ACTUATORS

By

CHIN-CHENG WANG

A DISSERTATION PRESENTED TO THE GRADUATE SCHOOL
OF THE UNIVERSITY OF FLORIDA IN PARTIAL FULFILLMENT
OF THE REQUIREMENTS FOR THE DEGREE OF
DOCTOR OF PHILOSOPHY

UNIVERSITY OF FLORIDA

2009

To my parents and all my teachers

ACKNOWLEDGMENTS

I would like to thank my advisor, Professor Subrata Roy, for his continued support, guidance, and encouragement throughout my doctoral study. He always provided me insightful physics and numerical understanding when I was struggling for research. Thanks for giving me this opportunity to prove my research ability.

I would also like to express my appreciation to my committee members: Professor David W. Hahn, Professor Renwei Mei, and Professor Susan B. Sinnott for guiding directions and providing useful suggestions on my dissertation.

I am grateful to Dr. John Schmisseur, Air Force Of Scientific Research, Dr. Datta V. Gaitonde, Dr. Miguel R. Visbal, and Air Force Research Laboratory for supporting my study. I also thank the former and current members of the Applied Physics Research Group (APRG) and the Computational Plasma Dynamics Laboratory and Test Facility (CPDLT): Richard, Dr. Singh, Ankush, Navya, Ryan, Matt, and Tomas for all their friendship and cooperation.

I wish to thank Dr. Ming-Jyh Chern, former advisor, mentor and teacher, for his training when I was a master student. I am greatly thankful to my parents, brother, and relatives for their constant support during my studies.

TABLE OF CONTENTS

LIST OF TABLES

LIST OF FIGURES

LIST OF ABBREVIATIONS

A	Preexponential constant of Townsend coefficient ($cm^{-1}Torr^{-1}$)
B	Exponential constant of Townsend coefficient (V/ cmTorr)
C	Scaling factor
c	Speed of sound (m/s)
c_p	Specific heat (J/kgK)
D_e	Electron diffusion coefficient (cm^2/s)
D_i	Ion diffusion coefficient (cm^2/s)
d	Circular pipe diameter (mm)
d_g	Gap between electrodes in vertical direction (m)
d_l	Reference length (m)
E	Electric field (V/m)
e	Elementary charge (C)
e^-	Electron particle
F	Electric force density (N/m^3)
k	Turbulent kinetic energy (m^2/s^2)
k_B	Boltzmann's constant (J/K)
k_c	Thermal conductivity (W/mK)
L	Characteristic length (m)
M	Blowing ratio
M_n	Neutral particle
m_i	Ion mass (kg)
N_e	Normalized electron density
N_i	Normalized ion density
n^+	Positive ion particle

n^-	Negative ion particle
n_e	Electron density (m^{-3})
n_i	Ion density (m^{-3})
p	Pressure (Torr)
Q	Volume flow rate (ml/min)
q	Charge density n_i-n_e (m^{-3})
r	Electron-ion recombination rate (cm^3/s)
T_e	Electron temperature (K)
T_{fs}	Freestream gas temperature (K)
T_i	Ion temperature (K)
T_j	Cooling jet temperature (K)
T_s	Work surface temperature (K)
V	Characteristic velocity (m/s)
V_b	Bohm velocity (m/s)
V_{fs}	Freestream velocity (m/s)
V_j	Cooling jet velocity (m/s)
V_n	Gas velocity (m/s)
V_n'	Fluctuation velocity (m/s)
$\overline{V_n}$	Mean velocity (m/s)
w	Weighted basis function
α	Townsend coefficient (cm^{-1})
α_a	Jet issuing angle
α_c	Collision efficiency
ε	Turbulent dissipation (m^2/s^2)

ε_0	Vacuum permittivity (Farad/m)
ε_d	Dielectric constant (Farad/m)
ϕ	Potential (V)
Γ_e	Electron flux ($m^{-2}s^{-1}$)
η	Film cooling effectiveness
Λ	Macroscopic characteristic length (m)
Λ_f	Amplitude of actuation force density (kN/m^3)
λ	Mean free path (m)
λ_D	Debye length (m)
μ	Dynamic viscosity (kg/ms)
μ_e	Electron mobility (cm^2/sV)
μ_i	Ion mobility (cm^2/sV)
ρ	Fluid density (kg/m^3)
ρ_{fs}	Freestream gas density (kg/m^3)
ρ_j	Cooling jet density (kg/m^3)
σ	Stress tensor (N/m^2)
σ_T	Thermal accommodation coefficient
σ_V	Momentum accommodation coefficient
ξ	Frequency (Hz)

Abstract of Dissertation Presented to the Graduate School
of the University of Florida in Partial Fulfillment of the
Requirements for the Degree of Doctor of Philosophy

NUMERICAL MODELING OF MICROSCALE PLASMA ACTUATOR

By

Chin-Cheng Wang

December 2009

Chair: Subrata Roy
Major: Mechanical Engineering

We present the study of the dielectric barrier discharge (DBD) plasma actuator for both macro and microscale applications. Such actuators create a stable glow discharge at atmospheric pressures and generate cold plasmas and electrohydrodynamic (EHD) force that impart directed momentum to the surrounding fluid. There are phenomenological and physics based reduced order numerical models available for predicting these forces at macroscale. In microscale the physical model is not known. This research covers problems of two distinct spatial scales.

At macroscale, we apply plasmas for mitigating heat transfer problem in gas turbines. Specifically, novel film cooling concepts of turbine blades are investigated using plasma discharge. A phenomenological approach is utilized for modeling the local body force generated by plasmas. An active three-dimensional plasma actuation is predicted for different cooling hole geometries. Such an approach utilizes the EHD force which attaches the cold jet to the work surface by actively altering the body force in the vicinity of an actuator. Results show above 100% improvement of film cooling effectiveness over the standard baseline design.

Also at macroscale, we study the physics of plasma induced bulk flow control using first-principles based reduced order force model. We introduce two novel designs of horseshoe and serpentine actuators, and both designs have zero net mass flux (ZNMF). These actuators show

active modification of the boundary layer thickness suitable for flow separation control and flow turbulization using the same actuator.

The primary weakness of DBD actuators is the relatively small actuation effect as characterized by the induced flow velocity. To improve upon this weakness for high speed flow control, the microscale discharge may be a remedy for increasing electric force.

We study the physics of microscale plasma actuation using the high-fidelity finite-element procedure which is anchored in a Multi-scale Ionized Gas (MIG) flow code. First, a two-dimensional volume discharge with nitrogen as working gas is investigated using a first-principles approach solving coupled system of hydrodynamic plasma equations and Poisson equation for ion density, electron density, and electric field distribution. The quasi-neutral plasma ($N_i \approx N_e$) region and the sheath ($N_i >> N_e$) region are identified. As one approaches the sheath edge, there is an abrupt drop in the charge difference and sharp increase in electric field strength. By decreasing the gap between electrodes, the sheath becomes dominant in the plasma region. Based on the simulation results, we have deeper insight into the microscale force generation mechanism through understanding the physics at microscale. Subsequently, we investigate a novel first generation micro plasma pump using the same microscale hydrodynamic plasma model. We find the average flow rate is around 28.5 ml/min for micro plasma pump. Such micro plasma pumps may become useful in a wide range of applications from microbiology to space exploration and cooling of microelectronic devices.

In order to improve the performance of micro plasma pumps in real world applications, a three-dimension plasma simulation is needed. We introduce a flow shaping mechanism using surface compliant microscale gas discharge. For the case of quiescent flow, horseshoe plasma

actuator creates an inward and downward electric force to pinch and eject fluid normal to the plane of the actuator.

We extend our two-dimensional hydrodynamic model into the two-species three-dimensional DC plasma simulation to study two cases of micro plasma pumps. Both plasma governing equations and Navier-Stokes equations are solved using a three-dimensional finite element based MIG flow code. The results show the highest charge separation and electric force close to the powered electrodes. We find three vortical structures inside the pump which can not be found in our two-dimensional simulation. To reduce the vortices inside the micro plasma pump, the location of the actuators and the input voltage may be key factors. The three-dimensional flow simulation at 5 Torr predicts an order of magnitude lower flow rate than that predicted earlier of two-dimensional micro plasma pump simulation for atmospheric condition. The predicted flow rate in Case#2 (Q_2 = 1.5 ml/min) is two times higher than that in Case#1 (Q_1 = 0.63 ml/min). Such flow rates are one order of magnitude higher than that previously reported data for the same level of input voltage and may be quite useful for a range of practical applications.

In the future, the numerical results will be compared with reported experimental data or other numerical work. Preliminary three-dimensional formulations have been implemented in the MIG environment for simulating simple flow actuation problems. Also, the computational speed is improved from one week to one day for a fine mesh (~300,000 elements). However, the challenge is the limited memory per node on the High Performance Center (HPC) at the University of Florida when I want to run a case of over 1,000,000 elements. Parallel computation could considerably share work loading on different nodes to conduct real physical problems.

CHAPTER 1
INTRODUCTION

The solid state becomes a liquid state as the temperature increase, and liquid state becomes a gas state as the temperature further increase. Plasma is formed by additional energy added to the gas. The energy could be heat, electric field, or magnetic field. At a sufficiently high temperature (energy), the atoms in the gas start to decompose into charged particles (ions and electrons), and this state is often called the *fourth state of matter*.

In the early 19th century, people knew how to use plasma to generate ozone. In the past few decades, plasma has been used for many applications. For example, it has been used as thin film deposition for the semiconductor industries, in fluorescent lamps for the lighting systems, in televisions for the display systems, in sterilization for health and medical purposes, in thrusters for propulsive mechanism, and airfoil drag reduction for the aerospace industries. The possibility of using plasma in aerodynamic applications such as flow separation control and flow turbulization is also an exciting one. Our purpose is to explore this avenue further. We will focus specifically on dielectric barrier discharge (DBD) based plasma actuators.

1.1 Physics of Plasma

1.1.1 Ionization and Recombination

Ionization is the process of the electron which is removed or added from a neutral atom or molecule by external energy. When an electron e^- knocks a neutral particle M_n, the ionization process occurs. The resultant positively charged particle is an ion n^+. For plasma DBD actuators, when we apply a high potential between electrodes, the ions are generated by electron-gas collisions, and this process is also called impact ionization. The plasma is sustained by collision with high energy electrons which can force electrons out of the shell of atoms. It may also pass their energy to other electrons thus ionization.

In classical mechanics, passing the electron through a potential barrier would be impossible without sufficient energy. However, in quantum mechanics for few micron gaps between electrodes, there is a probability to drive a discharge without sufficient external energy, and it is called quantum ionization or quantum tunneling of electrons effect.

Recombination is the reverse process of ionization. In this process, an ion n^+ recombines with an electron e^- as a result of a neutral particle M_n.

1.1.2 Secondary Emission

This is a process of new electrons are generated by electrons or ions bombardment. The electron enters the ground state of atom, and a second electron absorbs excess energy of neutralization. This mechanism is called Auger neutralization [1]. The secondary electrons are emitted from the cathode is an important process in sustaining a discharge. It is also called self-sustained discharge when plasma flows even in the absence of electrons from additional energy. Ions bombardment of cathode is also causing secondary emission and plays an important role in gas discharges.

1.1.3 Sheath

The sheath is one of the most important parameters in the physics of plasma actuator. Langmuir is the first one to explain this phenomenon in literature [2]. He described that there were sheaths containing very few electrons near the electrodes ($n_i >> n_e$), and the ionized gas which is quasi-neutral contains ions and electrons in about equal numbers ($n_i \approx n_e$). The definition of the sheath boundary can be assumed Bohm criterion, i.e. Bohm velocity $V_b = \sqrt{k_B T_e / m_i}$, where k_B is Boltzmann's constant, T_e is electron temperature, and m_i is the mass of ion. The sheath is generally confined by a few Debye lengths [3], i.e. $\lambda_D = \sqrt{\varepsilon_0 k_B T_{i,e} / (e^2 n_{i,e})}$, where ε_0 is the vacuum permittivity, k_B is the Boltzmann constant, $T_{i,e}$ are ion and electron

temperatures, and $n_{i,e}$ are ion and electron densities. The Debye length is defined as the maximum dimension of the space charge region where quasi-neutrality can be disturbed. A normal glow can only exist if λ_D is smaller than the gap of electrodes where the region contains the plasma. The Debye length primarily depends on the combination of cathode material and gas because such combination influences the electron density of the plasma at a given applied voltage.

1.1.4 Current-Voltage Characteristics

Raizer [4] shows a general current-voltage (I-V) characteristic curve for various discharges in Fig. 1-1. We can see the region between A and B is called cosmic rays (not a discharge), which is important before Townsend discharge. The region between B and C is called Townsend dark discharge, which is characterized by very little light emission. The Townsend discharge is dark because at this stage the excitement of atoms by the electron impact is not important and ionization is so small that the gas emits no appreciable light. The region between C and D is known as subnormal glow discharge, which is a transition region between the glow and dark discharge regions that corresponds to a weak current. Region between D and E is called glow discharge, which is characterized by a stable glow discharge and the current varies from 1 μA to 1 A. During a glow discharge, the secondary emission is mostly due to positive ion bombardment. Region between E and F is called abnormal glow discharge. Region between F and G is a transition to an arc discharge, and region between G and H is an arc discharge where the current is larger than 1 A.

1.2 Literature Review

The plasma that has been used for the flow actuation at atmospheric pressure is a weakly ionized gas, where the ions are often near the ambient temperature. The plasma actuator for flow

actuation can be an asymmetric configuration with surface discharge shown in Fig. 1-2(A) or symmetric configuration with volume discharge shown in Fig. 1-2(B). In aerodynamics, people use surface discharge for drag reduction behind the airfoils and fuselages at a high angle-of-attack. Fig. 1-2(A) shows an isometric view of surface discharge between two electrodes arranged asymmetrically. One of the electrodes is exposed to the air, and the other is encapsulated in a dielectric material (e.g. PMMA, FR4, silica glass, Kapton tape, and Teflon tape). For a radio frequency (RF) surface or volume discharge with two horizontally displaced parallel electrodes, the actuator is driven by a kilovolt level applied voltage, and a kilohertz level driving frequency. The high electric field guaranteed from this potential initiates the instantaneous cathode to emit electrons. These electrons collide with neutral molecules or atoms, which initiates the following: dissociation, ionization, and excitation. When the plasma discharge appears over the dielectric (surface discharge), the electrons move to the powered electrode (+), and the ions go to the grounded electrode (-). As a result, the electrohydrodynamic (EHD) force is generated by the interaction of the charged particles and the electric field.

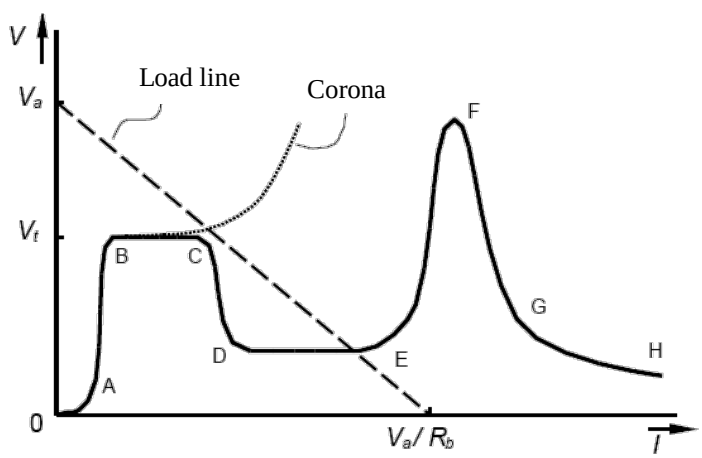

Figure 1-1. Current-Voltage (I-V) characteristic of low temperature discharge between electrodes for a wide range of currents. A-B: non-self-sustaining discharge, B-C: Townsend dark discharge, C-D: subnormal glow discharge, D-E: normal glow discharge, E-F: abnormal glow discharge, F-G: transition to arc, and G-H: arc discharge [4].

The attractions of DBD actuators include the absence of moving parts, quick response in a few nanoseconds, easy installation on any surface, and stable glow discharge at atmospheric pressure. Also, DBD actuators operate at cold (room) temperature and EHD force for imparting directed momentum to the bulk fluid flow. It has been proven to be effective at low speed control (10 – 20 m/s). However, the primary weakness of DBD actuators is the relatively small actuation effect. In order to improve the weakness for high speed flow control, microscale discharge may be a remedy to increase the EHD force for real aerodynamic applications.

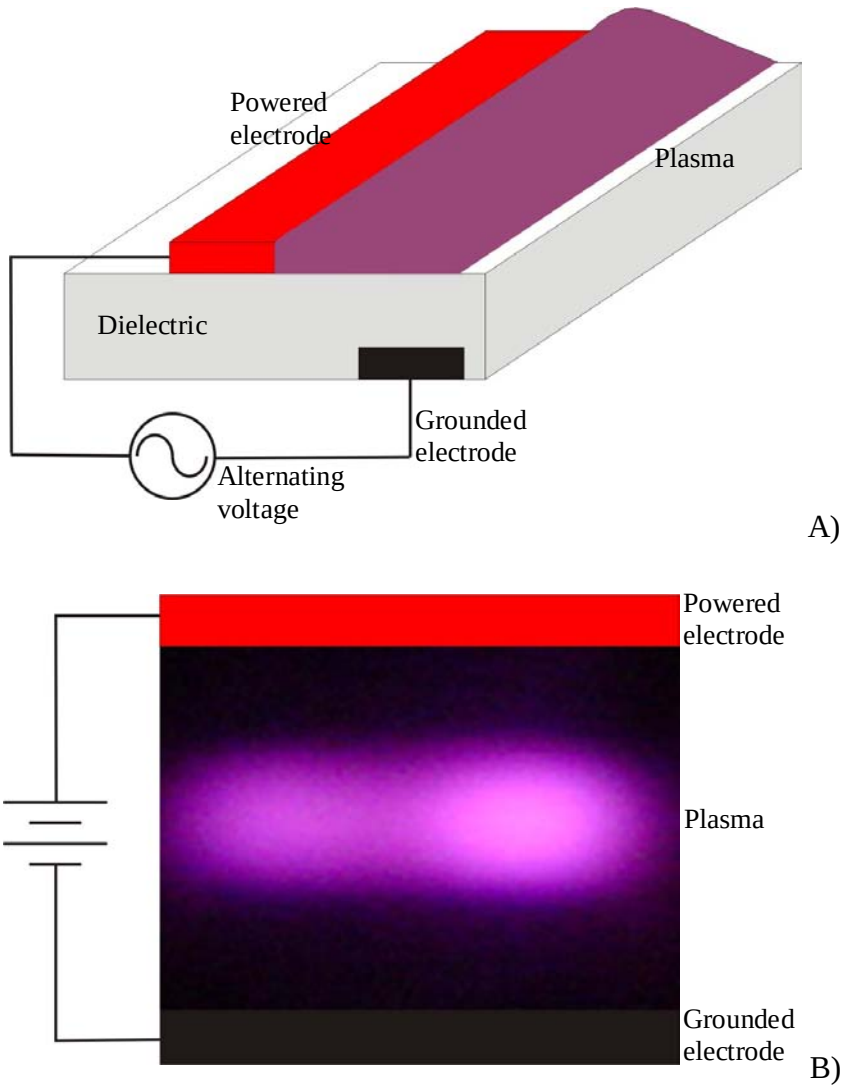

Figure 1-2. Schematics of plasma discharge for A) surface discharge and B) volume discharge.

1.2.1 Macroscale Discharge

Over the last decade, many experiments were conducted related to boundary layer flow control using DBD plasma actuators in aerodynamic applications. Kanda *et al*. [5] was the first one to produce weakly ionized plasma discharge using RF frequency. Such ideas were then utilized to control the fluid flows. Roth *et al*. [6-7] showed the aerodynamics application of One Atmosphere Uniform Glow Discharge Plasma (OAUGDP). He showed a strong vortical structure induced by paraeletric EHD body forces on the laminar flow via smoke wire flow visualization and mean velocity diagnostics shown in Fig. 1-3. In his experiment, the asymmetric electrode configurations produce more dramatic effects on the drag reduction rather than the symmetric electrode case. Fig. 1-4 shows a flow separation region is reduced by DBD plasma actuators. In order to enhance the electric force for large actuation effect, Enloe *et al*. [8] placed two DBD actuators next to each other, and they found that twice the momentum production was produced versus a single DBD actuator.

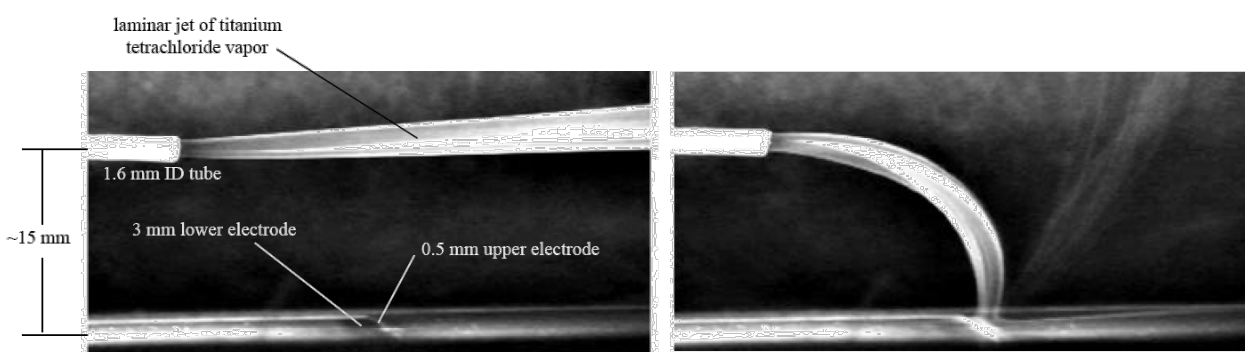

A) B)

Figure 1-3. Experiment of smoke wire laminar flow visualization for applied voltage of 4.5 kV_{rms} and driving frequency of 3 kHz [6]. A) Plasma off. B) Plasma on.

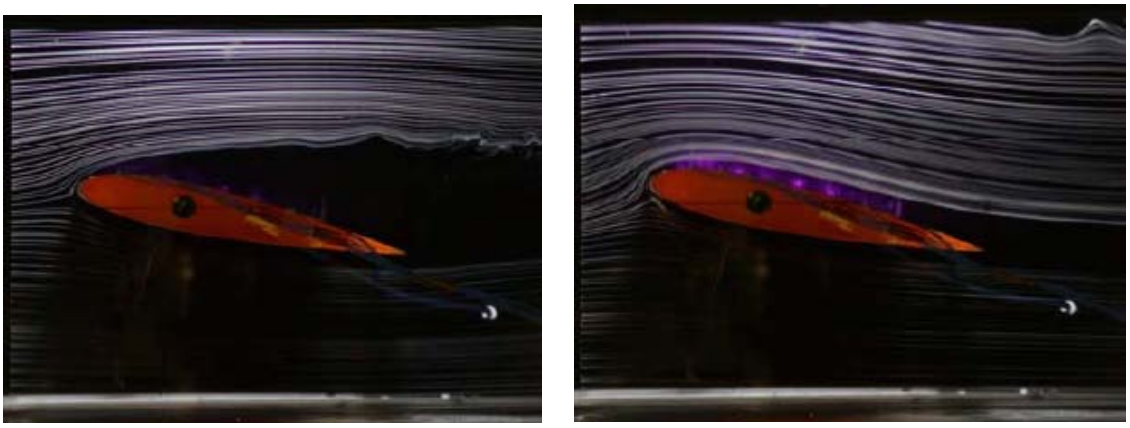

A) B)

Figure 1-4. Aerodynamics applications for flow attachment using plasma actuators on a NACA 0015 airfoil with a wind tunnel velocity of 2.85 m/sec, 12 degree angle of attack, applied voltage of 3.6 kV, and RF operating frequency of 4.2 kHz [7]. A) Plasma off. B) Plasma on.

There are some other experimental tools for studying the strength of the plasma EHD force. Enloe *et al.* [9] measured the light emission from the plasma actuator using a photomultiplier tube (PMT). Fig. 1-5 shows the RF discharge is much more irregular on the positive-going half cycle than the negative-going in one discharge cycle with a sinusoidal applied voltage waveform. Therefore, the discharge showed uniform structure and hence produced high thrust in only a half cycle. This explained the directed momentum effect of the time-averaged EHD force always acting from the exposed powered electrode to the grounded electrode. Even if the polarity of electrode is changed, the same effect exists. This phenomenon has also been proven by the Particle Image Velocimetry (PIV) measurements.

The force production mechanism was investigated by Gregory *et al.* [10] and Poter *et al.* [11]. From a theoretical derivation, the force production is due to the acceleration of ions through the applied electric field. They found the force production was governed by ion density, the volume of plasma, and the applied electric field. Fig. 1-6 exhibits a linear relationship between the force production and the gas pressure for different input powers from 5 to 20 W.

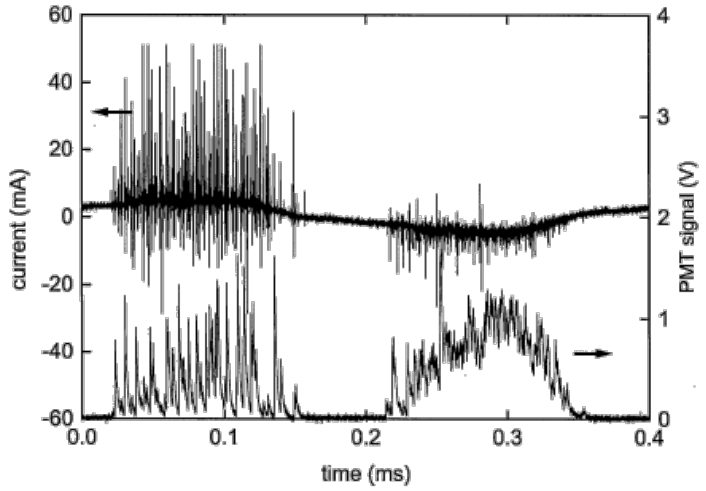

Figure 1-5. Positive-going half cycle from 0.0 to 0.2 ms is a much more irregular discharge than the negative-going part from 0.2 to 0.4 ms [9].

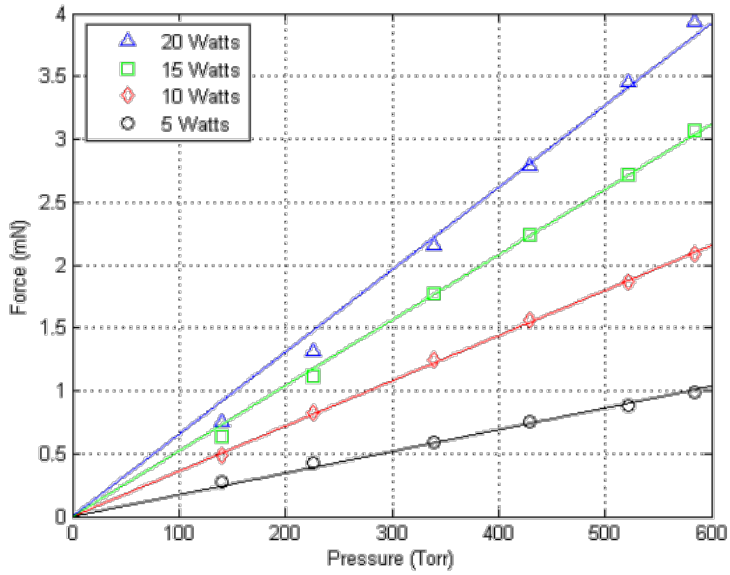

Figure 1-6. A linear relationship between air pressure (Torr) and force production (mN) for different input power from 5 to 20 Watts [10].

After understanding the physics of plasma actuators, parametric studies are also important factors to optimize the DBD actuator. According to the experiments conducted by Roth *et al.* [7] and Enloe *et al.* [8], they investigated the effects of dielectric materials, overlapping of electrodes, variable gap between electrodes, amplitude input, waveform input, operation frequencies, width of the anode and cathode, and the geometry of electrodes. It was discovered

that the dielectric losses for the PC board (e.g. FR4) is higher than Kapton™, Teflon™, and glass. In our test of the FR4 and PMMA DBD actuator, they delivered the stable glow discharge longer than Kapton™ or Teflon™. Roth *et al*. [7] found the gap distance d_g had a significant effect on the induced flow velocity. The highest induced velocities occurred in the range of 1 to 2 mm. The "gapless" design was significantly below the optimum. The shapes of electrodes are also important for the stable glow discharge formation. For the waveform chosen, Enloe *et al*. [8] suggested a sawtooth waveform to generate more thrust than the other waveforms. However, we didn't see any significant difference between the sinusoidal wave and the sawtooth wave in our plasma actuator test.

There are four different approaches to model the physics of plasma actuators. The first approach is the phenomenological model, which is based on force distribution approximation. The second is the load based method, which calculates the electric field from the Poisson equation and approximates charge distribution. The third is the reduced order method which correlates the relationship among the force, the load parameters (voltage and frequency), and the geometric parameters. The last approach is the purely first-principles based approach, which is solving ion density, electron density, and electric field distribution from plasma governing equations, and then applies the EHD force ($F_j = eqE_j$) as a body force to the Navier-Stokes equations.

Shyy *et al*. [12] used experimental data from Roth *et al*. [6] to develop a phenomenological model to study plasma-induced fluid flows. The local body force is a function of the electric field E, operating frequency ξ, collision efficiency α_c, charge density q, and duration of plasma is formed Δt, i.e. $F_{ave} = E\xi\alpha_c q\Delta t$. Fig. 1-7 shows the effect of the various parameters on streamwise velocity. The results show that the plasma produced the maximum relative effect on

the lower freestream velocity of 2 m/s in the Fig. 1-7(A) and the higher applied voltage of 5 kV in the Fig. 1-7(B).

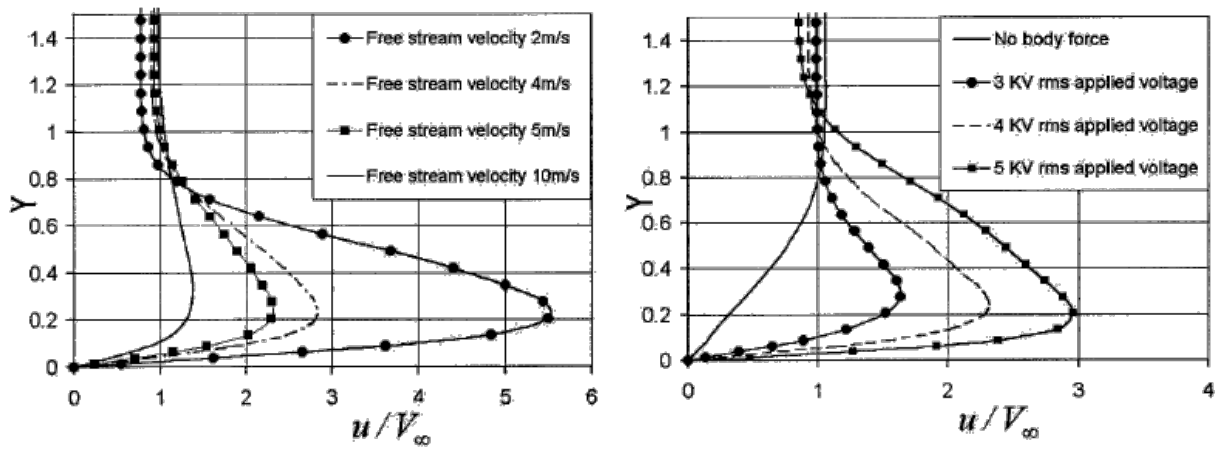

A) B)

Figure 1-7. The streamwise velocity effect of the various parameters with operating frequency of 3 kHz for A) different inlet velocities from 2 to 10 m/s with applied voltage 4 kV and B) different applied voltages from 3 to 5 kV with inlet velocity 5m/s [12].

Orlov *et al*. [13] studied the gas velocity induced flow using the load-based method. They solved Poisson equation ($\nabla^2\varphi = -q/\varepsilon_d$) and assumed the Boltzmann relation for the number of density, i.e. $n = n_0 \exp[e\varphi/(k_B T)]$ and charge density $q = -\varepsilon_d \varphi / \lambda_D{}^2$, where ε_d is the dielectric constant and λ_D is the Debye length. Fig. 1-8(A) shows the two-dimensional numerical results of the local body force distribution near the DBD actuator, where Fig. 1-8(B) is the fluid flow velocity vector induced by the local body force. The result of local body force looks suspicious due to the force vectors acting same direction normal to the dielectric surface at x = 0.002 to 0.006. Font [14] simulated the plasma as the electrons stream to the dielectric on the first half of the electrode bias cycle and the stream back on the second half. The results show the plasma actuator producing a time-averaged net force in only one direction. Gaitonde *et al*. [15] assumed

that the local body force distribution varies linearly, diminishing away from the surface until the critical electric field limit is reached for airfoils separation control.

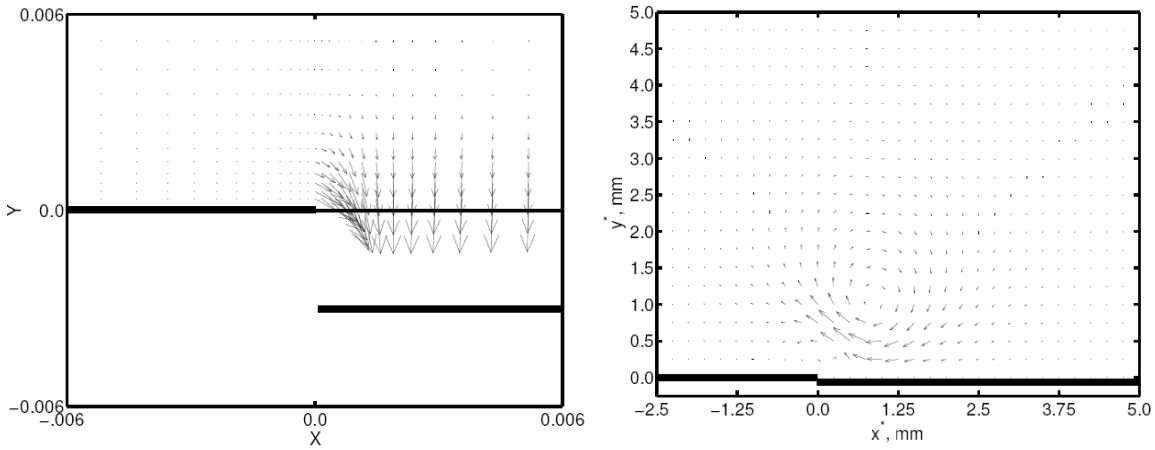

A) B)

Figure 1-8. Numerical results of body force and velocity vectors induced by DBD actuator [13]. A) Body force near the DBD actuator. B) Fluid flow resulting from body force with the largest velocity vector corresponds to 2 m/s.

We introduced a plasma actuator for film cooling enhancement in gas turbine applications and developed a time-averaged force model based on the phenomenological model [16-18]. The results showed an improvement of 100% effectiveness over the traditional design. The reduced order method based on the first-principles investigations of plasma actuation were conducted by Roy *et al*. [19-21]. The two-dimensional reduced order force model is shown below: [21]

$$F = F_{x0}\phi^4 \exp\{-\{[x - x_0 - (y - y_0)]/y\}^2 - \beta_x (y - y_0)^2\}\hat{i} + F_{y0}\phi^4 \exp\{-[(x - x_0)/y]^2 - \beta_y (y - y_0)^2\}\hat{j} \quad (1\text{-}1)$$

where F_{x0} and F_{y0} are taken from the average electrodynamic force obtained by solving air-plasma equations, ϕ is potential, x_0 is the midpoint between the RF electrode and the grounded electrode, y_0 is at the dielectric surface, β_x and β_y are functions of dielectric material and adjusted to match the velocity induced by the electrodynamic force. Fig. 1-9 shows the normalized velocity components at the *x*-direction and *y*-direction obtained using an

electrodynamic force and approximated force equations for different locations. The results are similar trends for both the electrodynamic and the approximated forces. We used the modified force model from Singh and Roy [21] for the approximated force based on the reduced order method. It has been applied to novel designs of horseshoe and serpentine actuators shown in Fig. 1-10. The detailed information of bulk flow control using horseshoe and serpentine actuators can be found in [22].

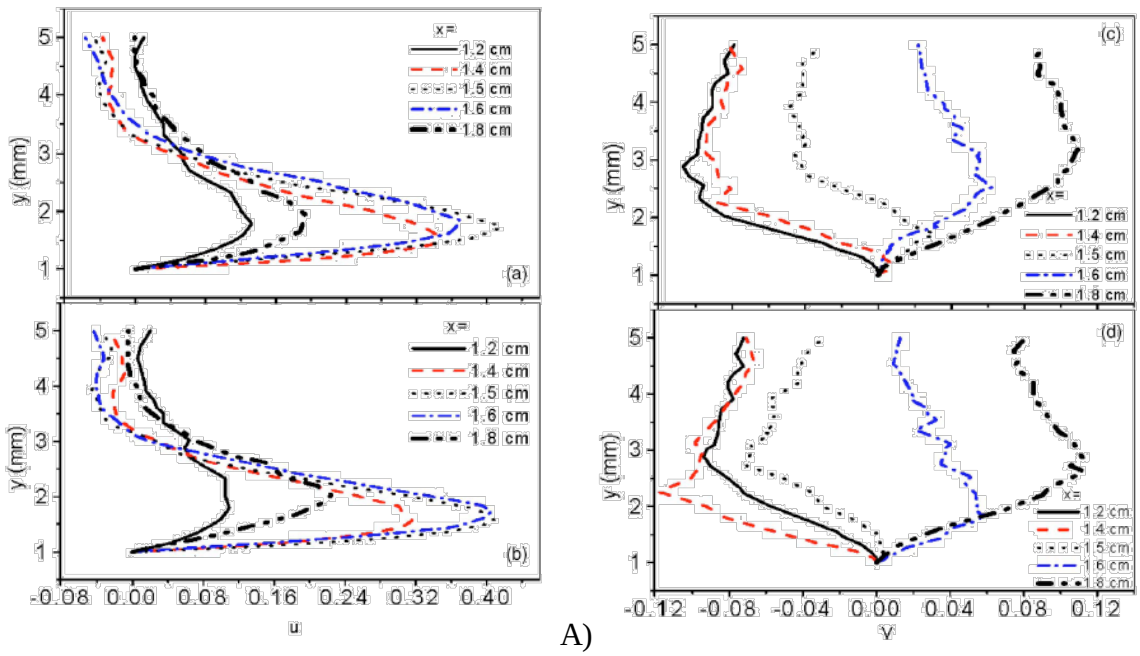

A) B)

Figure 1-9. The normalized velocity components obtained using electrodynamic force and approximated force as a function of *y* for different locations *x* for operating frequency 5 kHz and applied voltage 1000 V [21]. A) *u*-velocity. B) *v*-velocity.

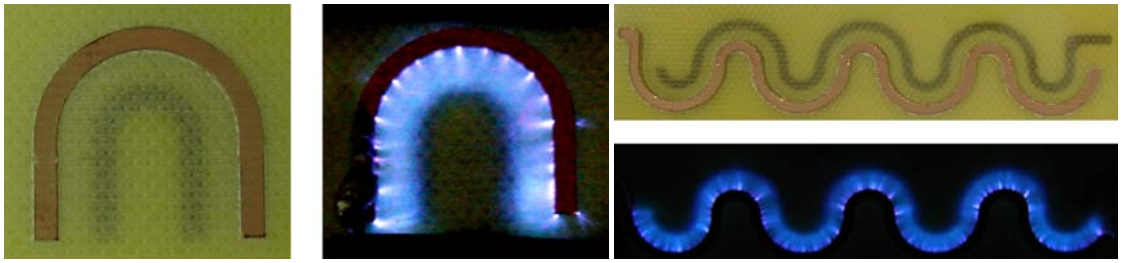

A) B)

Figure 1-10. Top view of experimental photograph illustrates plasma discharge on/off for A) horseshoe and B) serpentine actuators.

A higher fidelity first-principles approach is used to model plasma in a self-consistent solution of multi-dimensional, multi-fluid equations, which implicitly couple the Maxwell and Navier-Stokes equations. Roy [23] and Likhanskii *et al.* [24] developed gas models for two species (ion n^+ and electron e^-) and three species (n^+, n^-, e^-), respectively. They predicted charge densities q and the electric field E to calculate the electric force ($F_j = eqE_j$) and then computed the gas velocity distributions induced by the electric force. Fig. 1-11(A) shows the velocity field based on a quiescent flow and depicts a strong wall jet downstream of the RF electrode away from the dielectric surface. The local vertical line shown in Fig. 1-11(B) describes how the flow velocity increases at different locations. Likhanskii *et al.* [24] presented the instantaneous force of the DBD actuator changing the direction due to the RF signal changing shown in Fig 1-12. From the numerical simulation, they found the time-averaged force only acting one direction shown in Fig 1-12(C).

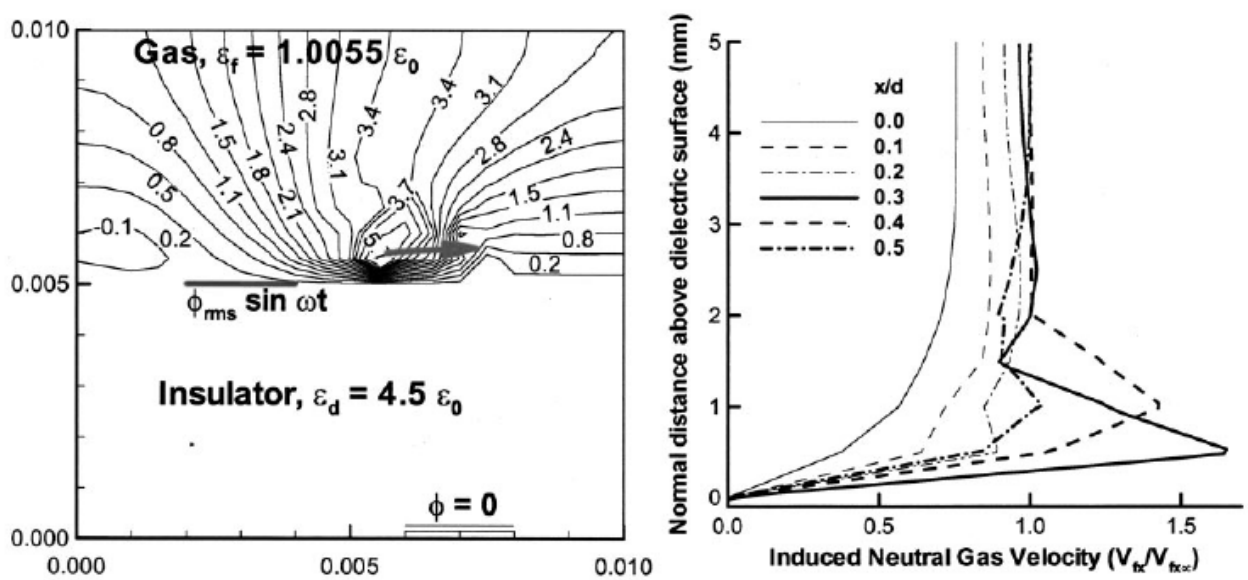

A) B)

Figure 1-11. Fluid velocity computed from the electric force for A) 2D contour lines velocity distribution and B) streamwise velocity component at different locations [23].

Singh and Roy [25-26] solved real gas air chemistry problems in 2D with eight species (e^-, $N_2, N_2^+, N, O_2, O_2^+, O^-, O$) and in 3D with five species (e^-, O_2, O_2^+, O^-, O). Fig. 1-13 shows that the charged density peaks are very close to the tip of the RF electrode where powered electrode is from x = 1.7 to 1.9 cm and grounded electrode is from x = 2.1 to 2.3 cm. The charged density decreases sharply with increase distance from the surface. The peak ion densities are more comparable for both the small grounded electrodes than for the long grounded electrodes. Fig. 1-14 presents a variation of densities of different species along the z-direction. The time-averaged electric force is calculated from $F = e(n_{o_2}^+ - n_e - n_o^-)E$. Based on these first-principles analysis, three-dimensional plasma discharge has been approximated and numerically tested for air.

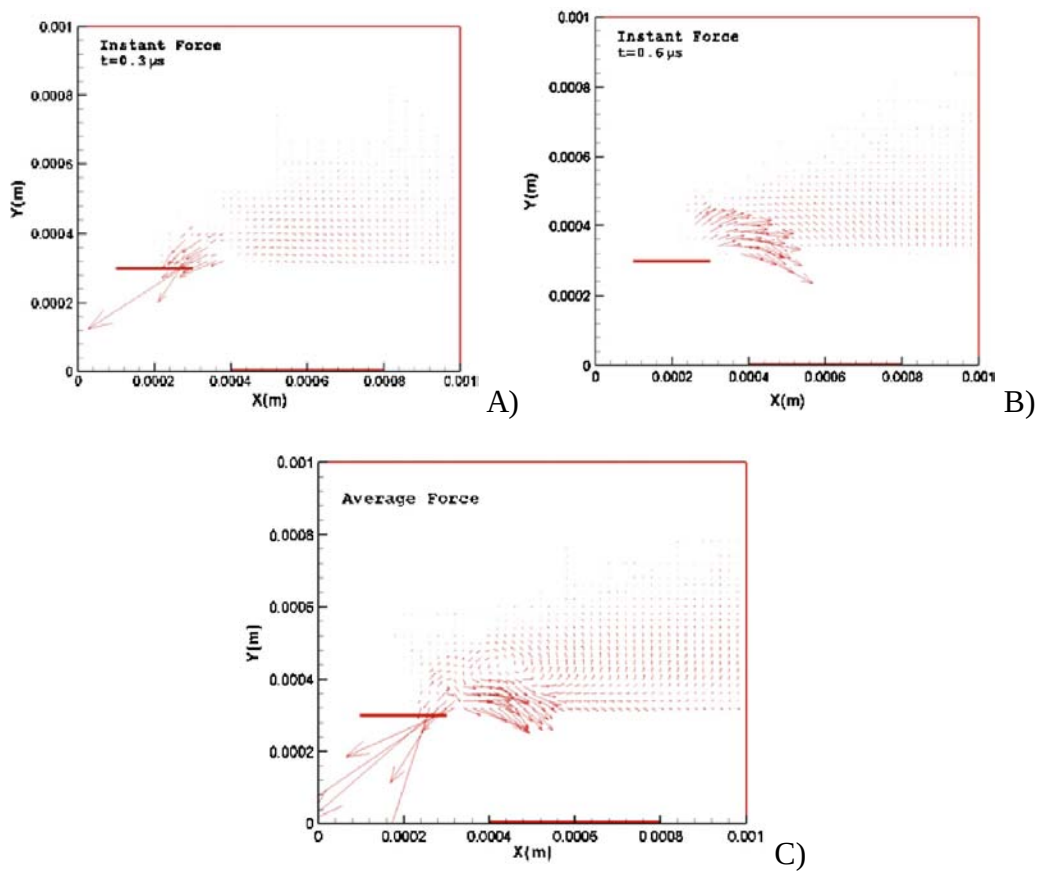

Figure 1-12. Force vector acting on neutral gas with applied voltage of 1.5 kV and operating frequency of 1 MHz for A) instantaneous force during the negative half-cycle, B) instantaneous force during the positive half-cycle, and C) average force [24].

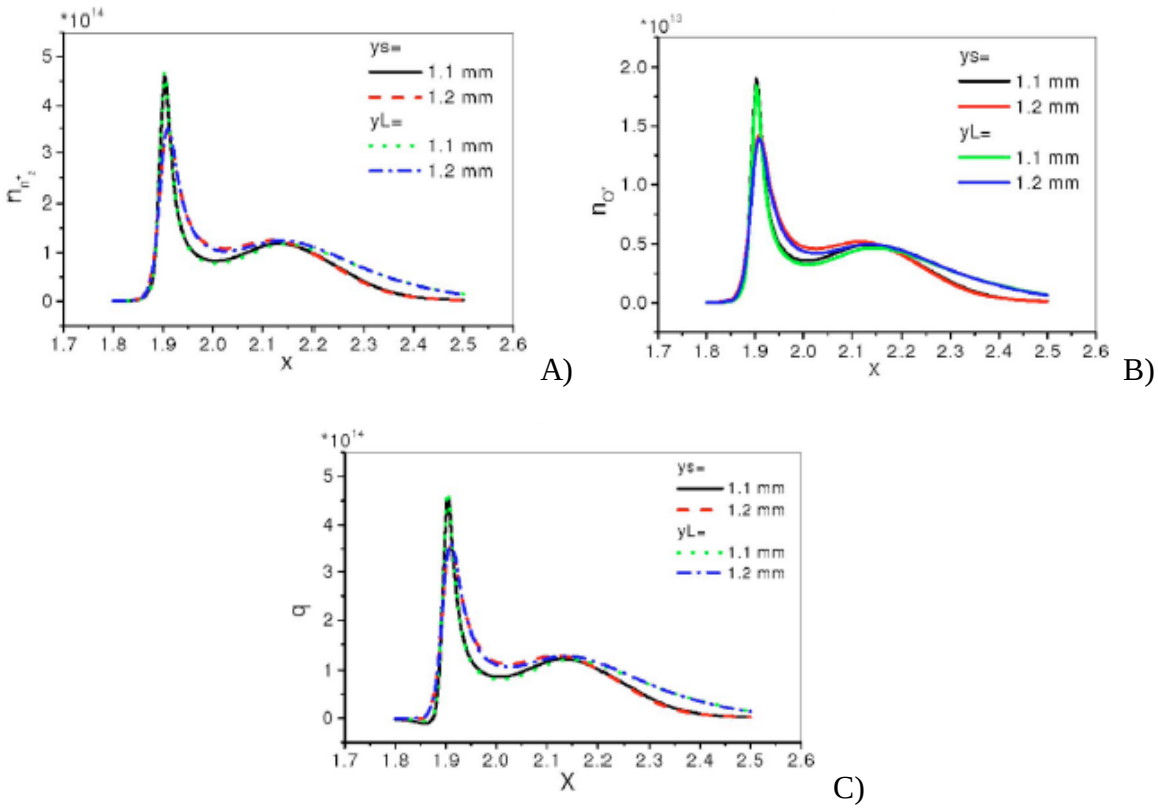

Figure 1-13. The positive ion density and charge separation at different *y* locations with both small and long grounded electrodes for A) positive nitrogen ion N_2^+, B) positive oxygen ion O_2^+, and C) charge density *q*. Here x is in cm [25].

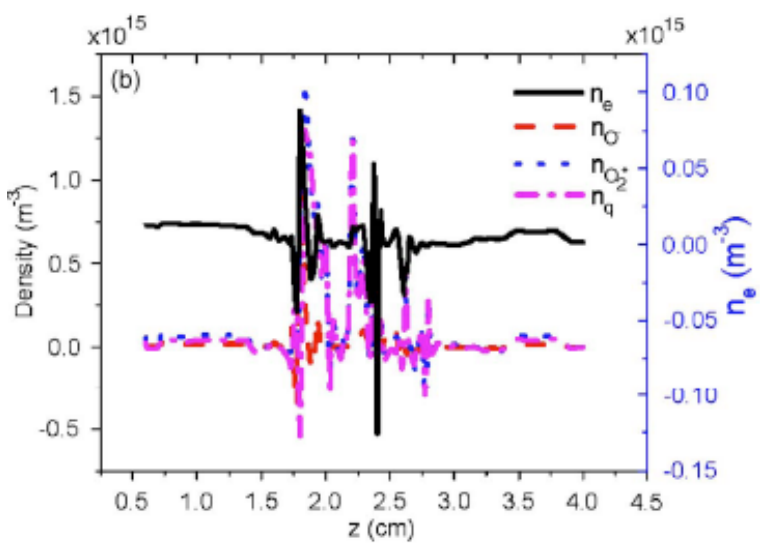

Figure 1-14. The density of various species (n_e, n_{o^-}, $n_{o_2^+}$) and charge separation (n_q) varying with *z*-direction [26].

1.2.2 Microscale Discharge

To generate a stable plasma glow discharge at atmospheric pressure in a range of hundreds μm or less is a promising approach. The reasons for using plasma in microscale are lower breakdown voltages and consequently power consumption to drive the discharge. For the plasma operating near atmospheric pressure, there is no need to pay a high maintenance costs for a vacuum chamber. The miniaturization of plasma discharges has been studied for the development of new applications [27], such as NO_x and SO_x remediation, the destruction of volatile organic compounds (VOCs), ozone generation, excimer formation as UV radiation sources [28], materials processing, surface modification as plasma reactors [29], and possibly breakdown and boundary-dominated phenomena for aerodynamic applications.

Several studies have been reported in the literature regarding electrical breakdown voltage varying from 300 to 750 V in microscale gap (1~ hundreds micron) [29-33]. Electrical breakdown is the process of the transformation of a non-conducting material into a conductor as a result of applying a sufficiently strong field to the material. This occurs when the applied voltage at least equal to the breakdown voltage. The breakdown characteristics of a gap are a function of the gas pressure p and the gap length d_g, which is based on Paschen's law [34]. For the same breakdown voltage, smaller dimensions are enabled by higher operating pressures. Torres *et al*. [31], Longwitz [33] and Germer [35] showed Paschen's law was not valid for gaps of less than 5 μm. From the experimental results by Torres *et al*. [31], we can see the deviation of Paschen's law below 5 micron shown in Fig. 1-15(A). We also can see the electric field decreasing in the same region. This explained the deviation of Paschen's curve is due to the quantum tunneling of electrons, which is possible to allow the electrons to pass through a barrier

without sufficient energy. For a small gap, when surface roughness becomes non-negligible, changing the pressure must have a different influence than changing the distance.

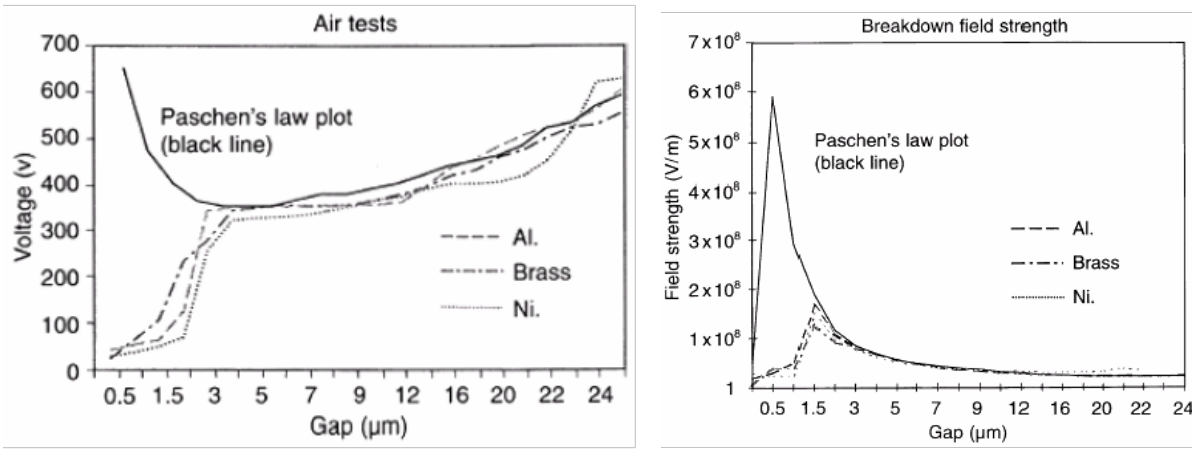

A) B)

Figure 1-15. The deviation of the Paschen's curve with air for different materials [31]. A) Breakdown voltage results versus gap. B) Electrostatic field results versus gap.

Before breakdown, the current in the gap between electrodes is very low. However, once the breakdown voltage is applied, breakdown occurs and leads to a discharge. During the current increases, Massines *et al*. [36] showed that the discharge transited from a non-self-sustained discharge to a Townsend discharge and then to a subnormal glow discharge in helium and argon. In nitrogen, however, the ionization level was too low to induce a localization of the electrical field and the glow regime was not achieved. Different regimes are also observed by Sublet *et al*. [37]. DBD was a glow-like discharge in helium and Townsend-like discharge in nitrogen.

Although microscale discharge has been studied experimentally for more than a decade, our understanding of the fundamental physics is still limited due to the reduced dimension, complicated transient behavior, and rapid collision in micro gaps. Therefore, numerical simulation is a remedy to overcome the experimental challenges.

In the past few years, the numerical investigations of microscale discharge have appeared in literature. There are three basic models that describe the evolution of charged particles in plasma discharges. The first one is the hydrodynamic model, which is most popular. The second one is the kinetic model, which is the particle-in-cell/Monte Carlo collision (PIC/MCC) model. The third one is the hybrid kinetic-fluid simulation model, which is often used for modeling high-density plasma reactors. Kushner [38-39] presented a two-dimensional plasma hydrodynamic model of microscale discharge (MD) devices operating at pressures of 450-1000 Torr and dimensions of 15 to 40 μm. He found the MD devices typically require more applied voltages to operate at lower pressures, and because of this, they resemble discharges obeying Paschen's curve for breakdown. Boeuf *et al*. [40] developed a fluid-based model to clarify the physical mechanisms occurring in microhollow cathode discharges (MHCD). Wang *et al*. [41] simulated a microscale discharge in helium at atmospheric pressure based on the hydrodynamic model and found that it resembled a macroscopic low pressure DC glow discharge in many respects. Fig. 1-16 shows their simulation results were in agreement with experimental observations.

A one-dimensional Particle-In-Cell Monte Carlo Collision (PIC-MCC) model was developed by Choi *et al*. [42] for current-driven atmospheric-pressure helium microscale discharge. The PIC-MCC simulation results were compared with the fluid simulation results shown in Fig. 1-17. The results show the sheath widths are comparable in both the PIC-MCC and fluid simulation, and the peak of the electron and ion densities were within the same order of magnitude. However, the density profiles were significantly different. Radjenovic *et al*. [43] utilized the PIC-MCC model and found the deviation from Paschen's law when the gaps between electrodes are smaller than 5 μm shown in Fig. 1-18. From their point of view, the electron

mean path is of the order of a few micrometers at atmospheric pressure. So the electrical breakdown is initiated by the secondary emission processes instead of a gas avalanche process at small interelectrode spacing.

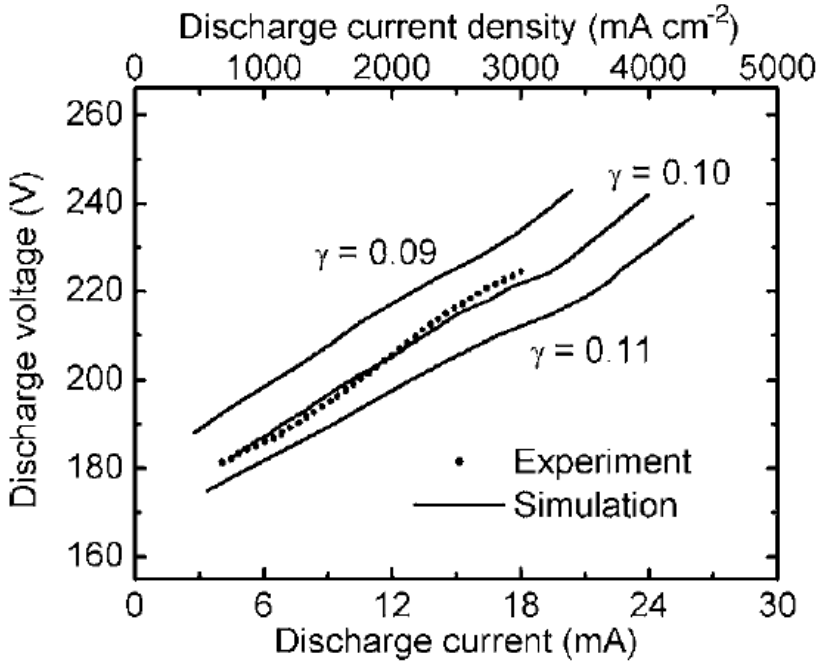

Figure 1-16. Comparison of numerical results (solid line) and experimental data (dashed line) for current-voltage (I-V) characteristics in a parallel plate with helium DC microscale discharge at 760 Torr and 200 μm interelectrode gap with different secondary electron emission coefficient $\gamma = 0.09$, 0.10, and 0.11, respectively [41].

Another useful approach to simulate microscale plasma discharge is using the hybrid kinetic-fluid model. In this model the reaction rates are obtained by solving a zero-dimensional Boltzmann equation, while the transport of electrons, ions and neutrals is carried out via fluid models. Farouk *et al.* [44] simulated a DC argon micro glow-discharge at atmospheric pressure using CFD-ACE+ code based on a hybrid model. The simulations were carried out for a pin-plate electrode configuration with interelectrode gap spacing of 200 μm together with an external circuit. The temperature measurements, which were around 500 K, suggested the discharge as a

non-thermal, non-equilibrium plasma. The measured temperatures and the predicted temperatures are found to compare favorably.

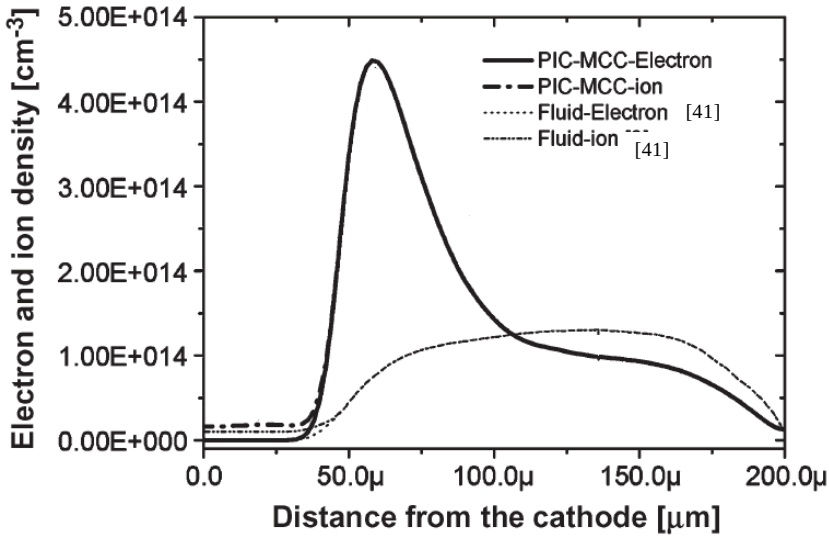

Figure 1-17. Comparison of PIC-MCC and hydrodynamic simulation for density profile in a DC helium microdischarge at atmospheric pressure [42].

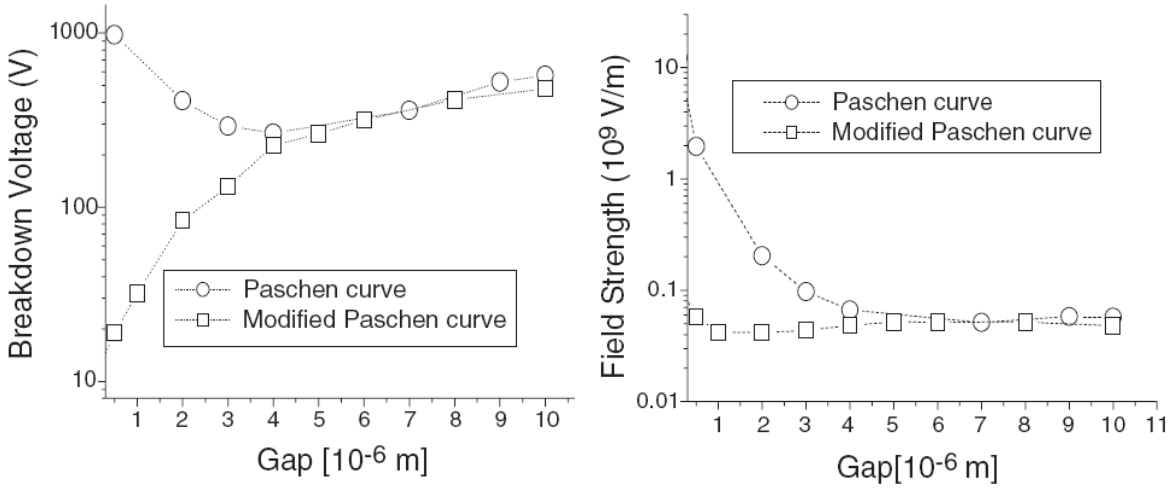

A) B)

Figure 1-18. The numerical results are compared with Paschen's curve for argon at 1 atm [43]. A) Breakdown voltage and B) electric field strength is a function of the gap size.

1.2.3 Micropump

Mircopump is made by fabrication on the order of micrometers to draw or drain the working fluid in the microfluidic system, such as lab-on-a-chip (LOC) or a micro total analysis system (μTAS). Since its introduction in mid 1970s [45], micropumps are becoming widely popular in a variety of applications ranging from biological analysis and chemical detection to space exploration and microelectronics cooling. A variety of micropumps has been developed based on the operational mechanism. These may be categorized as mechanical and non-mechanical devices. Mechanical micropumps drive the working fluid through a membrane or diaphragm, while non-mechanical micropumps inject momentum or energy into a local region to produce pumping operation. Based on the motion of mechanical micropumps, it can be divided into reciprocating, rotary, and aperiodic pumps. Mechanical micropumps include electrostatic, pneumatic, thermopneumatic, piezoelectric, and electromagnetic diaphragm pumps. Non-mechanical micropumps include electrohydrodynamic (EHD), electroosmotic (EO), and magnetohydrodynamic (MHD) pumps. Diaphragm pumps can be used for any gas or liquid and generate flow rates in the range of ml/min. However, the drawbacks are the relatively high cost and the short life time of moving diaphragm due to their frequently on/off switching. In contrast, the primary advantage of non-mechanical micropumps is without moving parts. Furthermore, the simple design of such pumps may reduce the cost and increase miniaturization, so that it improves the integration into the microfluidic system. A thorough review of the actuation mechanism and the applications of micropumps have been described by Nguyen *et al.* [46], Laser and Santiago [47], and Oh and Ahn [48].

EHD pump uses electric force based on the space charge generation and the electric field to add momentum to the fluid for pumping effect. Stuetzer [49] and Pickard [50-51] were the

first who studied the theoretical and experimental investigation of the EHD pump. Later, numerous EHD micropumps have been reported [52-62]. Richer *et al.* [52-53] tested and improved the design of EHD micropump. The micropump produced an averaged flow rate of 14 ml/min with ethyl alcohol as working fluid. The electrodes are separated by a gap of 350 μm with an applied potential of 650V. Ahn *et al.* [54] and Darabi *et al.* [55-56] tested ion-drag micropump capability shown in Fig. 1-19. Ahn *et al.* reported an averaged flow rate of 40 to 60 μl/min with an applied voltage of 60 to 100 V. It also drives the ethyl alcohol as a working fluid. Drarbi *et al.* showed comparisons between experimental and simulation results for ion-drag micropump shown in Fig. 1-20. Fuhr *et al.* [57-58] and Choi *et al.* [59] studied EHD micropump based on the traveling wave-driven mechanism shown in Fig. 1-21. Fuhr *et al.* showed the pump generates a maximum flow rate of Q_{max} = 2 μl/min for water under applied voltage of 40 V. A detailed comparison of maximum flow rate for EHD and EO micropumps is shown in Fig. 1-22. Nowadays, such EHD micropumps are also applied to drug-delivery into human body [60] and ion propulsion in space [61].

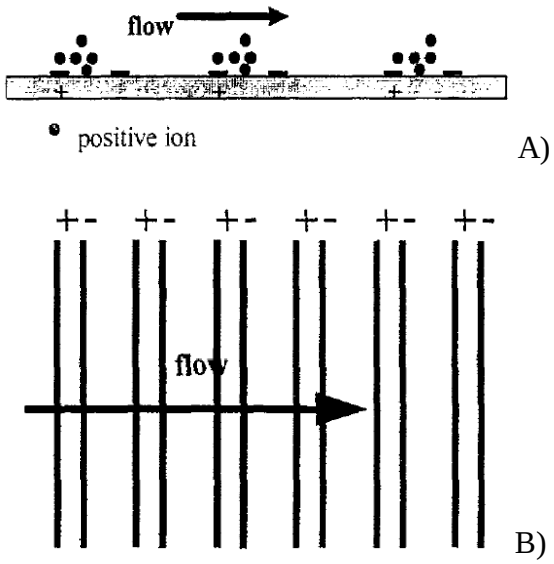

Figure 1-19. Schematic of ion drag pumping using multiple electrodes for A) side view and B) top view [54].

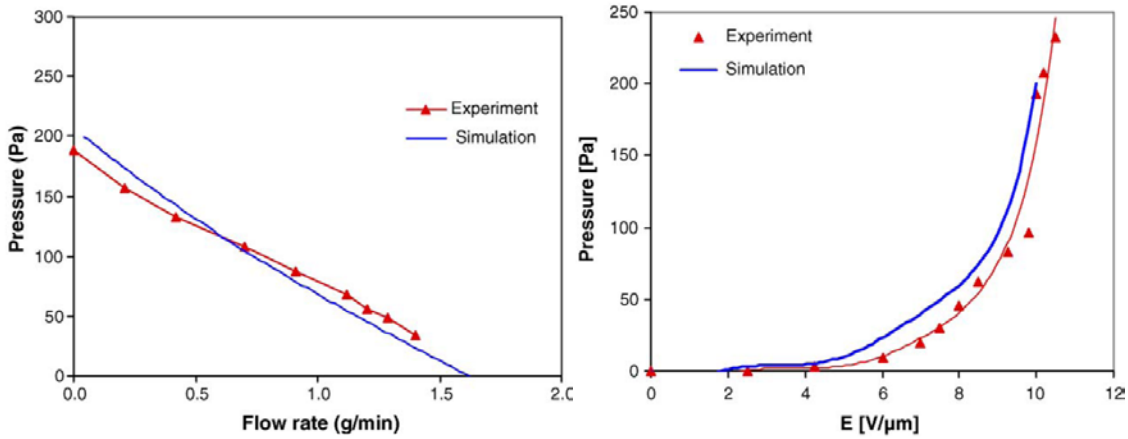

A) B)

Figure 1-20. Comparison of pressure head between numerical and experimental data under no flow condition [56] for A) pressure head as a function of flow rate condition and B) pressure head as a function of electric field.

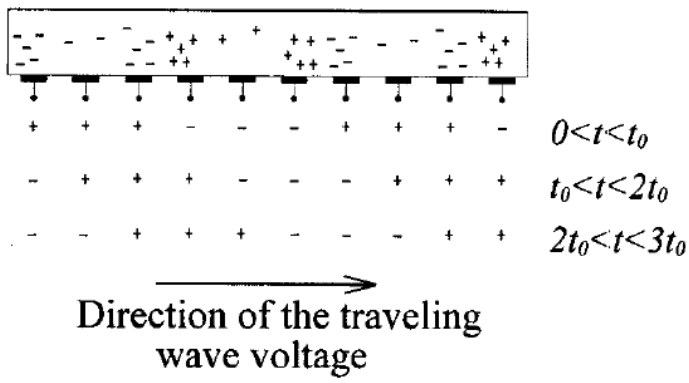

A)

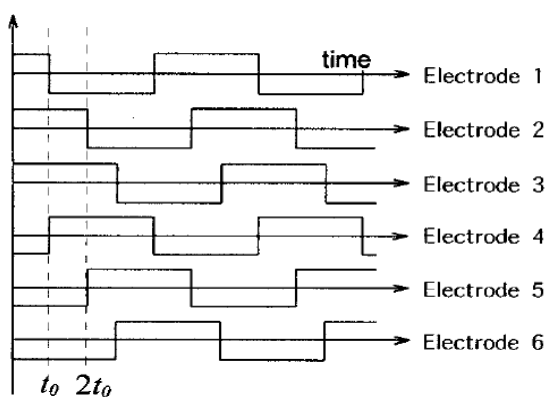

B)

Figure 1-21. Traveling wave voltages concept for A) conceptual diagram and B) six phases of square traveling wave voltages at each electrode with 60 degree delayed [59].

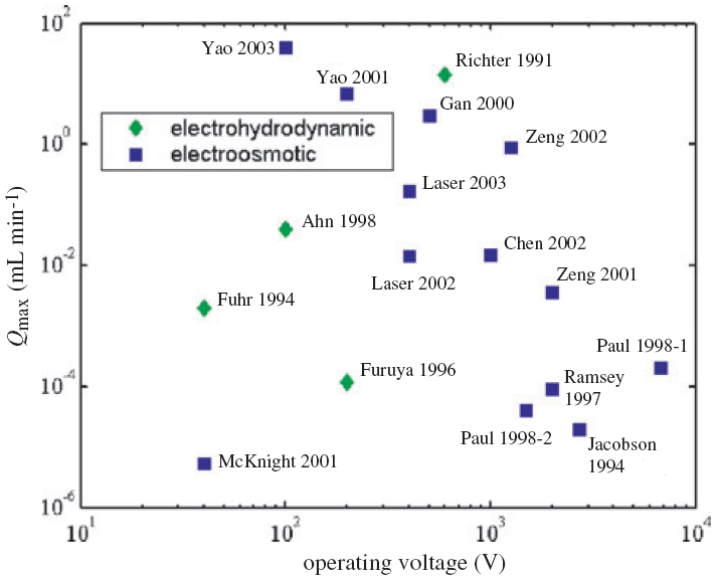

Figure 1-22. The reported experimental data of maximum flow rate for electrohydrodynamic and electroosmotic micropumps [47].

Roy [62] presented a concept of EHD micropump using dielectric barrier discharge (DBD) actuators shown in Fig. 1-23. We can see this tri-directional plasma pump draws the fluid into the micro channel at the both inlets due to the attraction of parallel plasma actuators and drains the fluid upward to the outlet by means of serpentine plasma actuators. Such design leverage several advantages of non-mechanical micropumps.

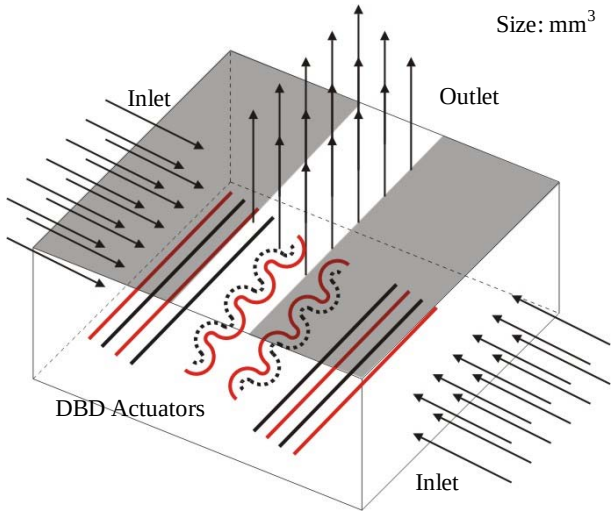

Figure 1-23. Schematic of three-dimensional micro plasma pump.

1.3 Outline of the Dissertation

Since we are interested in the large actuation effect for high speed flow control applications, we study plasma discharge in small interelectrode gaps on the order of μm to hundreds of μm at atmospheric pressure. So far very little work has been done on the microscale discharge and the theory is not clearly understood, especially for real world applications. The plasma governing equations we used are based on a hydrodynamic model, which gives reasonably accurate predictions of discharge properties at sufficiently high pressures for understanding fundamental physics of plasma actuators, and it has also been proved in literature.

In chapter 2, we present both the plasma governing equations and Navier-Stokes equations for modeling fluid flow induced by plasma actuation in both macro and microscale. We also introduce some basic physics in the area of fluid dynamics. In the following section, we will explain how to employ finite element method to discretize partial differential equations. We use a powerful Multi-scale Ionization Gas (MIG) flow code for solving a coupled system of hydrodynamic equations, Poisson equation, and Navier-Stokes equations to calculate the ions, electrons, and electric field distribution over the computational domain. We present two applications for plasma actuators in macroscale in the last section. One is using plasma to actuate heat transfer, and the other is using horseshoe and serpentine actuators for bulk flow control. The results are compared with experimental data and show mimic trends. The detailed description can also be found in Applied Physics Letters [16], Journal of Applied Physics [17], and Journal of Physics D: Applied Physics [22].

In chapter 3, we present a two-dimensional microscale volume discharge for nitrogen gas at atmospheric pressure. In such small interelectrode gap, the deviations of Paschen's law will dominate the plasma region. In the following section, we explain the numerical setup for the

computational domain. In the last section, we show some results with various gaps from 200 to 5 μm between electrodes. The obtained numerical results show good agreement with reported experimental data [33].

In chapter 4, we introduce the applications of micro plasma pump and horseshoe plasma actuator for two- and three-dimensional microscale plasma simulation. The results of two-dimensional micro plasma pump show reasonable flow rate on the order of ml/min compared with reported data. For the improvement of EHD mircopump, a novel design of horseshoe plasma actuator may be helpful. Such fully three-dimensional electric force nature proves the bulk flow control for tripping and ejecting fluid normal to the plane of the actuator by pinching the fluid using plasma force. Finally, the flow rate of new generation of micro plasma pump has been improved one order of magnitude higher than reported data. I have written all the above results in Journal of Applied Physics, Applied Physics Letters, and Journal of Physics D: Applied Physics.

In chapter 5, I summarized all the results for both macro and microscale cases. Our studies are mainly contributed to physics of plasmas actuators and physics of computation, especially in three-dimension. For the future work, I will focus on more realistic simulation and experimental work. Parallel computation may be required for more real world applications.

CHAPTER 2
NUMERICAL MODEL

In chapter 1, I discussed some basic physics in plasma and reviewed the relevant experimental and numerical efforts for macroscale discharge, microscale discharge, and micropump. In this chapter, I will present the plasma and Navier-Stokes governing equations for solving plasma-gas interaction problem. For the plasma and fluid governing equations, I use a finite element method to discretize for numerical computation. The formulation and the algorithm will be discussed in chapter 2.3. In the last section, I will show two macroscale applications which are plasma actuated film cooling and bulk flow control using horseshoe and serpentine actuators.

2.1 Plasma Governing Equations

A hydrodynamic model is obtained from Kumar and Roy [63] for multi-scale plasma discharge simulation at atmospheric pressure. The model uses an efficient finite element algorithm. The unsteady transport for electrons and ions is derived from fluid dynamics in the form of mass and momentum conservation equations. The species momentum is modeled using the drift-diffusion approximation under isothermal condition that can be derived from the hydrodynamic equation. At atmospheric pressure, the drift-diffusion approximation is reasonable and computationally efficient. The continuity equations for ion and electron number densities are given by:

$$\begin{aligned}
&\frac{\partial n_i}{\partial t} + \frac{\partial \left(n_i V_{ij} \right)}{\partial x_j} = \alpha \left| \Gamma_e \right| - r n_i n_e \\
&\frac{\partial n_e}{\partial t} + \frac{\partial \left(n_e V_{ej} \right)}{\partial x_j} = \alpha \left| \Gamma_e \right| - r n_i n_e \\
&\left| \Gamma_e \right| = \sqrt{\sum_j (n_e V_{ej})^2},\ 1 \le j \le 3
\end{aligned} \tag{2-1}$$

where n is the number density, $V_{i,e}$ is the species hydrodynamic velocity, r is the electron-ion recombination rate, subscript j is the coordinate direction, and subscript i and e are ion and electron, respectively. The discharge is maintained using a Townsend ionization scheme. The ionization rate is expressed as a function of electron drift velocity and Townsend coefficient α:

$$\alpha = Ape^{-B/(|E|/p)} \tag{2-2}$$

where A and B are preexponential and exponential constants, respectively, p is the gas pressure, and E is the electric field. $|\Gamma_e|$ is the effective electron flux and depends mainly on the electric field. The ionic and electronic fluxes in equation (2-1) are written as:

$$n_i V_i = n_i \mu_i \left(E + V_i \times B_z\right) - D_i \nabla n_i \tag{2-3}$$

$$n_e V_e = -n_e \mu_e \left(E + V_e \times B_z\right) - D_e \nabla n_e \tag{2-4}$$

where the electrostatic field is given by $E = -\nabla\varphi$. The Lorentz force term, $V \times B$, brings in the effect of the magnetic field. We neglect the magnetic field effect in this study. After some algebraic manipulations, we end up with the following equations:

$$\frac{\partial n_i}{\partial t} + \frac{\partial}{\partial x_j}\left\{ n_i \mu_i E_{x_j} - D_i \frac{\partial n_i}{\partial x_j} \right\} = \alpha \left|\Gamma_e\right| - r n_i n_e \tag{2-5}$$

$$\frac{\partial n_e}{\partial t} + \frac{\partial}{\partial x_j}\left\{ -n_e \mu_e E_{xj} - D_e \frac{\partial n_e}{\partial x_j} \right\} = \alpha \left|\Gamma_e\right| - r n_i n_e \tag{2-6}$$

where μ is the mobility, D_e is the electron diffusion calculated from the Einstein relation which is a function of the mobility μ_e , Boltzmann's constant k_B, and the electron temperature T_e, i.e. $D_e = k_B T_e / (e\mu_e)$. The ion mobility μ_i is expressed as a function of a reduced field (E/p).

The relation between electric field and charge separation is given by the Poisson equation:

$$\varepsilon_0 \nabla \cdot E = -e(n_e - n_i) \tag{2-7}$$

where ε_0 is the permittivity in vacuum and e = 1.6022*10^{-19} C is the elementary charge.

The system of equations (2-5)-(2-7) is normalized using the following normalization scheme: $\tau = t/t_0$, $x_j^* = x_j/d_l$, $N_e = n_e/n_0$, $N_i = n_i/n_0$, $u_e = V_e/V_B$, $u_i = V_i/V_B$, and $\phi = e\varphi/k_BT_e$ where $V_B = \sqrt{k_BT_e/m_i}$ is the Bohm velocity, m_i is the ion mass, reference length is d_l which is usually a domain characteristic length in the geometry, the reference time is t_0, and reference density is n_0. The working gas is nitrogen. For the case of atmospheric pressure, we use the value of rate coefficients given by Kossyi *et al*. [64]. For the case of low pressure, the ion mobility and diffusion at 300 K as well as electron mobility and diffusion at 11600 K are given by Surzhikov and Shang [65].

2.2 Flow Governing Equations

In the macroscopic view, fluid mechanics is assumed as a continuum [66]. Leonhard Euler is generally credited with giving a firm foundation to this idea. The continuum concept considered fluid properties (e.g. density, velocity, pressure, and temperature) to be continuous from one point to another. In microscale (molecular scale), fluid properties are non-uniform due to intermolecular spacing and random molecular motion.

2.2.1 Navier-Stokes Equations

Fluids are governed by conservation of mass, and the conservative form of continuity is:

$$\frac{\partial \rho}{\partial t} + \frac{\partial(\rho V_{nj})}{\partial x_j} = 0 \tag{2-8}$$

where ρ is the fluid density. The second term can be further decomposed via chain rule:

$$\frac{\partial \rho}{\partial t} + V_{nj}\frac{\partial \rho}{\partial x_j} + \rho\frac{\partial V_{nj}}{\partial x_j} = \frac{D\rho}{Dt} + \rho\frac{\partial V_{nj}}{\partial x_j} = 0 \tag{2-9}$$

For incompressible flow, the characteristic velocity V_n must be much smaller than speed of sound c, i.e. Mach numbers Ma = V_n / c below approximately 0.3, and the compressible effect can be neglected. The following equation for the incompressible fluid (ρ =constant) is:

$$\frac{\partial V_{nj}}{\partial x_j} = 0 \tag{2-10}$$

Fluids are also governed by conservation of momentum which is an application of Newton's second law as follows:

$$\rho \frac{DV_{nj}}{Dt} = \rho f_j + \frac{\partial \sigma_{ji}}{\partial x_i} \tag{2-11}$$

where ρf_j is the body force and σ_{ji} is the stress tensor as follows:

$$\sigma_{ji} = -p\delta_{ji} + \mu(\frac{\partial V_{nj}}{\partial x_i} + \frac{\partial V_{ni}}{\partial x_j}) \tag{2-12}$$

where p is the pressure, and μ is the viscosity of fluid. For an incompressible Newtonian fluid, the Navier-Stokes equation is:

$$\rho \frac{DV_n}{Dt} = \rho f - \nabla p + \mu \nabla^2 V_n \tag{2-13}$$

A useful normalized factor which can be found by normalizing equation (2-13):

$$\frac{DV_n^*}{Dt^*} = f^* - \nabla^* p^* + \frac{1}{\mathrm{Re}} \nabla^{*2} V_n^* \tag{2-14}$$

where $V_n^* = V_n/V$, $t^* = tV/L$, $\nabla^* = L\nabla$, $f^* = fL/V^2$, and $p^* = p/\rho V^2$ where V is characteristic velocity, L is characteristic length, and Reynolds number, Re, which relates the relative strength of steady inertial forces to viscous forces $\mathrm{Re} = \rho VL / \mu$. A large Reynolds number indicates the flow is dominated by inertial forces. Therefore, we can assume the flow to be inviscid flow. If Reynolds number is small, the flow can be assumed to be a viscous flow or Stokes flow

(creeping flow). Reynolds number also plays an important character for discrimination between laminar and turbulent flow. For pipe flow, Re less than 2100 will be laminar flow, and Re above 4000 will be turbulent flow. For boundary layer flow, Re less than 10^5 will be laminar flow, and Re above 3×10^6 will be fully turbulent flow.

For a compressible Newtonian fluid, the unsteady Navier-Stokes equations are:

$$\begin{aligned}&\frac{\partial\rho}{\partial t}+V_n\cdot\nabla\rho+\rho\nabla\cdot V_n=0\\&\rho\frac{\partial V_n}{\partial t}+\rho(V_n\cdot\nabla)V_n=\rho f-\nabla p+\mu[\nabla^2V_n+\frac{1}{3}\nabla(\nabla\cdot V_n)]\end{aligned}\tag{2-15}$$

2.2.2 Turbulence Model

For turbulent flow, the Navier-Stokes equations cannot be applied without modification. The Reynolds-averaged approach is the most interesting scheme to deal with turbulent flow. This approach separates the turbulent velocity for mean and fluctuating parts, i.e. $V_n=\overline{V_n}+V_n^{'}$, where V_n is the instantaneous velocity, $\overline{V_n}$ is the mean velocity, and $V_n^{'}$ is the fluctuation velocity. Based on the time average for stationary turbulent flow, $\overline{V_n}$ may be defined:

$$\overline{V_n}=\frac{1}{\Delta t}\int_{t-\Delta t}^{t+\Delta t}V_n(x,y,z,t)dt\tag{2-16}$$

where Δt is the time interval compared with the maximum period of turbulent flow. Applying the time-averaged approach in equations (2-10) and (2-13), the incompressible Reynolds-Average Navier-Stokes equations for Newtonian fluid become:

$$\begin{aligned}&\frac{\partial\overline{V_{nj}}}{\partial x_j}=0\\&\rho\frac{D\overline{V_{nj}}}{Dt}=\rho\overline{f_j}-\frac{\overline{\partial p}}{\partial x_j}+\mu\frac{\overline{\partial V_{nj}}}{\partial x_i}+\frac{\partial\left(-\rho\overline{V_{nj}^{'}V_{ni}^{'}}\right)}{\partial x_i}\end{aligned}\tag{2-17}$$

where $\left(-\rho\overline{V_{nj}^{'}V_{ni}^{'}}\right)$ is the Reynolds stress. In Fluent [67], we use a two-equation k-ε model to describe Reynolds stress for the problem of plasma actuated film cooling. Many researchers have developed k-ε models over several years. We applied the renormalization group (RNG) k-ε model to improve accuracy for rapid strained and swirling flows. The RNG k-ε model has a similar form to the standard k-ε model proposed by Launder and Sharma [68]:

$$\begin{aligned}
&\frac{\partial}{\partial t}(\rho k)+\frac{\partial(\rho k V_{ni})}{\partial x_i}=\partial(\alpha_k \mu_{eff}\frac{\partial k}{\partial x_j})/\partial x_j+G_k+G_b-\rho\varepsilon-Y_M+S_k \\
&\frac{\partial}{\partial t}(\rho \varepsilon)+\frac{(\rho \varepsilon V_{ni})}{\partial x_i}=\partial(\alpha_\varepsilon \mu_{eff}\frac{\partial \varepsilon}{\partial x_j})/\partial x_j+C_{1\varepsilon}\frac{\varepsilon}{k}(G_k+C_{3\varepsilon}G_b)-C_{2\varepsilon}^{*}\rho\frac{\varepsilon^2}{k}+S_\varepsilon
\end{aligned} \tag{2-18}$$

where k is the turbulent kinetic energy, ε is the turbulent dissipation, G_k represents the generation of turbulent kinetic energy due to the mean velocity gradients, G_b is the generation of turbulent kinetic energy, Y_M represents the contribution of the fluctuating dilatation in compressible turbulence to the overall dissipation rate, α_k and α_ε are the inverse effective Prandtl numbers for k and ε, S_k and S_ε are user defined source terms, and $C_{1\varepsilon}$, $C_{2\varepsilon}^{*}$, and $C_{3\varepsilon}$ are model constants.

2.2.3 Slip Velocity Regime

In the microscale regime, the continuum approach with the no-slip boundary condition may not hold when the Knudsen number (Kn) is greater than 0.1. The Knudsen number which is a normalized factor is defined as the ratio of the fluid mean free path λ and macroscopic characteristic length Λ, i.e. Kn = λ/Λ. As Kn increases, the rarefaction effects become more dominant between the bulk of the fluid and the wall surface. This results in a finite slip velocity at the wall which is known as the slip flow regime. In this regime, the flow is governed by the Navier-Stokes equations, and the rarefaction effects are modeled by Maxwell [69] which derived the first-order slip relation for dilute gases. Table 2-1 describes different regimes of fluid flow

depending on the Knudsen number. For Kn between 10^{-2} and 10, we can implement the boundary conditions for the momentum and energy equations. The slip wall boundary condition for an ideal gas is as follows [70]:

$$V_n - V_{wall} = \frac{2-\sigma_V}{\sigma_V}\lambda\left(\frac{\partial V_n}{\partial y}\right)_w + \frac{3}{4}\frac{\mu}{\rho T_{\text{gas}}}\left(\frac{\partial T}{\partial x}\right)_w \tag{2-19}$$

where σ_V is tangential momentum accommodation coefficient. The second term on the right hand side is known as *thermal creep* which generates slip velocity in the direction opposite to the increasing temperature. Smoluchowski's [71] temperature jump boundary condition is as follows:

$$T_n - T_{wall} = \frac{2-\sigma_T}{\sigma_T}\left(\frac{2\gamma}{\gamma+1}\right)\frac{\lambda}{\text{Pr}}\left(\frac{\partial T_n}{\partial y}\right)_w \tag{2-20}$$

where V_n and T_n are the velocity and temperature of the gas adjacent to the wall, while V_{wall} and T_{wall} are the wall velocity and the wall temperature in equations (2-19) and (2-20), σ_T is thermal accommodation coefficient, Pr is the Prandtl number, i.e. Pr $= c_p\mu / k_c$, where c_p is the specific heat and k_c is the thermal conductivity. The value of the coefficients σ_V and σ_T depends on the surface finish, the fluid temperature, and local pressure.

Table 2-1. Knudsen number regimes

Range, Kn	Flows	Equations
$0 \sim 10^{-2}$	Continuum flow	No-slip Navier-Stokes
$10^{-2} \sim 10^{-1}$	Slip flow	Slip Navier-Stokes
$10^{-1} \sim 10^{1}$	Transition flow	Burnett equations
$10^{1} \sim \infty$	Free-molecule flow	Boltzmann equations

Note: See [70] for more information.

2.3 Finite Element Formulation

The finite element method (FEM) is a popular technique used for solving partial differential equations (PDE) approximately. The FEM is based on the weak formulation of the PDE, and strives to approximate the solution of the PDE. For finite difference (FD) or finite volume methods (FVM), both methods are approximating the governing equations. In the FEM the domain is divided in several sub-domains called elements. The method treats the problem at an element-level basis, and the solution in each element is constructed from the basis function. The FEM has several advantages that make it very attractive for the solution of transport problems. Some of these advantages are simplicity for dealing with different meshes (e.g. triangular or quadrilateral) and order of elements (e.g. linear or quadratic), and hence for dealing with complex geometries. Also, it is easy for dealing with complex Neumann (flux) or Robin (convection) boundary conditions.

The numerical simulation of this dissertation is anchored in an existing finite element based Multi-scale Ionized Gas (MIG) flow code. It has been utilized for a range of applications including electric propulsion, micro or nanoscale flows, fluid dynamic, and plasma physics [19, 20, 23, 63, 70].

2.3.1 Galerkin Weak Statement

The fundamental principle underlying the finite element method is the construction of a solution approximation as a series of assumed test functions multiplied by a set of unknown expansion coefficients, such as the Galerkin Weak Statement (GWS) [72-73]. Such weak form has the effect of relaxing the problem. We are finding a solution that satisfies the strong form on average over the domain instead of finding an exact solution. Any real world smooth problem

distributed over a domain x_j can be approximated as a Taylor series of known coefficients a_i and functions $\psi_i(x_j)$:

$$G(\gamma) = \sum_i a_i \psi_i(x_j) \tag{2-21}$$

The plasma governing equations (2-5)-(2-7) can be written generally as $G(\gamma) = 0$ where γ is the vector containing N_i, N_e, and ϕ. The GWS approach requires that the measure of the approximation error should vanish in an overall integrated sense. This gives a mathematical expression for the minimization of the weighted residual over the domain. We can consider the weak form of Poisson equation (2-7) in one-dimension:

$$WS = \int_0^L \left(\frac{d^2\phi}{dx^2} - S \right) w dx = 0 \tag{2-22}$$

$$\int_0^L \frac{d^2\phi}{dx^2} w dx = \int_0^L S w dx \tag{2-23}$$

where $S = e(n_e - n_i)/\varepsilon_0$ is the source term and w is the weighted basis function. The basis function is chosen orthogonal to the trial function in the GWS to ensure minimum solution error. We can perform integration by parts for equation (2-23) at left hand side:

$$\int_0^L \frac{d^2\phi}{dx^2} w dx = \left[w(x) \frac{d\phi}{dx} \right]_{x=0}^{x=L} - \int_0^L \frac{d\phi}{dx} \frac{dw}{dx} dx = w(L) \left. \frac{d\phi}{dx} \right|_{x=L} - w(0) \left. \frac{d\phi}{dx} \right|_{x=0} - \int_0^L \frac{d\phi}{dx} \frac{dw}{dx} dx \tag{2-24}$$

We can see the above equation satisfies Neumann boundary conditions automatically.

2.3.2 Basis Functions

The basis function approximates the test and trial functions within each element. The finite element basis N_k can be Chebyshev, Lagrange or Hermite interpolation polynomials, and the degree k is based on the one-, two- or three- dimensional problem. The integrated variables γ (i.e. N_i, N_e, ϕ) can be represented as the union of temporally and spatially discretized elements.

For the two-dimensional microscale discharge simulation in chapter 3, the biquadratic (9-node) basis functions $N_k(s,t) = [N_1\, N_2\, N_3\, N_4\, N_5\, N_6\, N_7\, N_8\, N_9]$ are required for a better convergence shown in Fig. 2-1(A). For the case of three-dimensional micro plasma pump in chapter 4, we choose a tri-linear (8-node) basis functions $N_k(r,s,t) = [N_1\, N_2\, N_3\, N_4\, N_5\, N_6\, N_7\, N_8]$ shown in Fig. 2-1(B). It is customary to use the isoparametric coordinate system for the basis function when dealing with a complex geometry.

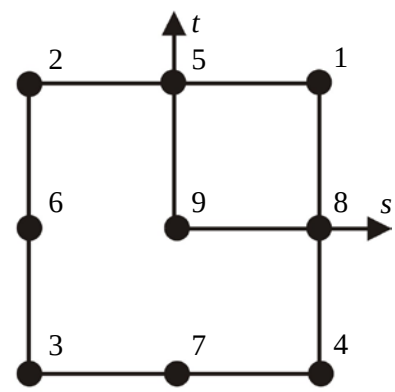

$$\{N(s,t)\}^T = \frac{1}{4}\begin{Bmatrix} st(1+s)(1+t) \\ -st(1-s)(1+t) \\ st(1-s)(1-t) \\ -st(1+s)(1-t) \\ 2t(1+t)(1-s^2) \\ -2s(1-s)(1-t^2) \\ -2t(1-t)(1-s^2) \\ 2s(1+s)(1-t^2) \\ 4(1-t^2)(1-s^2) \end{Bmatrix}$$

A)

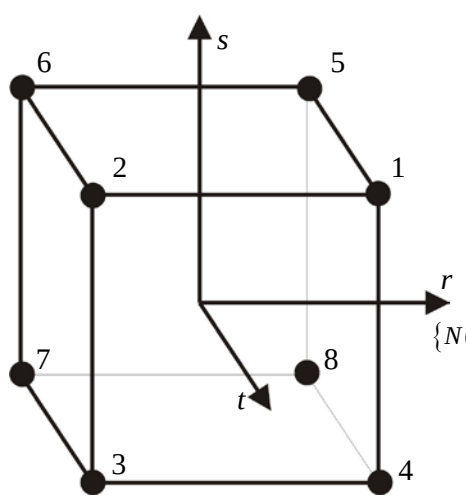

$$\{N(r,s,t)\}^T = \frac{1}{8}\begin{Bmatrix} (1+r)(1+s)(1+t) \\ (1-r)(1+s)(1+t) \\ (1-r)(1-s)(1+t) \\ (1+r)(1-s)(1+t) \\ (1+r)(1+s)(1-t) \\ (1-r)(1+s)(1-t) \\ (1-r)(1-s)(1-t) \\ (1+r)(1-s)(1-t) \end{Bmatrix}$$

B)

Figure 2-1. Isoparametric representation of basis functions for A) biquadratic (9-node) quadrilateral element and B) tri-linear (8-node) element.

For Galerkin's method, we can assume $\phi(x) = \sum_j \gamma_j N_j(x)$ and $w(x) = \sum_k \beta_k N_k(x)$ where γ_j is unknown variable and β_k is arbitrary weighting function. We can rewrite the equation (2-24) based on the above assumption as well as zero boundary value:

$$\int_0^L \sum_j \gamma_j \frac{dN_j}{dx} \sum_k \beta_k \frac{dN_k}{dx} dx = \int_0^L -S \sum_k \beta_k N_k(x) dx \tag{2-25}$$

After rearrangement and cancelation, equation (2-25) becomes $\sum_j \gamma_j K_{kj} = F_k$ where

$K_{kj} = \int_0^L \frac{dN_j}{dx} \frac{dN_k}{dx} dx$ is a n x n symmetric stiffness matrix and $F_k = \int_0^L -SN_k dx$ is a n x 1 vector.

2.3.3 Numerical Integration

Once the basis functions are defined, the interior (volume) and boundary (surface) integrals required in the finite element formulation are evaluated approximately using the Gauss-Legendre quadrature rule [74]:

$$\begin{aligned} I_{1D} &= \int_{-1}^{1} f_i(t)dt \sim \sum_{i=1}^{n} w_i f(t_i) \\ I_{2D} &= \int_{-1}^{1} f_{ij}(t,s)d \sim \sum_{i=1}^{m} \sum_{j=1}^{n} w_i w_j f_{ij}(t_i, s_j) \\ I_{3D} &= \int_{-1}^{1} f_{ijk}(t,s,r)d \sim \sum_{i=1}^{m} \sum_{j=1}^{n} \sum_{k=1}^{p} w_i w_j w_k f_{ijk}(t_i, s_j, r_k) \end{aligned} \tag{2-26}$$

Table 2-2 shows nodes and weights for numerical integration up to ftfth order n, which can be exact for a polynomial of degree (2n-1) or less. Therefore, each integral is replaced by a summation of the argument of the integral multiplied by a given integration weight w_i for a given number of integration points t_i.

Table 2-2. Gauss-Legendre quadrature; nodes and weights (t_i, w_i)

Order, n	Nodes, t_i	Weights, w_i
1	t_1 = 0	w_1 = 2
2	t_1 = -0.577350	w_1 = 1
	t_2 = 0.577350	w_2 = 1
3	t_1 = -0.774597	w_1 = 0.555556
	t_2 = 0	w_2 = 0.888889
	t_3 = 0.774597	w_3 = 0.555556
4	t_1 = -0.861136	w_1 = 0.347854
	t_2 = -0.339981	w_2 = 0.652145
	t_3 = 0.339981	w_3 = 0.652145
	t_4 = 0.861136	w_4 = 0.347854
5	t_1 = -0.906180	w_1 = 0.236927
	t_2 = -0.538469	w_2 = 0.478629
	t_3 = 0	w_3 = 0.568889
	t_4 = 0.538469	w_4 = 0.478629
	t_5 = 0.906180	w_5 = 0.236927

Note: See [74] for more information

2.3.4 Solution Approach

The forward temporal evolution is evaluated using the fully implicit ($\theta = 1$) time stepping procedure. The Newton-Raphson scheme is used for dealing with nonlinear terms. To solve the sparse matrix, we apply an iterative sparse matrix solver called Generalized Minimal RESidual (GMRES) [75]. The assembly procedure involves storing only the non-zero elements of the matrix (Jacobian, $\partial R / \partial q$) in the form of a linear array and the corresponding row and column locations using an incremental flag. The solution is assumed to have converged when the L_2 norms of all the normalized solution variables and residuals are below a chosen convergence criterion.

2.3.5 The MIG Flow Code

A finite element based module driven Multi-scale Ionized Gas (MIG) flow code has been developed and verified with one-, two- and three-dimensional problems, including fluid dynamics and heat transfer related problems, micro/nanoscale flow, specifically to modeling DC/RF induced dielectric barrier discharges, and designing electromagnetic propulsion thrusters.

Computed solutions show details of the distribution of charged and neutral particles and their effects on the flow dynamics for the above applications. Here is flow chart for MIG flow code shown in Fig. 2-2, where the detailed information for the input file is described in Appendix A.

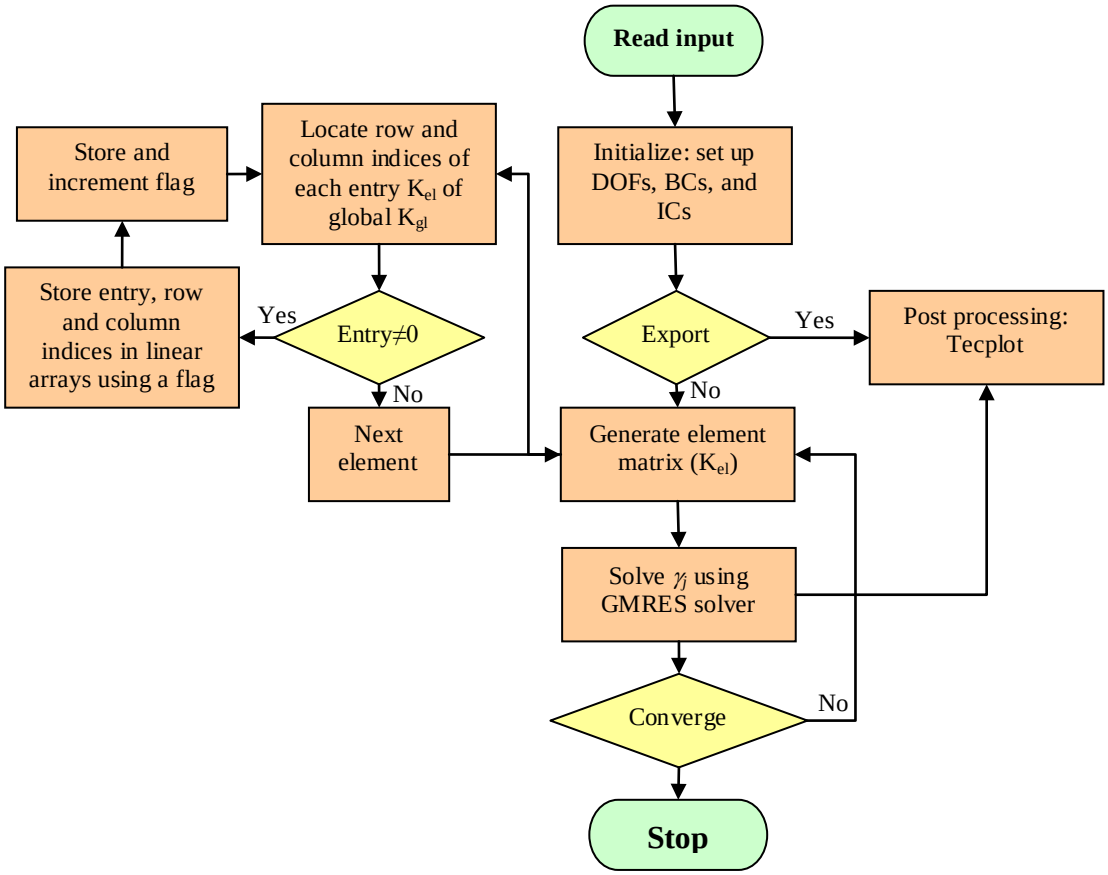

Figure 2-2. Flow chart for Multi-scale Ionized Gas (MIG) flow code.

2.4 Macroscale Results

Many similar physics of plasma actuators exist in both macro and microscale. In macroscale, we study the physics of plasma actuators based on the phenomenological model and the reduced order method in the following sections. The results for microscale discharge based on the first-principles approach will be presented in chapter 3.

2.4.1 Film Cooling

In gas turbine blades, fluid film based cooling becomes mandatory to protect the blades from high thermal stresses induced by hot combustion gases and thus increasing the blade lifetime. In this process, cold gas is injected from a row of holes located spanwise into the hot crossflow. The penetration of the cold jet into the main flow creates a three-dimensional flow field entraining some hot gas to bend towards the blade. We study the geometry shown in the Fig. 2-3(A) schematic [16-18]. This schematic shows hot air passing over a flat surface (e.g., a turbine blade). This surface of study has a row of injection holes through which the cool air is issued at an angle α_a = 35°. The cool jet at temperature T_j =150 K is injected into the hot freestream of T_{fs} =300 K. The injection ducts are circular pipes with diameter equal to d = 2.54 mm. The injection hole formed by the intersection of the injection pipe with the wind tunnel is an ellipse with the minor and the major axes. The distance between the hole centers is 3d. The selected mean flow velocities, static pressures and temperatures (i.e., densities) in the injection pipe and the wind tunnel gives a blowing ratio $M = \rho_j V_j / \rho_{fs} V_{fs} = 1$. The inlet section is located at x = -20d and the exit at x = 29d. The flat (blade) surface is considered adiabatic. The domain extends from the plenum base at y = -6d to y = 20d from work surface where a pressure-far-field boundary condition was applied. The periodic boundary condition was applied in the crosswise direction (at $z = \pm 1.5d$) in the computational domain. For the coolant plenum, we applied no-slip wall condition on x/d = -14 and 8 and y/d = -2 surfaces, and mass flow inlet condition for y/d = -6. The plasma actuator can be made of a set of electrode pairs as shown in Fig. 2-3(B) between which electric potential and induced weak ionization of the working gas generate an electric body force that is dominant inside the boundary layer. Because of geometry in such an actuator, the electrohydrodynamic body force field is three dimensional. The induced flow actuation is

directly linked with the gas-charged particle interaction and is thus instantaneous. Fig. 2-3(C) shows schematics of various hole shapes: A- baseline, B- bumper with 0.5*d* height, C- jet hole with compound slopes, and D- rectangular slot.

The film cooling performance is measured by an effectiveness parameter $\eta(x,y) = (T_{fs} - T_s(x,y))/(T_{fs} - T_j)$, where $T_s(x,y)$, T_j and T_{fs} are the work surface, cooling jet and hot freestream gas temperatures, respectively.

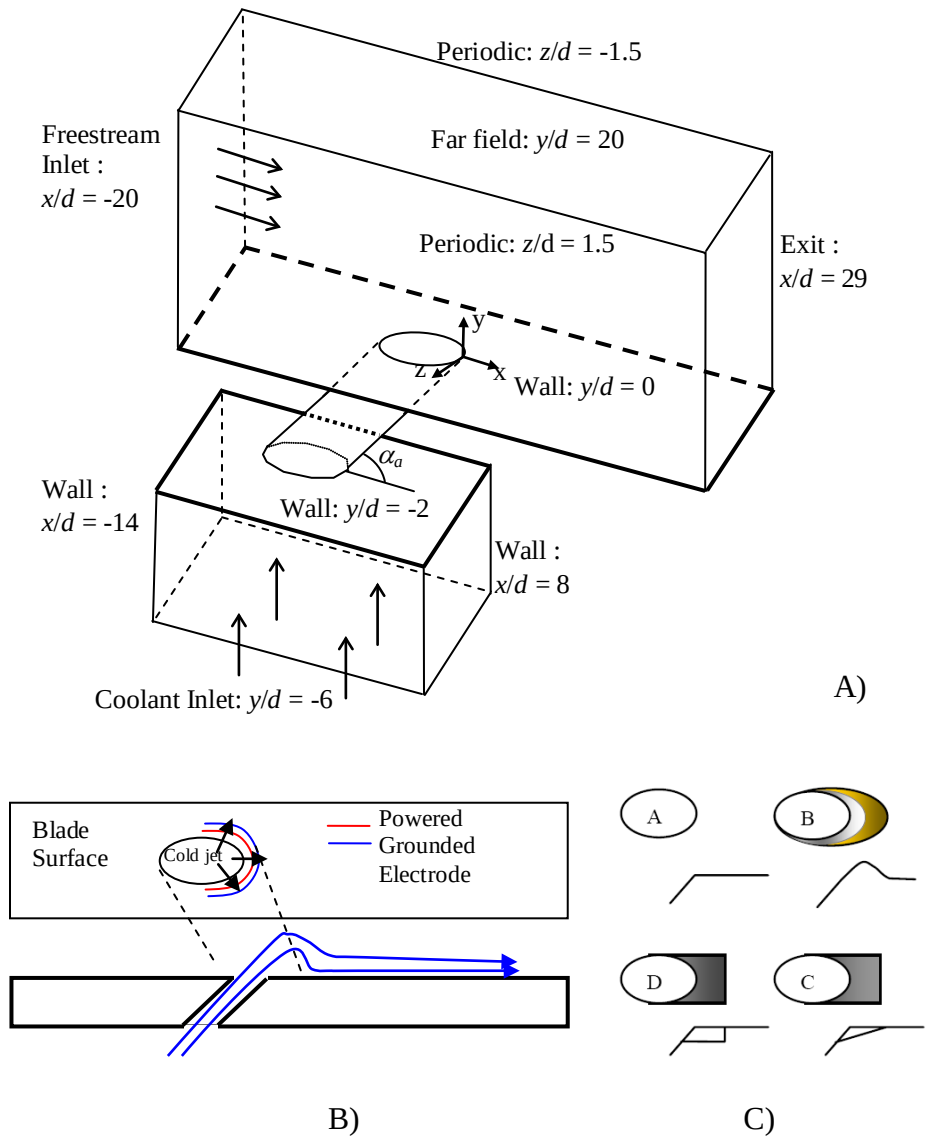

Figure 2-3. Schematics of film cooling using plasma actuated heat transfer and geometric modification for A) film cooling simulation geometry, B) adiabatic flat plate with plasma actuator, and C) cooling hole geometric modification types A through D.

We apply the time average of the electric force shown in Fig. 2-4. $\mathbf{F} = 6\Lambda_f \hat{i} - 3\Lambda_f \hat{j} \pm \Lambda_f \hat{k}$ where Λ_f = f_x*f_y*f_z with $f_x = \left((x-d/2)^2 + C_1\right)/C_2$, $f_y = \left(\exp(-1000y)/C_3\right) - C_4$, $f_z = \left((z-d/2)^2 + C_5\right)/C_6$ based on the phenomenological model. The amplitude Λ_f is varied from 0 to 7500 kN/m^3 with an increment of 1500 kN/m^3 for C_1 = 1.5×10^{-6}, C_2 = 3.09×10^{-6}, C_3 = 0.98, C_4 = 0.057, C_5 = 1.58×10^{-6}, and C_6 = 3.14×10^{-6}.

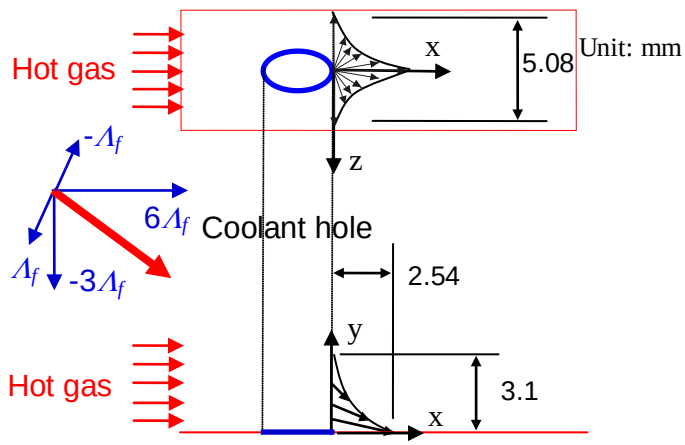

Figure 2-4. Directional distribution of force density.

Using the above phenomenological force model, the three-dimensional fluid description is solved by a commercial Computational Fluid Dynamics (CFD) package, FLUENT^{TM} 6.3.26, based on the finite volume method. According to the experiments, the flow is compressible and fully turbulent. The Reynolds number based on the hole diameter and inlet conditions was 16100. We used the ideal gas approximation and the Advection Upstream Splitting Method AUSM solver closed with the ReNormalized Group (RNG) k-ε turbulence model with a standard wall function. The courant number was set equal to 1 for solution control. A second-order upwind discretization method was used. Convergence was determined when the residual among the continuity, momentum, energy, turbulent kinetic energy, and turbulent dissipation were less than 10^{-3}. Based on the grid independence study [76], we selected 203665 cells for less

computational cost. The baseline case took 1300 iterations for convergence. The baseline solutions were compared with experimental data and other previous numerical work and were determined to be quite similar.

Fig. 2-5(A) plots the temperature distribution on the vertical mid-plane (z = 0). It is obvious that the lift-off effect causes a significant reduction in effectiveness for the baseline case (i). As we increase the body force density from an initial zero (Λ_f = 0, no force) to a maximum of Λ_f = 7500 kN/m^3 (effective force ~N) the flow completely attaches to work surface. Fig. 2-5(B) shows the temperature distribution on the horizontal work surface (y = 0). Importantly, the actuation force applied in a three-dimensional manner demonstrates successful spreading of the cold film over the flat (blade) surface not only in the streamwise direction but also in the crosswise fashion. As the force density increases from Λ_f = 0 to 7500 kN/m^3, the cold flow attachment has significant effect near the coolant hole.

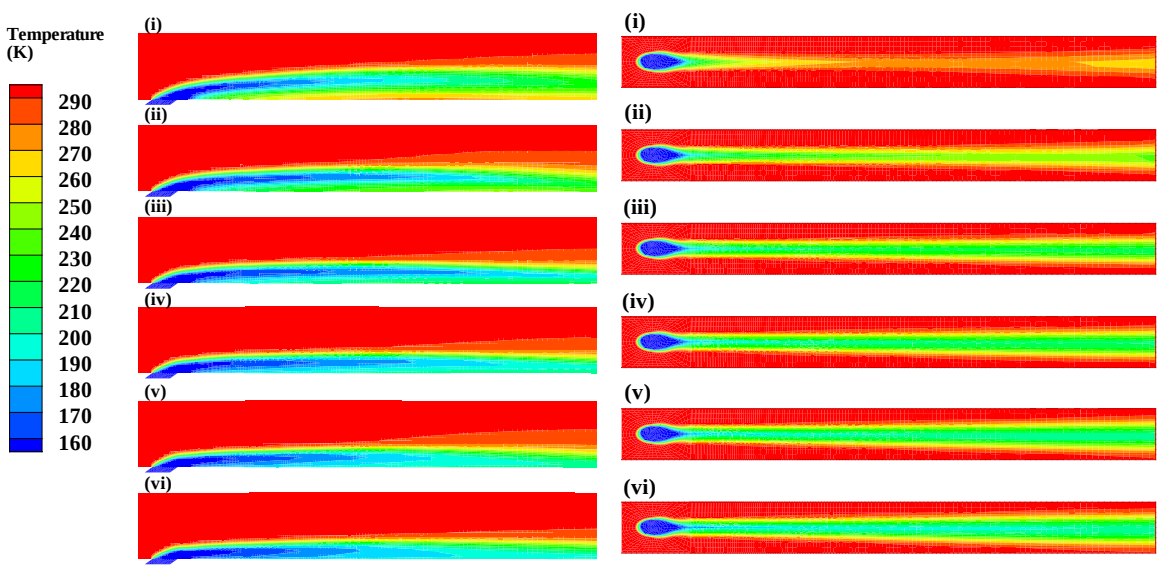

A) B)

Figure 2-5. Temperature contour with different amplitude of actuation force densities Λ_f = (i) 0, (ii) 1500, (iii) 3000, (iv) 4500, (v) 6000, and (vi) 7500 kN/m^3 for A) along the vertical plane at z = 0 and B) on the work surface y = 0.

The effect of plasma discharge on the heat transfer near the work surface is compared in Fig. 2-6 for (A) Λ_f = 0 (plasma off) and (B) 2000 kN/m^3 (plasma on). Fig. 2-6(A) shows the effect of geometric modifications (Λ_f = 0) of the cooling hole. The computed centerline effectiveness η for the baseline case without plasma discharge compares reasonably with the experimental data and other previously reported numerical results. The performance plots of different hole shapes show that C and D have a better η before x/d = 6 because the expansion of the jet reduces the momentum ratio, increasing the cooling performance. Also, the step at the edge of D acts as a trip for the cold fluid inducing more attachment. Interestingly, case B provides a higher η beyond x/d = 20 because the jump effect delays the cold fluid attached to the work surface. In Fig. 2-6(B), the η increases by over 70%, 558%, 137%, and 164% more, respectively, at x/d = 5 than in Fig. 2-6(A), as the force density increases to the maximum (Λ_f = 2000) for designs A-D. It is evident that the plasma flow control guarantees the flow attachment on the surface, improving the heat transfer drastically.

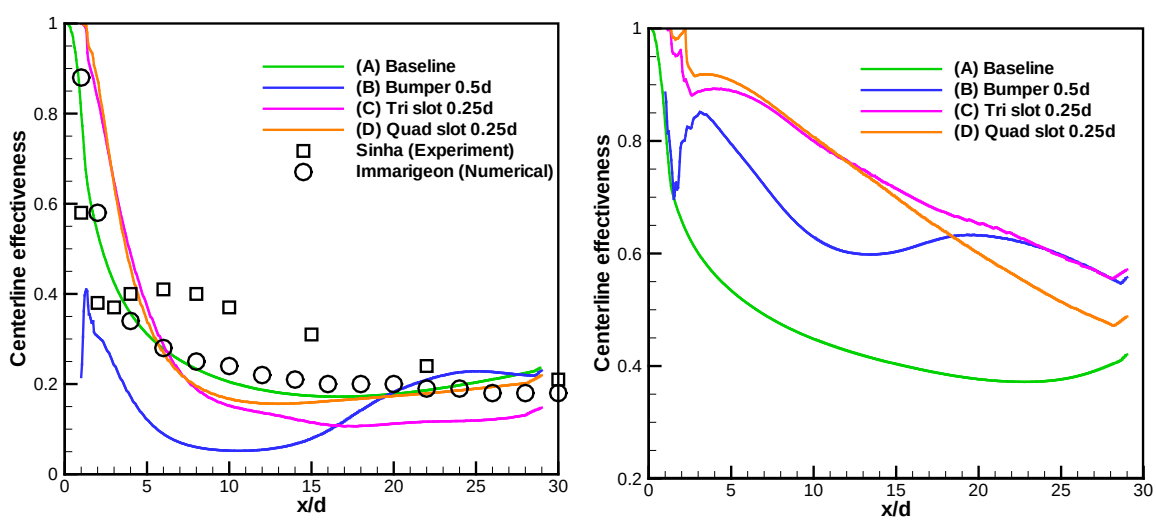

A) B)

Figure 2-6. Effect of plasma actuation on centerline effectiveness for A) Λ_f = 0 and B) Λ_f = 2000 kN/m^3.

Fig. 2-7 shows the evolution of the vortices from x/d = 4 to 16 and presents y-vorticity contours with velocity vector overlays at x/d = 4 for hole shapes A, B, C, and D. The baseline solution for design A shows the typical counter-rotating vortex pair (CVP) with peak vortex strength of about 20,000 s^{-1}. We can see the weaker vortices are moving outward and away from the wall as the distance increases. For design B, the strength of vortex pair doubles to 40,000 s^{-1} with a much larger core diameter. This is due to the tripping of cold jet over the bump. The peak vorticity is a few millimeters above the work surface. Design C shows slightly higher (25, 000 s^{-1}) vorticity than that of A, but this value is substantially lower than that of B or D. In later design the peak is about the same as that of B, however, it is attached to the work surface allowing significantly higher horizontal dispersion of the cooling jet. Fig 2-8 plots the effect of strong downward and forward forces for Λ_f =2000 kN/m^3. For design A, the y-vorticity is lower than that in Fig. 2-7 without plasma effect because the electric force slightly kills the strength of the vortex. Clearly, for designs B–D, the CVP changes their direction from an outward swirl to an inward swirl because the downward momentum induced by the electric force is much larger than the upward momentum of the cooling jet. For design B, the single vortex pair of Fig. 2-8 splits into two separate vortex pairs with equal strength, while for designs C and D the single vortex pair with slightly lower strength (35,000 s^{-1}) shows strong attachment toward the work surface inducing large dispersion of the cold jet. Application of plasma discharge changes the near wall dynamics of flow which is also reflected in heat transfer.

Figure 2-9 plots the temperature distribution on the same planar location (x/d = 4, 10, and 16) and marks y-z plane temperature distribution at x/d = 4 for no actuation Λ_f = 0. At this distance, the cold fluid lifts off in traditional design A. As the distance increases at x/d = 16 for design A, the lift-off effect becomes aggravated. The situation worsens for B just beyond the

bump. However, for C and D the cold jet bends (trips) for modest improvement of the cooling region on the work surface. In contrast, the influence of plasma induced electric force can be significant as seen in Fig. 2-10 for Λ_f = 2000 kN/m^3. The temperature of the work surface reduced for all designs. For design A at x/d = 16, the lowest temperature 230 K on the work surface is much cooler than that in Fig. 2-9 for the same design and location. Clearly (in designs for B, C, and D), the cold jet attaches to the work surface, the extent of which increases from B to C to D. It is thus essential to quantify the improvement in cooling performance.

In conclusion, we explore the advantages of plasma based active heat transfer control for film cooling of a flat work surface. Results demonstrate advantages including three-dimensional dispersion of the cold jet over the work surface without any major loss in flow energy. Based on the numerical prediction, it is evident that application of plasma discharge along with modifications of the hole geometry can culminate into over 100% improvement of the film cooling effectiveness.

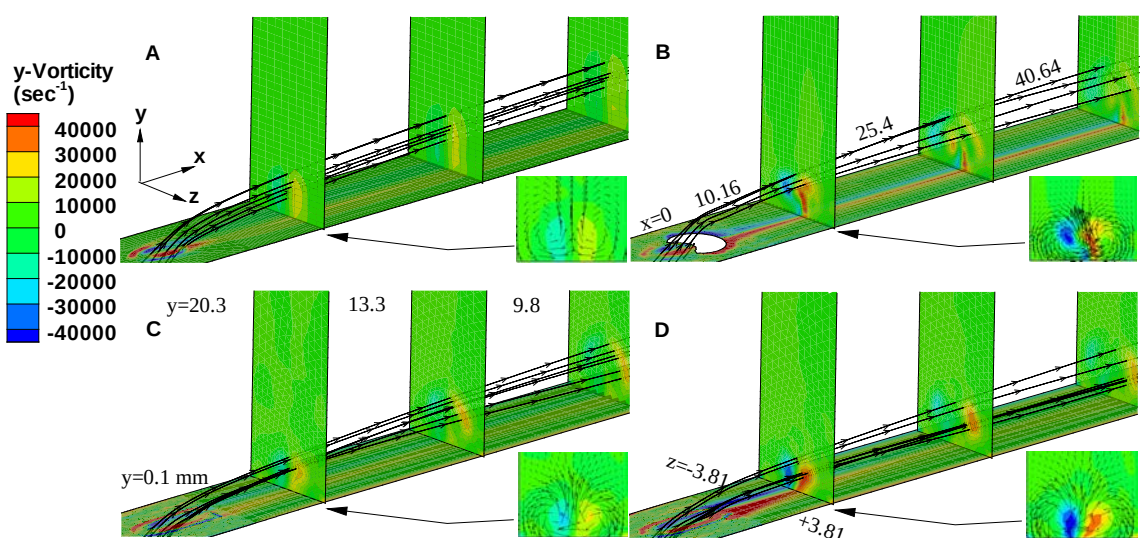

Figure 2-7. Velocity vectors and contours colored by the y-vorticity at x/d = 4, 10, and 16. The inset hole schematics show various shapes for designs A-D.

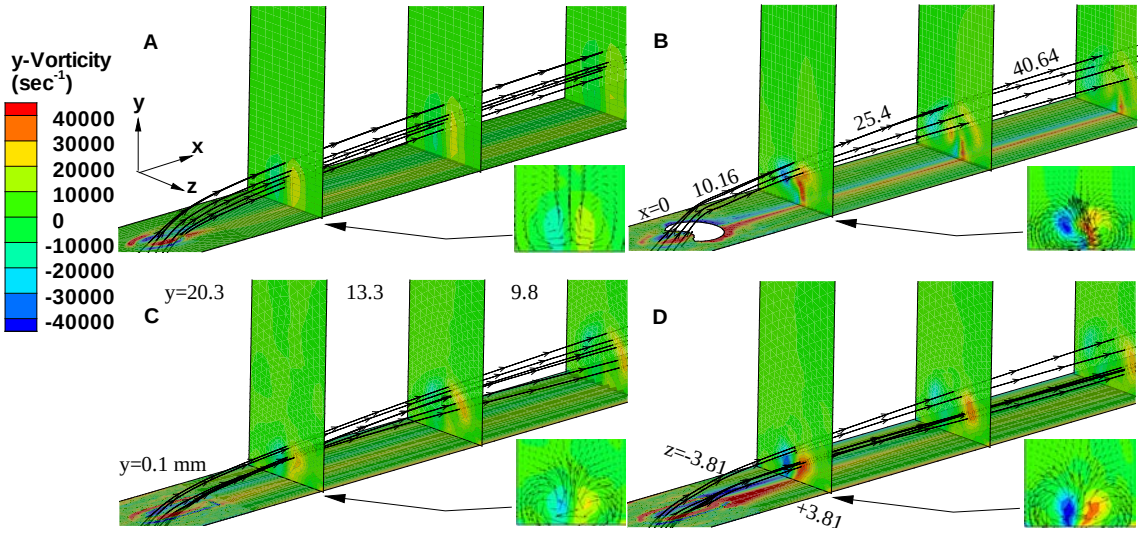

Figure 2-8. Velocity vectors and contours colored by the *y*-vorticity at x/d = 4, 10, and 16 for designs A-D with actuation force density Λ_f = 2000 kN/m^3.

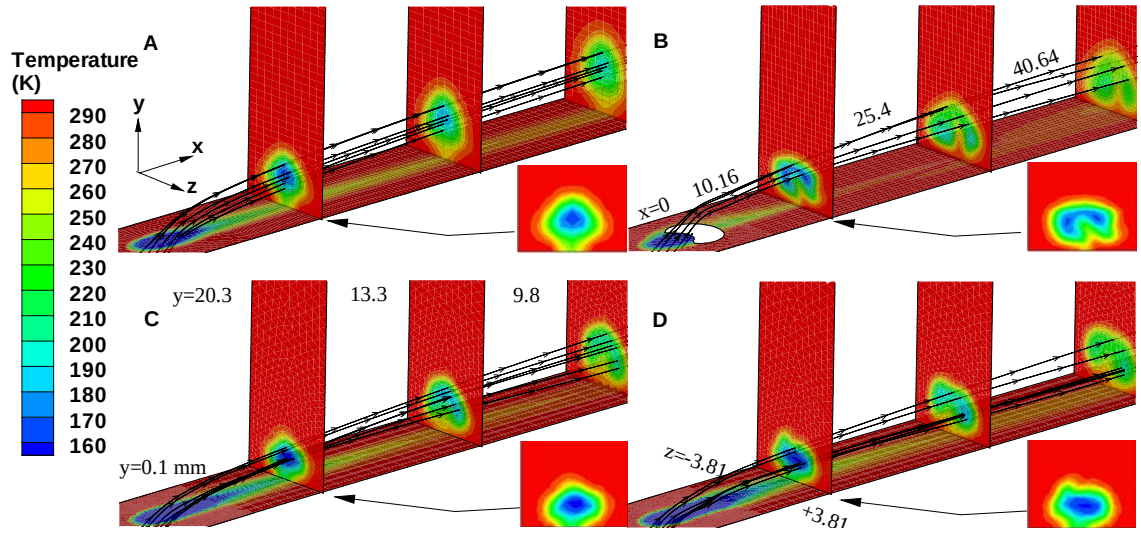

Figure 2-9. Temperature contours at spanwise plane (x/d = 4, 10, and 16) for various designs A-D.

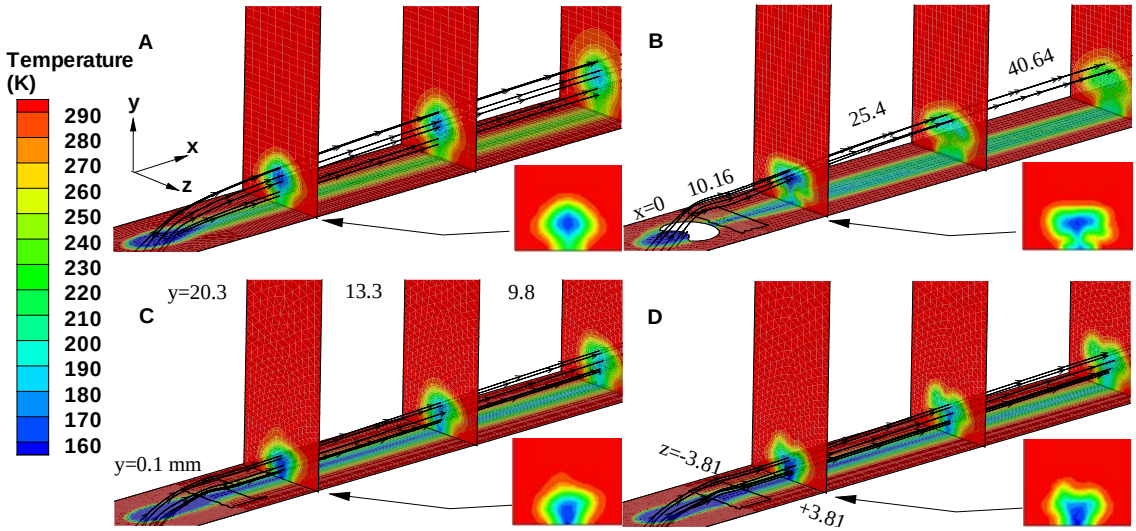

Figure 2-10. Temperature contours at spanwise plane (x/d = 4, 10, and 16) for designs A-D with actuation force density Λ_f = 2000 kN/m^3.

2.4.2 Bulk Flow Control

Surface barrier discharge has been successfully used to control low speed boundary layer flows. Such discharge imparts momentum inside the boundary layer of a fluid in the vicinity of an exposed electrode, and it can be useful for flow separation control [77] shown in Fig. 2-11 or flow turbulization [78] shown in Fig. 2-12.

We introduce a new set of horseshoe and serpentine shaped plasma actuators on a flat surface shown in Fig. 1-10. This picture shows an inward discharge for the horseshoe actuator and a combination of inward and outward discharges for serpentine actuator. Both designs have zero net mass flux (ZNMF), and the electric force from all three planar directions (except from the upstream) push fluid inward to or outward from the central region.

We have studied eight cases (H1 to H4 for Horseshoe and S1 to S4 for Serpentine) with different flow directions and polarities shown in Fig. 2-13. The first-principles based

electrodynamic force has been approximated by Singh and Roy [21]. We use the modified electric force equation based on the reduced order method in equation (2-27).

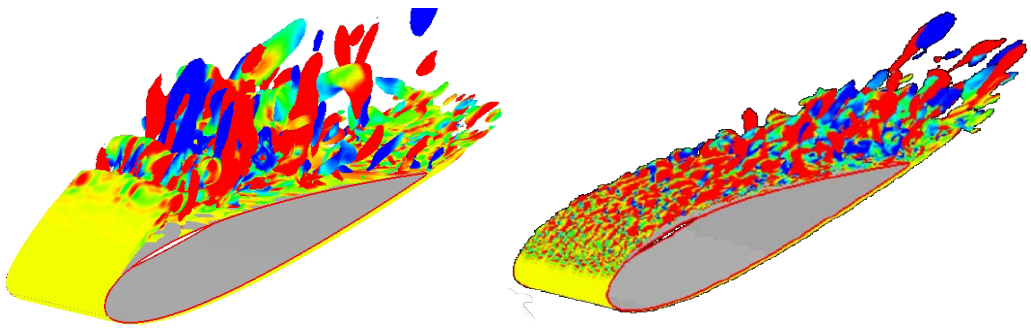

A) B)

Figure 2-11. Flow separation control with vorticity magnitude colored by the spanwise component of vorticity on the airfoil for A) plasma off and B) plasma on [77].

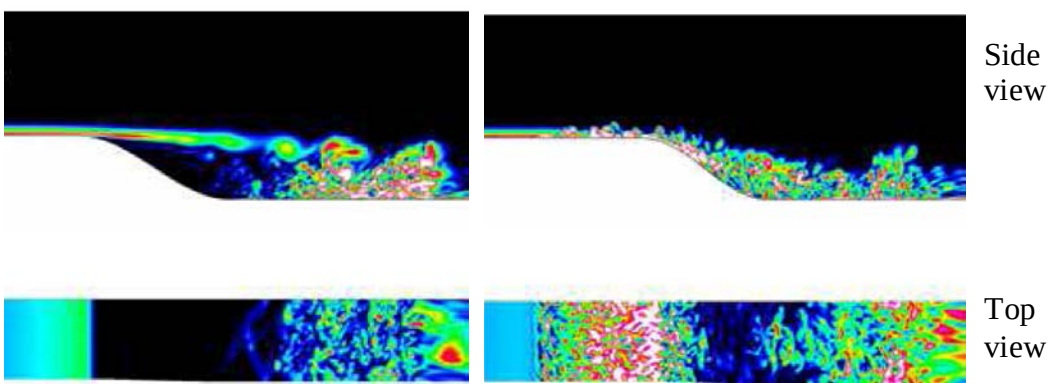

A) B)

Figure 2-12. Laminar flow turbulization over a separation ramp with vorticity magnitude for A) plasma off and B) plasma on [78].

$$\begin{aligned}\mathbf{F} &= C*\mathrm{F}_{x0}*\phi_0^4*\exp[-((\mathrm{r}-\mathrm{r}_0-(\mathrm{z}-\mathrm{z}_0))/\mathrm{z})^2-\beta_x(\mathrm{z}-\mathrm{z}_0)^2]\hat{i}\\ &+C*\mathrm{F}_{y0}*\phi_0^4*\exp[-((\mathrm{r}-\mathrm{r}_0-(\mathrm{z}-\mathrm{z}_0))/\mathrm{z})^2-\beta_y(\mathrm{z}-\mathrm{z}_0)^2]\hat{j}\\ &+C*\mathrm{F}_{z0}*\phi_0^4*\exp[-((\mathrm{r}-\mathrm{r}_0)/\mathrm{z})^2-\beta_z(\mathrm{z}-\mathrm{z}_0)^2]\hat{k}\end{aligned} \tag{2-27}$$

where C is a scaling factor, F_{x0} , F_{y0} , and F_{z0} are taken from the average electrodynamic force obtained by solving the air-plasma equations. The functional relationship with the fourth power

of potential ϕ_0 = 800 V to the exposed electrode is based on the plasma simulation. The values of β_x, β_y, and β_z are functions of the dielectric material and correlated to match the velocity induced by the electrodynamic force.

We ignore the height of the powered electrode and dielectric on the flat plate. At the freestream inlet (y = -100 mm), a uniform velocity of 10 m/s was applied. At the exit plane (y = 100 mm), the gauge pressure at the outlet boundary was maintained at 0 Pa. We applied a no-slip wall condition on the flat plate surface z = 0. The symmetry boundary condition was applied in the crosswise direction x = ± 100 mm and the top of the computational domain z = 100 mm. For both the horseshoe and serpentine plasma actuators, we imposed the time averaged body force vectors with the purple arrow shown in Fig. 2-13. Depending on the actuation device, a local force density (kN/m^3) may be obtained by spending a few watts.

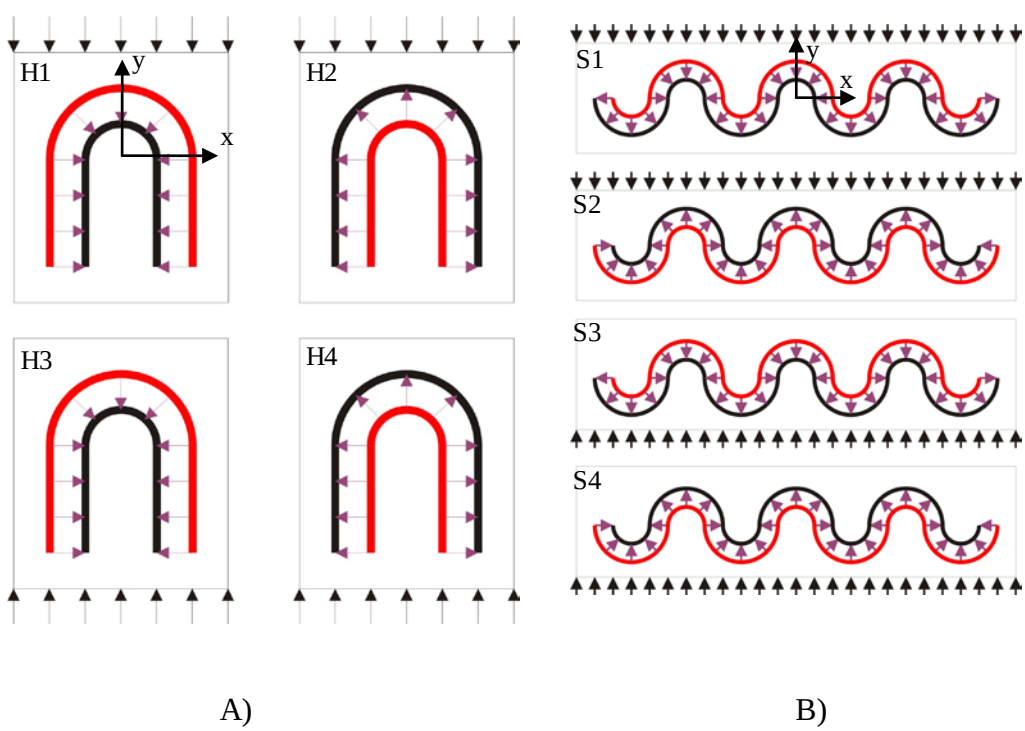

Figure 2-13. Top view of actuators with different flow and plasma electric force directions for A) horseshoe and B) serpentine.

The established three-dimensional mathematical model was solved by the commercial CFD package, FLUENT^{TM}, which is based on the finite volume method. The fluid was air, and we assumed that the flow was incompressible and steady-state laminar flow. The Reynolds number Re = 136917 was based on the length of flat plate y = 200 mm in streamwise direction. A second-order upwind scheme discretization method was used. Fig. 2-14(A) shows the comparison of the streamwise velocity (y-velocity) at x = 0.2 m for four different mesh densities. We can see the y-velocity did not make any difference after we increased the mesh densities in x, y, and z axis. Convergence was determined when the residual was less than 10^{-6} for the continuity and the momentum equations shown in Fig. 2-14(B). We also compared the numerical boundary layer thickness on the flat plate with the exact solution for Blasius boundary layer without plasma actuation. The error showed 1.63% difference. For less computational cost, we selected the mesh case 85x85x38 as our computational grids.

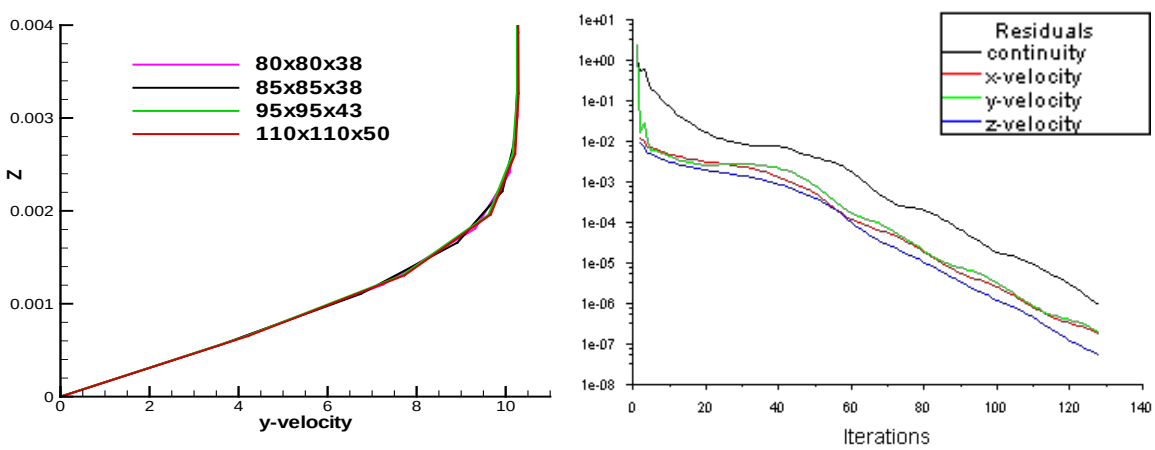

A) B)

Figure 2-14. Grid independent and convergent test for flat-plate boundary layer with A) 4 different mesh densities and B) residuals with continuity and velocity components.

Fig. 2-15(A) describes the effect of the streamwise velocity V_y for the cases H1 to H4 on the yz-plane (x = 0), which show a clockwise vortex induced by plasma actuation in cases H1 and H3, and a counterclockwise vortex generated in cases H2 and H4. For case H3, the inward

plasma actuation accumulated the fluid toward the centerline of the actuator and pinched the fluid going upward past this barrier. The result shows a significant tripping resulting in the local increase in boundary layer thickness. Fig. 2-15(B) shows the velocity V_z for cases H1 to H4 on the vertical mid-plane (y = 0). For cases H1 and H3, there are two vortices generated between the plasma region, and the velocity V_z at the origin is going upward because the fluid is sucked by the plasma actuation between electrodes. For cases H2 and H4, two vortices are generated by induced velocity by which the fluid is pulled toward origin and pushed upward between plasma regions.

Fig. 2-16 plots the streamwise velocity V_y for cases S1 to S4 on the xy-plane (1 mm above the actuator) and shows a very complex pattern of flow because the curve electrodes induce velocity in both streamwise and crosswise directions rather than only in one direction for the standard parallel electrodes.

In conclusion, we introduced the surface compliant horseshoe and serpentine shaped plasma actuators and numerically demonstrated the momentum injection advantages, including the three-dimensional modification of the flow over the work surface. Based on the different momentum injection arrangements, we showed the usefulness of such actuators for both the tripping mechanism and the separation control as needed. When the outer electrode was powered and the inner electrode was grounded, the resulting inward pinching electrodynamic force extracted momentum and injected it vertically into the bulk fluid. While the outer electrode was grounded and electrical power was applied to the inner electrode, a downward vortical flow was generated to induce the flow attachment to the work surface. More detailed numerical information can be found in our publication [22]. Such predictions need to be validated with physical experiments.

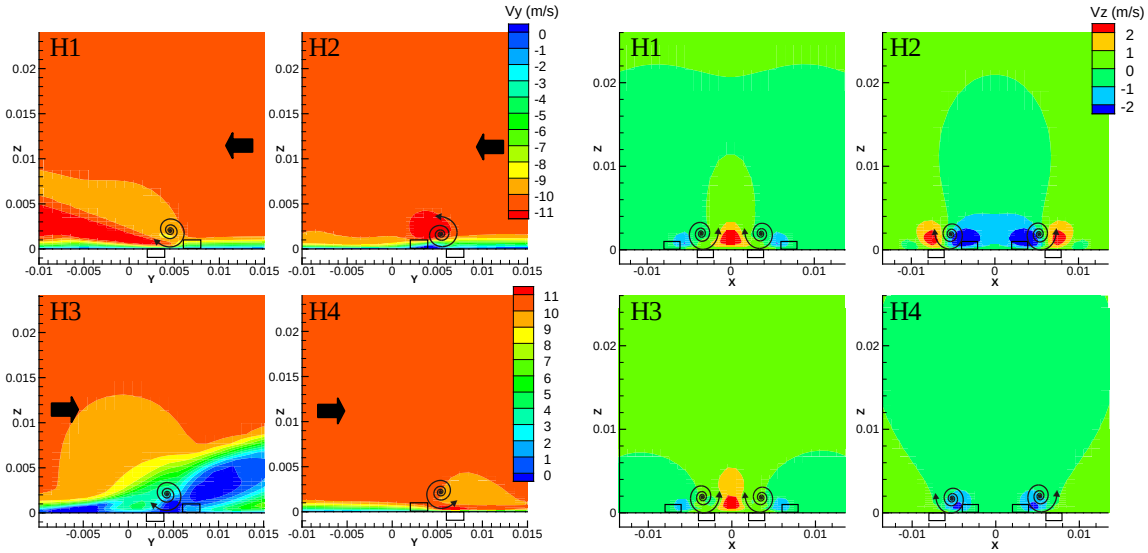

Figure 2-15. Comparison of velocity components with various configurations for H1 to H4 for A) streamwise velocity V_y at $x = 0$ and B) upward velocity V_z at $y = 0$.

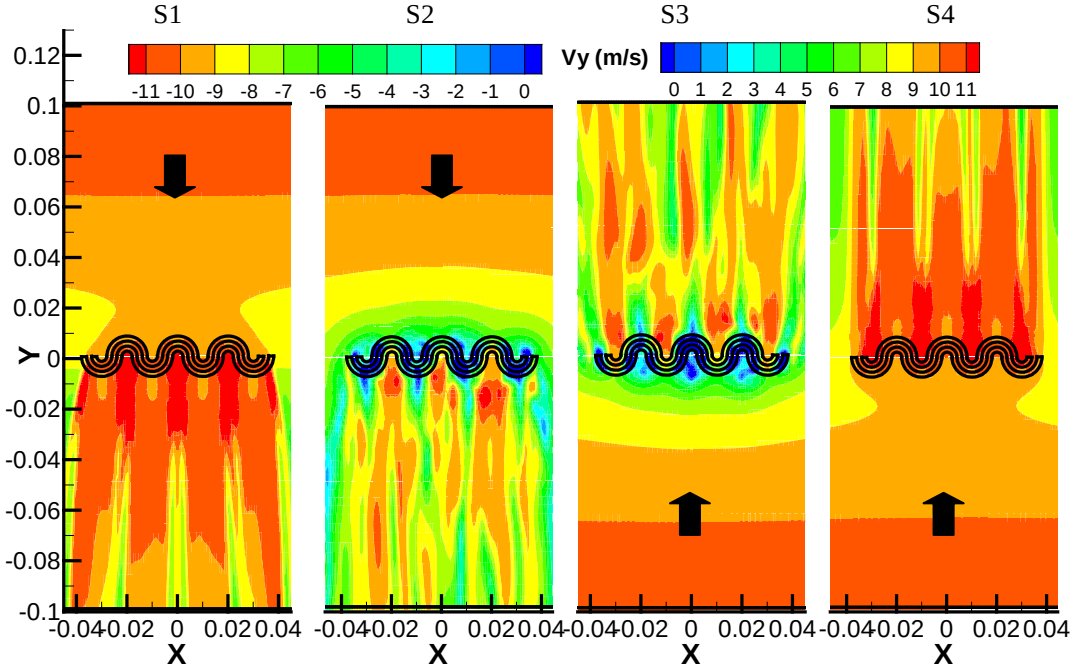

Figure 2-16. Comparison of streamwise velocity V_y for S1 to S4 at $z = 1$ mm.

CHAPTER 3
MICROSCALE VOLUME DISCHARGE

The physics of the plasma actuator in macroscale has been shown in chapter 2. The plasma actuator creates a promising result for actively imparting momentum to the bulk region. For the horseshoe and serpentine actuators, we can use the same actuator for flow attachment or turbulization.

The primary weakness of the DBD actuator is the relatively small actuation effect. Since our interests are in high speed flow control, microscale discharge may be a remedy to generate a large plasma actuation. In this chapter, we explain the challenges in deviation of Paschen's law and set up a problem for a two-dimensional nitrogen microscale volume discharge at atmospheric pressure based on the first-principles approach. The obtained numerical results compare with reported experimental data. The numerical error is also analyzed. We plot the residual versus the iterations for one time step and the total time to check the convergence.

3.1 Challenges and Scopes

Paschen's curve does not matter if the pressure or the electrode distance is changed; smaller dimensions are enabled by higher operating pressures. Deviations from Paschen's theory in microgaps were first reported in the 1950s. Later, researchers [31, 33, 35] found Paschen's law was not valid for gaps of less than 5 μm from experiments shown in Fig. 1-15. They provided an explanation for the deviation based on quantum tunneling of electrons. It is clear that a reduced gap in a submicrometer scale (1-5 μm) will not give us an increase in electric field strength. In this chapter, our goal is to investigate a two-dimensional volume discharge from 200 to 5 μm interelectrode gaps. Finally, numerical results are compared with reported experimental data to verify the plasma model.

3.2 Problem Specification

A direct current (DC) discharge forms plasma, sustained by a DC through an ionized medium shown in Fig. 3-1. A high voltage difference between electrodes results in the electrical breakdown of the gas. These discharges are characterized by continuous steady currents and are mostly sustained by secondary emissions.

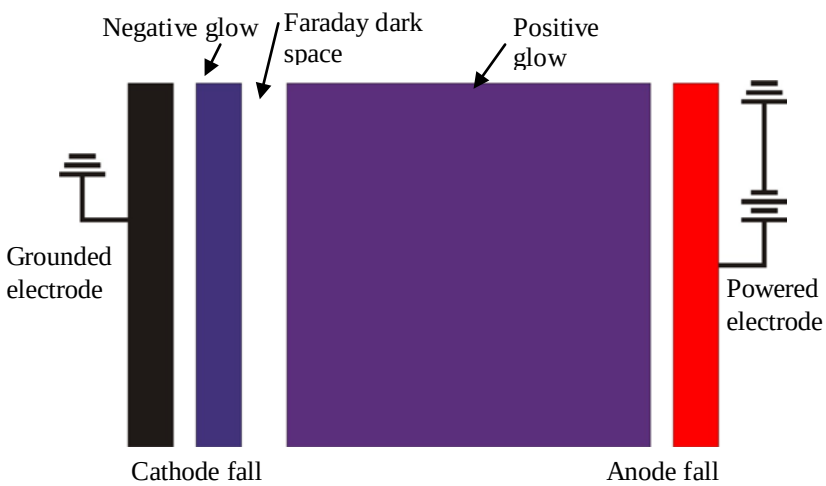

Figure 3-1. Schematic representation of various glows with DC discharge.

We study a two-dimensional parallel plate discharge with microgaps varied from 200 to 5 μm at atmospheric pressure. The working gas is nitrogen (N_2), and the discharge is driven by a voltage of 500 V shown in Fig. 3-2. The plasma governing equations are described in chapter 2.

The computational grid consists of 25×30 biased biquadratic (9-node) quadrilateral elements with non-dimensional length of 0.00049 away from the wall for the first node shown in Fig. 3-3. We neglect the thickness of electrodes at the top and bottom surface. An electrode potential of 500 V is applied through an external circuit. The anode is at $y = 0$, while the cathode is at $y = 0.1$. A vanishing ion density is imposed at the anode, while the electron density at the cathode is calculated from the flux balance using a secondary-emission coefficient. The left and right boundaries of the computational domain are maintained at symmetric conditions. Electrons

and ions distributions are based on the initial condition calculated on the DC sheath solution [79]. A uniform time-step of 10^{-13} seconds is used for the time integration.

3.3 Results Obtained

The simulation results for ion and electron densities along y-direction with various gaps from d_g = 200 to 10 μm at atmospheric pressure (760 Torr) are presented in Fig. 3-4. The variables for y, N_e, and N_i were normalized using the following normalization scheme: $y = d_g / d_l$, $N_e = n_e / n_0$, and $N_i = n_i / n_0$ where reference length d_l varied from 2000 to 100 μm, and reference density $n_0 = 10^{17}$ m^{-3}. By decreasing the gap d_g, the sheath became more dominant to the plasma region. The location of the sheath was roughly at the bifurcation of ion and electron densities. The sheath thickness was a few Debye lengths based on the pressure [80], and Debye shielding confined the potential variation shown in Fig. 3-5. The function of a sheath is to form of potential barrier so that more electrons are confined electrostatically. The potential lines are bent towards the cathode due to a very low density of electrons. This high potential will also drive electrons away from the cathode and form a cathode sheath thickness.

We applied the Newton-Raphson scheme to solve the nonlinear system of equations, and the ideal convergence was quadratic convergence. However, Fig. 3-6 shows the convergence was between linear and quadratic because the Jacobian matrix does not contain the following four terms, i.e. $\partial R_{n_i} / \partial n_e, \partial R_{n_i} / \partial \phi, \partial R_{n_e} / \partial n_i$, and $\partial R_{n_e} / \partial \phi$ in the stiffness matrix of our model.

Fig. 3-7 shows that the computed electric field compared with the published experimental data [33] with a very good agreement from 50 to 5 μm interelectrode gaps. The computed charge eq slightly decreased as the gap d_g decreased, but it increased at the gap below 10 μm

because much less electrons exist in the plasma region. Based on the calculation of the electric force $F_y = eqE_y$, the highest force density was around 6.8 MN/m^3 at 5 μm gap.

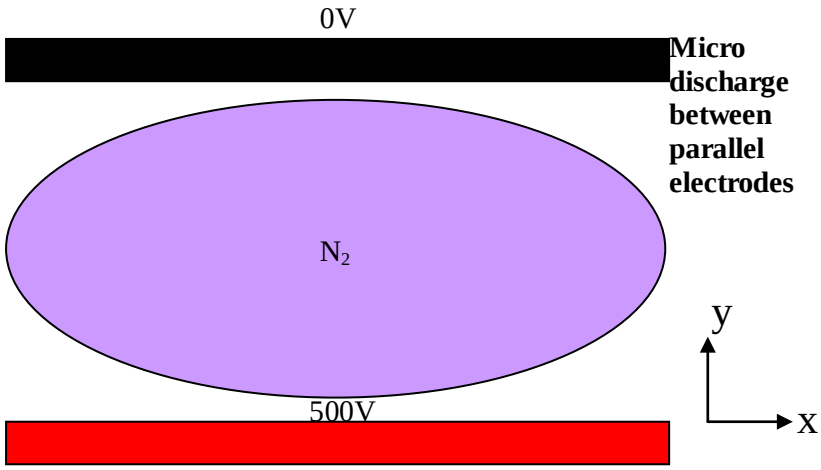

Figure 3-2. Schematic of two-dimensional microscale volume discharge with nitrogen gas.

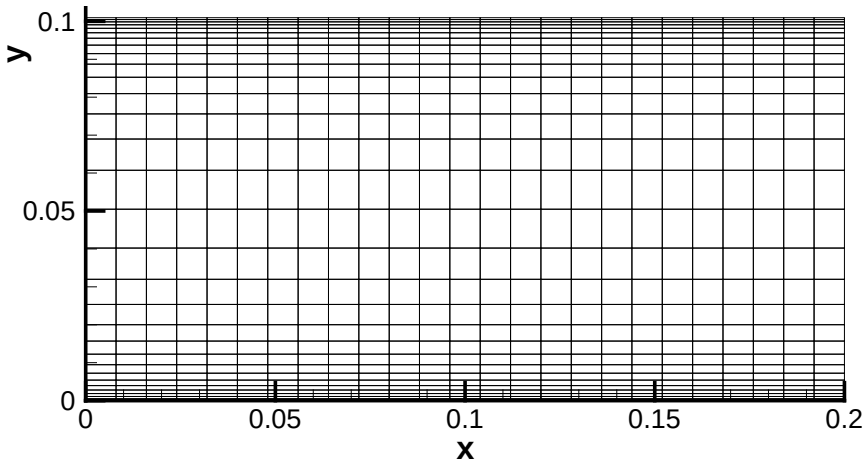

Figure 3-3. Schematic of computational domain with 3111 nodes and 750 elements.

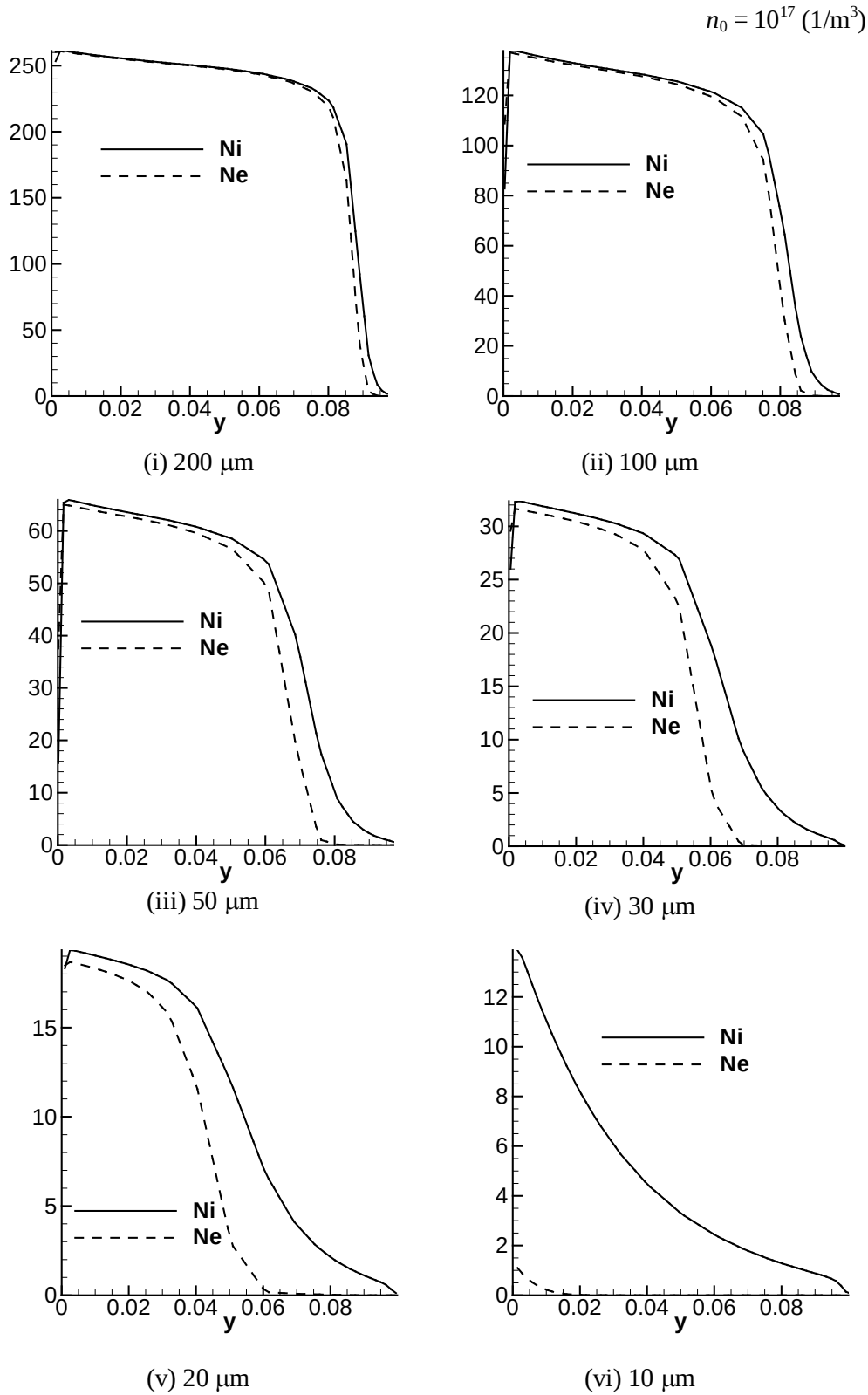

Figure 3-4. Ion (N_i) and electron (N_e) density distribution along y-direction with various gaps from d_g = 200 to 10 μm. Reference density $n_0 = 10^{17}$ m^{-3}.

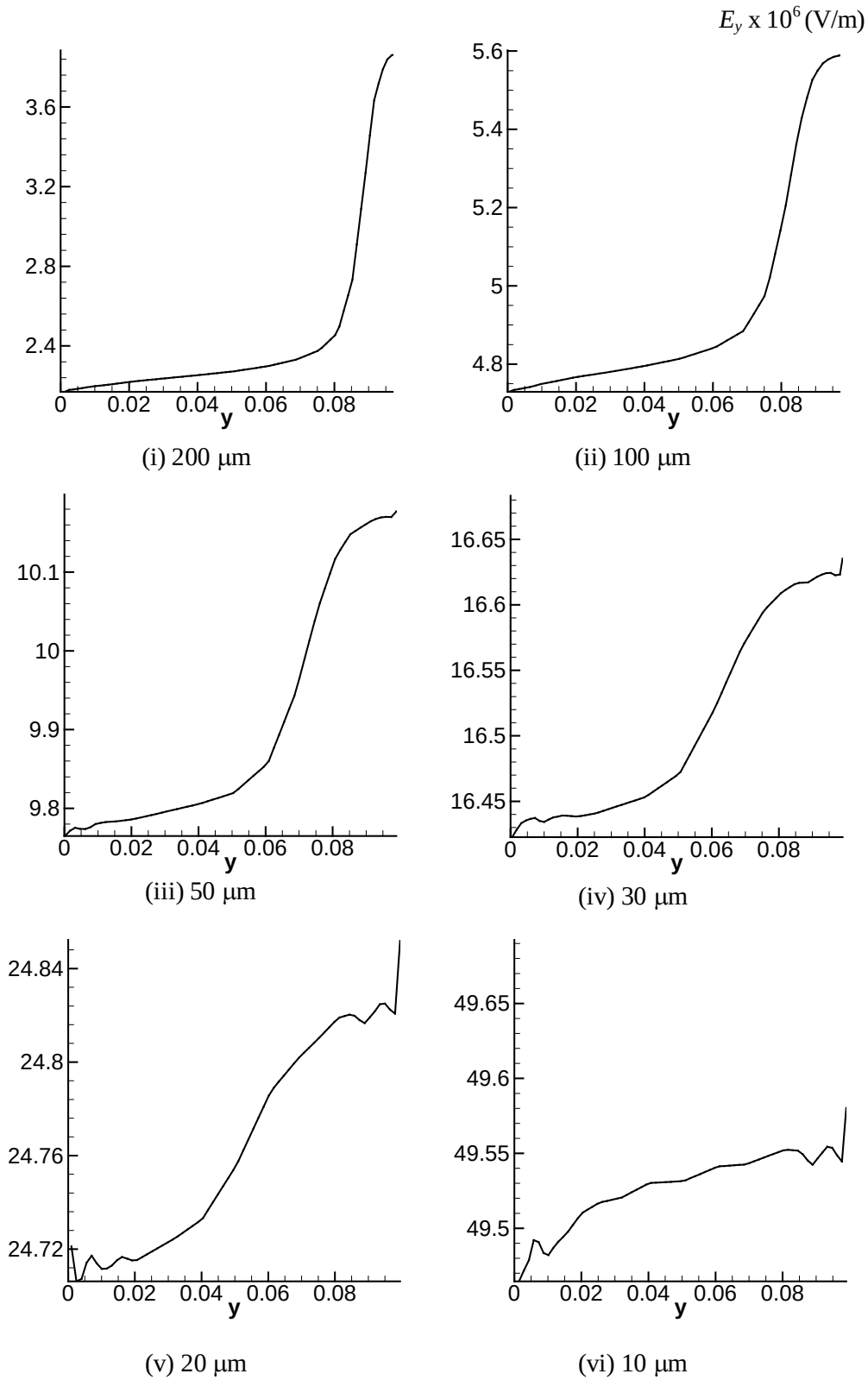

Figure 3-5. Electric field E_y (V/m) along y-direction with various gap from d_g = 200 to 10 μm.

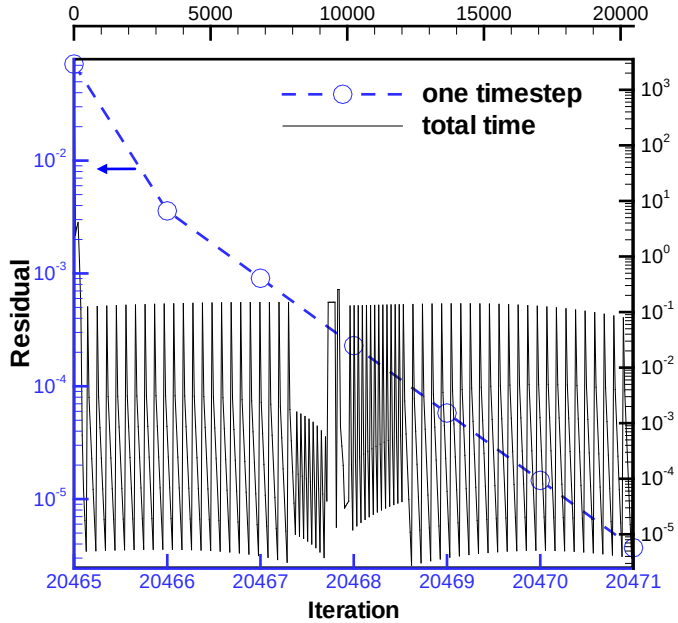

Figure 3-6. Convergence for one time step from iteration 20465 to 20471 and total time from iteration 0 to 20471.

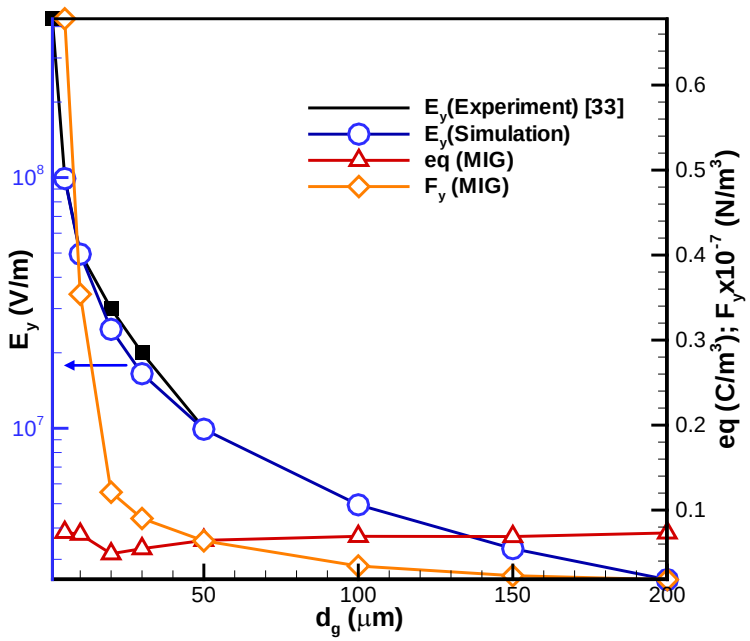

Figure 3-7. Comparison of numerical results and experimental data for electric field strength from d_g = 50 to 5 μm. The charge density (eq) and the electric force (F_y) are calculated from numerical results.

In conclusion, we study plasma discharge in microscale in order to enhance the electric force for realistic applications. A two-dimensional nitrogen volume discharge under applied DC potential has been modeled. It is based on first-principles using a self-consistent coupled system of hydrodynamic equations and Poisson equation. The quasi-neutral plasma ($N_i \approx N_e$) the sheath ($N_i >> N_e$) regions can be observed shown in Fig. 3-4. Interesting, the layer of sheath is governed by the Debye length. When the gap between electrodes is close to Debye length, the electron density is very less compared with ion density. That is why the electric field arises sharply close to the layer of sheath shown in Fig. 3-5. The computational error is also investigated to guarantee the calculation of physics of plasma actuators. The convergence criterion is less than 10^{-5} for every time step. The results of electric field match well with published experimental data [33] from 50 to 5 μm for interelectrode gaps. Based on the electric force calculation, the force is almost 7 times increase from 20 to 5 μm. Such electric force in microscale may be useful for Microelectromechanical systems (MEMS) technology.

CHAPTER 4
APPLICATIONS OF MICROSCALE SURFACE DISCHARGE

We presented a study of microscale volume discharge with nitrogen as a working gas in chapter 3. The microscale discharge is investigated using a first-principles approach solving coupled system of hydrodynamic plasma equations and Poisson equation for ion density, electron density, and electric field distribution. We found microscale plasma actuators that may induce orders of magnitude higher force density (N/cm^3). Such EHD force may be beneficial to some realistic applications, i.e. micropump in microfluidic systems.

In this chapter, we simulate a first generation micro plasma pump. We solve multiscale plasma-gas interaction for two-dimensional cross-section of micro plasma pump. The result shows that a reasonable flow rate (ml/min) can be pumped using a set of small active electrodes. Furthermore, we introduce a flow shaping mechanism using surface compliant microscale gas discharge. Such horseshoe actuator may improve the performance of micro plasma pump. Three-dimensional details of charge separation, potential distribution, and fluid velocity are solved. Finally, a three-dimensional micro plasma pump incorporated horseshoe actuator is simulated. The results of plasma simulation identify three-dimensional nature of electric force. The flow rate of micro plasma pump is on the order of ml/min. Such flow rate may be beneficial for many applications from biological analysis to micropropulsion in space.

4.1 2D Micro Plasma Pump

Micropump is one of the most important components in the microfludics. Our interest is to investigate EHD micropump due to the advantage of rapid on/off switching without any moving parts. Also, it can push the flow continuously without intermittent pulsed. The concept of new generation of micro plasma pump has been developed by Roy [62]. Such design leverage several

advantages of non-mechanical micropumps shown in Fig. 4-1 [82]. Fig. 4-1 shows the micro plasma pump with four pairs of DBD actuators at both inlets and two pairs of DBD actuators at the center of the pump. The pump inlet openings are 250 μm at both sides and the single outlet opening is 500 μm at the top. Fig. 4-2(A) shows the configuration of DBD actuator. The powered electrode is 20 μm wide, while the grounded electrode is 40 μm wide. The gap between electrodes is 10 μm at streamwise direction and 50 μm in vertical direction. Fig. 4-2(B) shows two-dimensional computational mesh for simulation of micro plasma pump with a Kapton polyimide insulator, i.e. dielectric constant $\varepsilon_d = 4.5\varepsilon_0$, where ε_0 is permittivity of vacuum. We simulate half of micro plasma pump due to the symmetric configuration. The computational mesh consists of 67x50 elements and 13635 nodes. The boundary condition of potential ϕ is equal to 1300 V. We neglect the thickness of powered electrode (at y = 50 and 300 μm) and grounded electrode (at y = 0 and 350 μm). For the flow simulation, gauge pressure is equal to zero at the inlet and the outlet. The right boundary is maintained as symmetry, and based on low Knudsen number (Kn) of $2.6\text{x}10^{-4}$ all the dielectric surfaces are maintained at zero wall velocity.

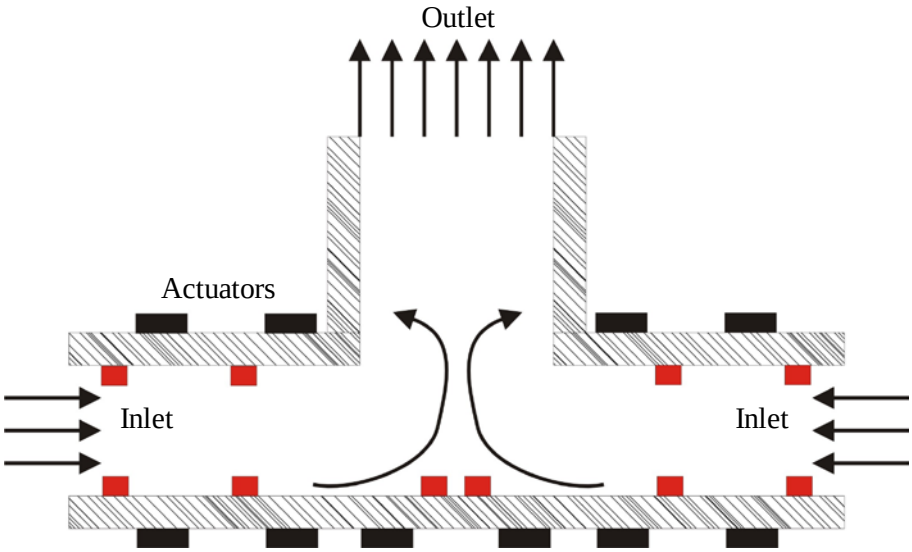

Figure 4-1. Schematic of two-dimensional micro plasma pump.

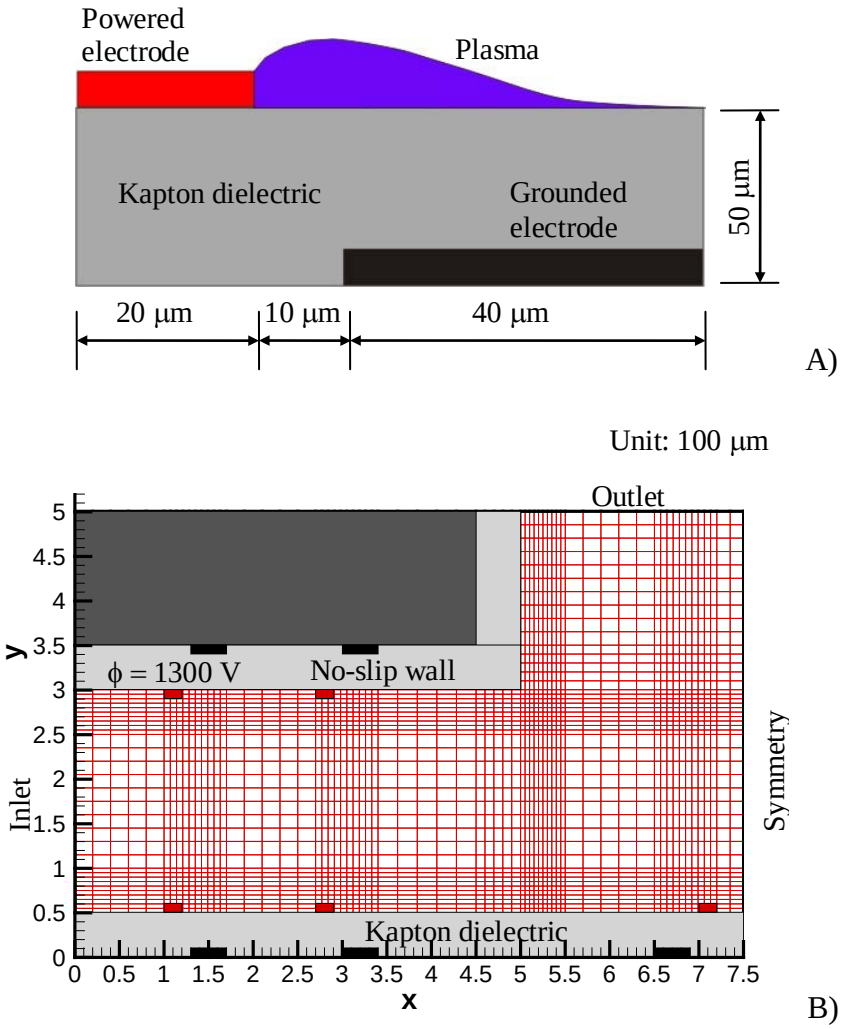

Figure 4-2. Computational domain of 2D micro plasma pump with 13635 nodes and 3350 elements. A) Microscale DBD actuator. B) Computational mesh.

Fig. 4-3(A)-(C) plot the contour of potential (ϕ), ion number density (N_i), and electron number density (N_e). Fig. 4-3(A) shows an applied potential of 1300 volts on the powered electrode (red). The electric field lines are acting from the powered electrode to the grounded electrode. Due to a large difference of potential between electrodes, the fluid is ionized at local regions shown in Fig. 4-3(B) and (C). We can see the net charge densities are concentrated inside the boundary layer near the wall, and it is almost zero away from the wall. Note that the

charge densities depositing on the dielectric surface will cause a net electric force in the direction from the powered electrode to the grounded electrode. Therefore, outside the plasma region, the flow is mainly driven by viscous force.

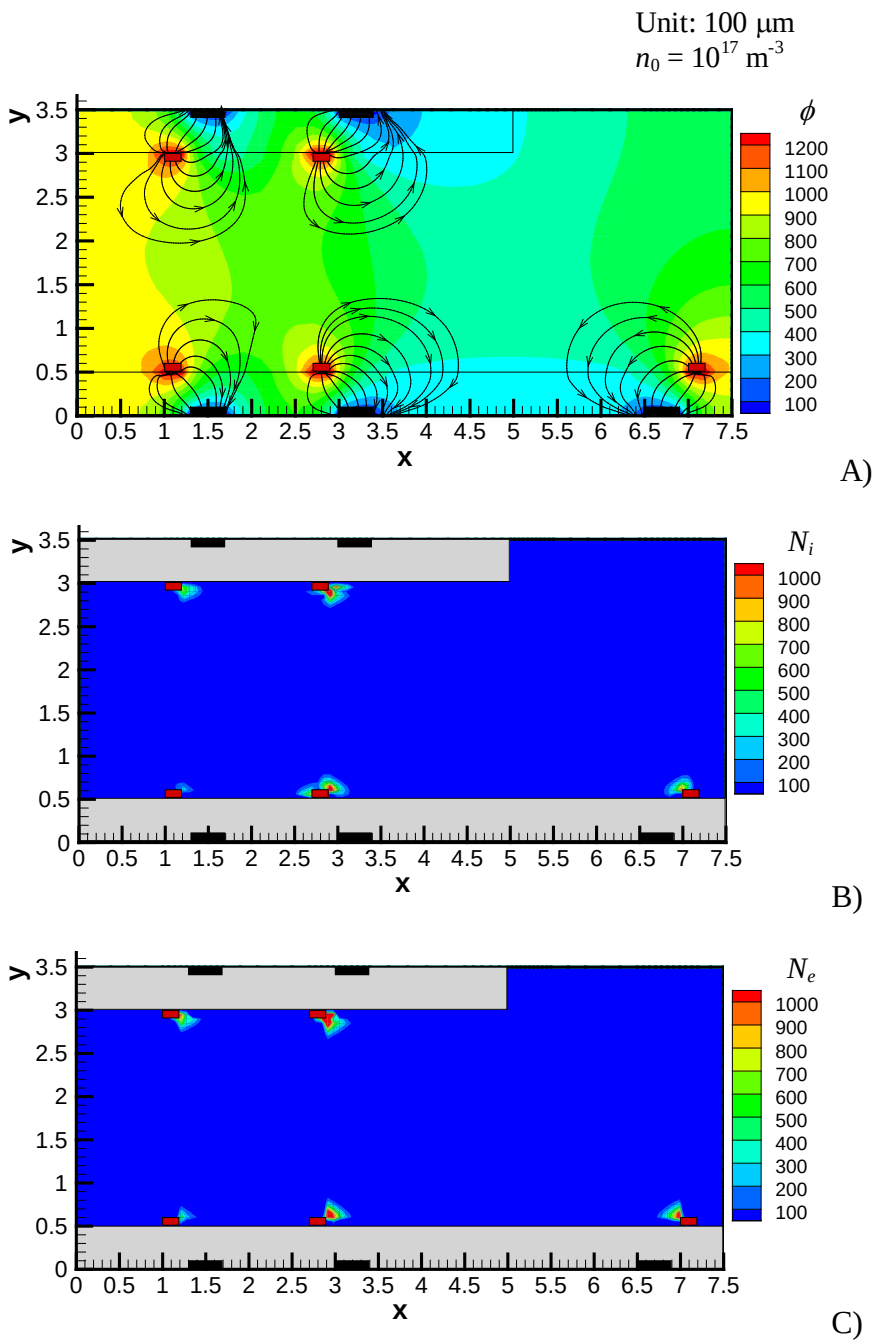

Figure 4-3. Results of 2D micro plasma pump for detailed plasma simulation. A) Potential (ϕ) distribution with electric potential lines. B) Ion number density (N_i) contour. C) Electron number density (N_e) contour.

Fig. 4-4 shows the flow behavior inside the micro plasma pump. We can see the plasma drives the fluid into the pump at the inlet (x = 0) due to the net near-wall jet created by DBD actuators. We also can see one of the DBD actuators near symmetry boundary (x = 0.0007 m) with different configuration. This actuator is used for altering the fluid flow direction from horizontal to vertical direction and pushes the fluid upward to the outlet. However, it also creates a strong vortical structure inside the pump. That will influence the mass flow rate of micro plasma pump due to the energy loss. Fig. 4-5 shows the V_y-velocity distribution along x-direction normal to the outlet. The V_y-velocity increases sharply from the wall (x = 0.0005 m) and becomes flat V_{max} = 3.1 m/s at middle of the pump (x = 0.00075 m). The sharp increase is because the shear stress that flow exerts on the wall of the pump. After simple calculation, we find the average flow rate Q_{ave}= 28.5 ml/min, which is a function of operating voltage of 1300 V for micro plasma pump with nitrogen as working gas under atmospheric pressure. Such flow rate may be useful for the application of biological sterilization and decontamination, micro propulsions, and cooling of microelectronic devices.

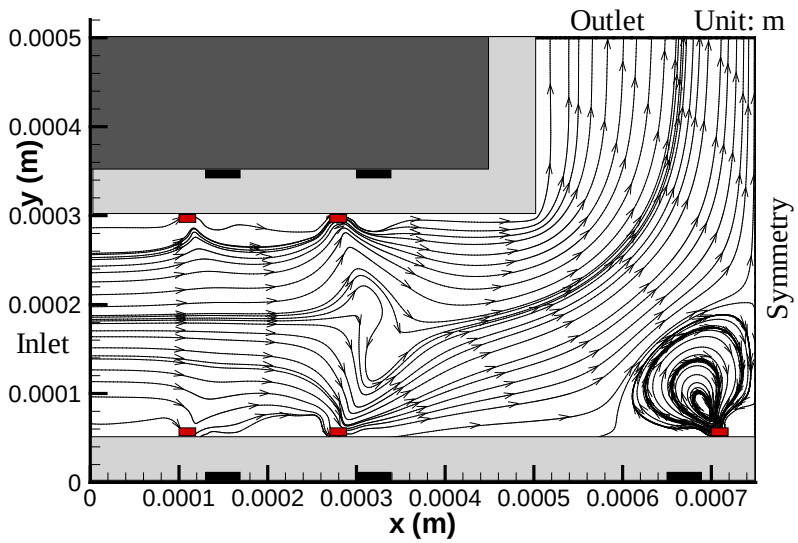

Figure 4-4. The velocity streamtraces inside the two dimensional micro plasma pump.

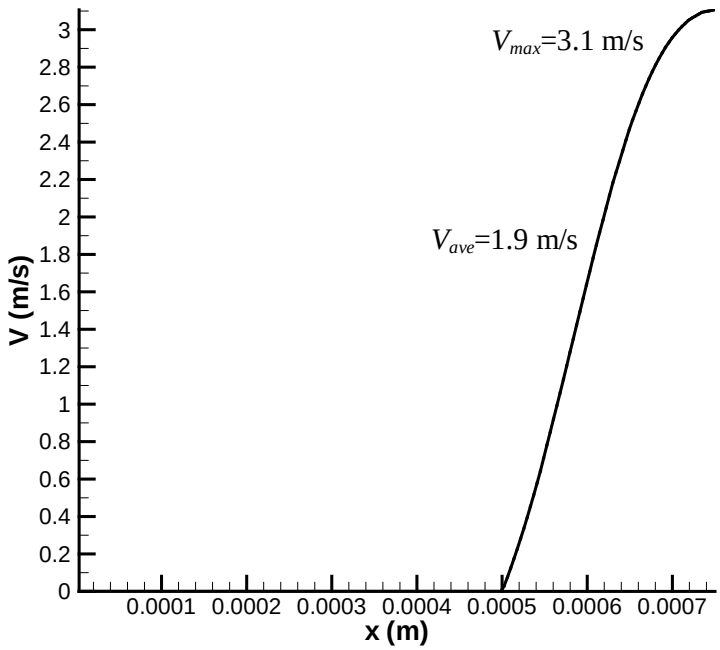

Figure 4-5. V_y-velocity distribution along the x-direction normal to the outlet.

In conclusion, we investigate a two-dimensional micro plasma pump using the same microscale two-species hydrodynamic plasma model. The detailed plasma information inside the pump is shown in Fig. 4-3. The plasma discharge imparts momentum near the wall to push the fluid flow shown in Fig. 4-4. We find the reasonable flow rate which is around 28.5 ml/min for two-dimensional micro plasma pump. Such EHD micropump may become useful in a wide range of applications from microbiology to space exploration and cooling of microelectronic devices.

4.2 3D Micro Horseshoe Plasma Actuator

We showed that the bulk flow can be modified through actively diverting the direction of injected momentum using macroscale horseshoe plasma actuator in our recent study [22]. Appropriate polarization of such plasma generators (in Fig. 4-6) can not only induce flow attachment to work surface but also can change flow direction from the surface-parallel to the surface-normal direction and thus may help flow turbulization.

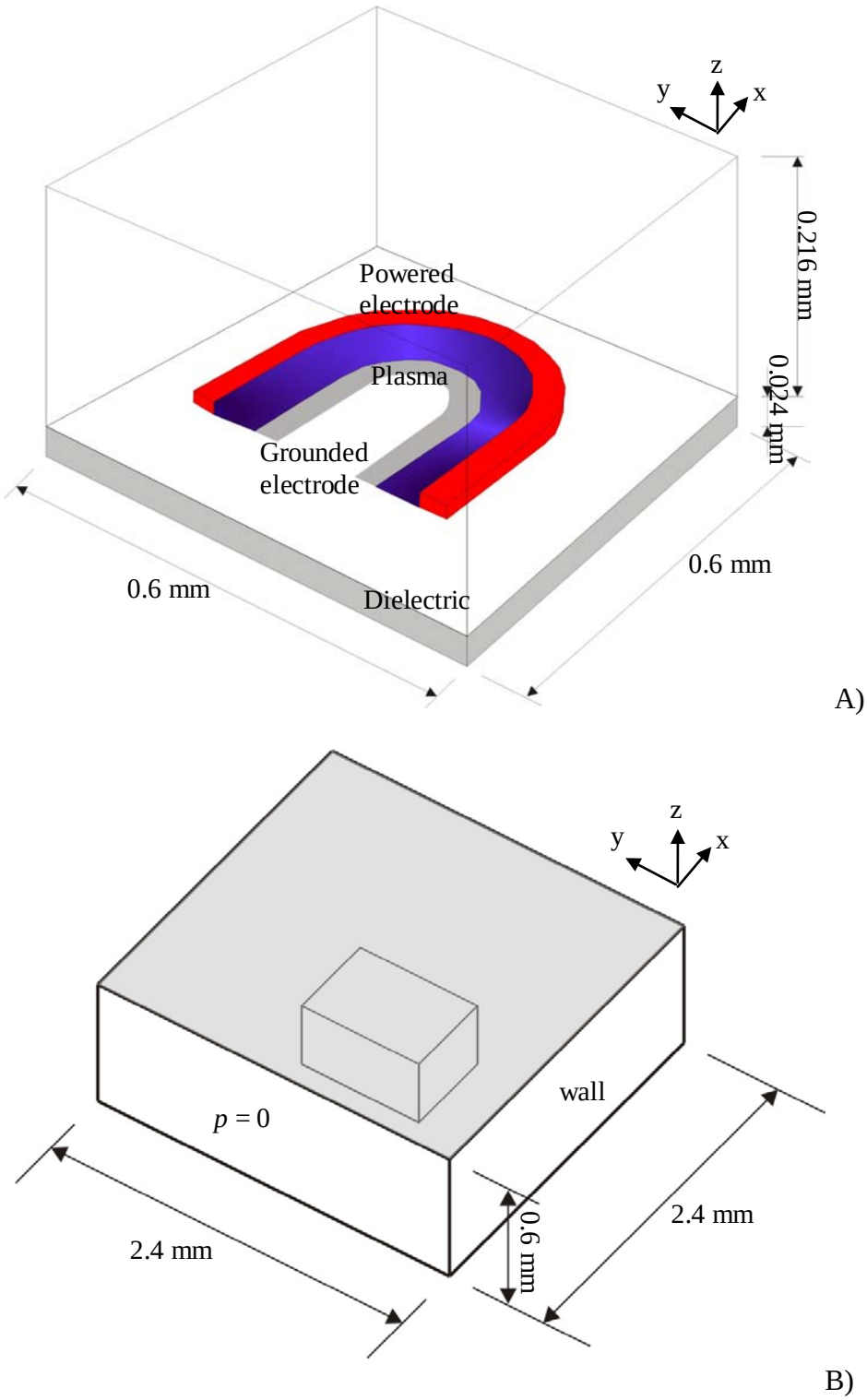

Figure 4-6. Computational domain of horseshoe actuator with quiescent flow for A) plasma domain of 0.6×0.6×0.24 mm and B) fluid flow domain of 2.4×2.4×0.6 mm showing plasma domain inlay.

A top view of both inner (grounded) and outer (powered) electrodes are shaped like horseshoes. When the outer electrode is powered and the inner electrode is grounded, the discharge is primarily inward. The electric force from all three planar directions push fluid toward the central region, where following continuity and momentum conservation the incoming flow changes direction normal to the plane of the actuator. The electric force field in such an actuator is purely three-dimensional because of the geometry pinching the fluid at the center.

We introduce a flow shaping mechanism using surface compliant microscale gas discharge. Three-dimensional details of charge separation, potential distribution, and fluid velocity are solved by multiscale ionized gas (MIG) flow code based on finite element method. The working gas is nitrogen at bulk pressure p = 5 Torr. The ion mobility and diffusion at 300 K as well as electron mobility and diffusion at 11600 K are given by Surzhikov and Shang [65]. We choose the reference time $t_0 = 10^{-8}$ s and the reference density $n_0 = 10^{15}$ m^{-3} for the plasma simulation. Due to several orders of magnitude difference in timescales of plasma and gas flow, we employ the time average of electric body force $F_j = eqE_j$ in the Navier-Stokes equations. For conditions stated in this problem, the Knudsen number (Kn) is less than 0.008 validating the use of no-slip condition.

The computational domain for plasma simulation consists of a lower part of 0.024 mm thick dielectric with zero charge density and an upper part of a fluid domain (0.6×0.6×0.216 mm) filled with nitrogen gas shown in Fig. 4-6(A). The exposed (red) electrode of the horseshoe actuator is at center of the domain on the dielectric surface at z = 0.024 mm while the embedded electrode is grounded at z = 0. A direct current voltage of ϕ = 50 V is applied to the exposed electrode. Note that the electrodes are shown here as references and they have negligible thickness. Fig. 4-6(B) shows the computational domain (2.4×2.4×0.6 mm) for quiescent flow

simulation and inner domain which is at center of the outer domain for plasma simulation. We assume zero pressure for both boundaries in x-direction (x = 0 and 2.4 mm) and all other boundaries with no-slip wall condition. The computational domain was discretized using 48×48×40 three-dimensional tri-linear elements with 98,441 nodes sufficient to capture the sheath (Debye length) physics for plasma simulation. The fluid boundary layer physics is resolved with a mesh of 48×48×20 three-dimensional tri-linear elements overlay on top of the plasma mesh.

Fig. 4-7 shows the electric force vectors distribution overlay on (A) charge separation $q = n_i - n_e$ at x-z plane (y = 1.2 mm) and (B) potential distribution at x-y plane (z = 0.03 mm). We can see the potential ϕ varies from 50 to 0 V calculated from Poisson equation. The force density for this electrode arrangement (not shown) is in the order of kN/m^3. The quasi-steady state solution for the peak of separated charge is close to the dielectric surface inside the exposed electrode of the horseshoe actuator. The peak charge density is about 10^{15} m^{-3}. From top view just above dielectric surface at z = 0.03 mm shown in Fig. 4-7(B), we can easily see the distribution of the electric force vectors acting inward.

Fig. 4-8 describes the effect of horseshoe actuator on quiescent flow in three different planes. The center of the horseshoe is located at (x, y, z: 1.2, 1.2, 0 mm). The electric force attracts fluid toward the center of the horseshoe as shown in Fig. 4-8(A) and pushes fluid to the left boundary (x = 0). The effect of inward acting plasma force extracts fluid from top of plasma region (y = 1.2 mm) and ejects fluid to the both boundaries (y = 0 and 2.4 mm) shown in Fig. 4-8(B). This pinching effect is evident at z = 0.03 mm plane shown in Fig. 4-8(C). The fluid is separated into an upper half portion and a lower half portion. As a result, the working fluid is

ejected nearly outward normal to the plasma region and the fluid is almost stagnant at the center of the horseshoe actuator.

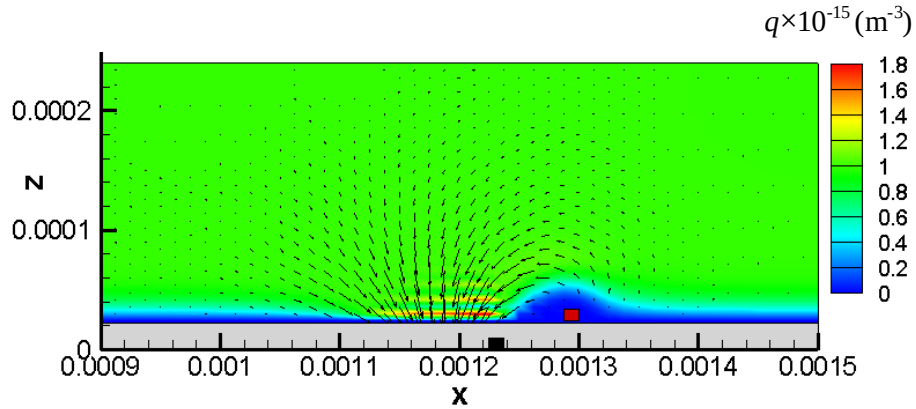

A)

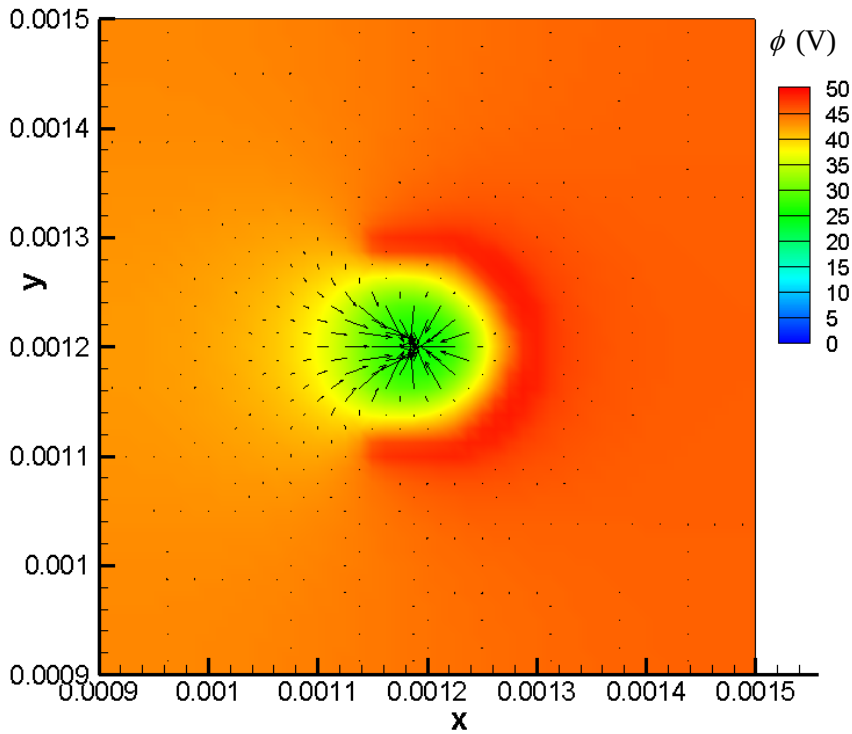

B)

Figure 4-7. Results of detailed horseshoe actuator simulation for A) charge separation contour $q = n_i - n_e$ at x-z plane (y = 1.2 mm) and B) potential ϕ at x-y plane (z = 0.03 mm) with force vectors.

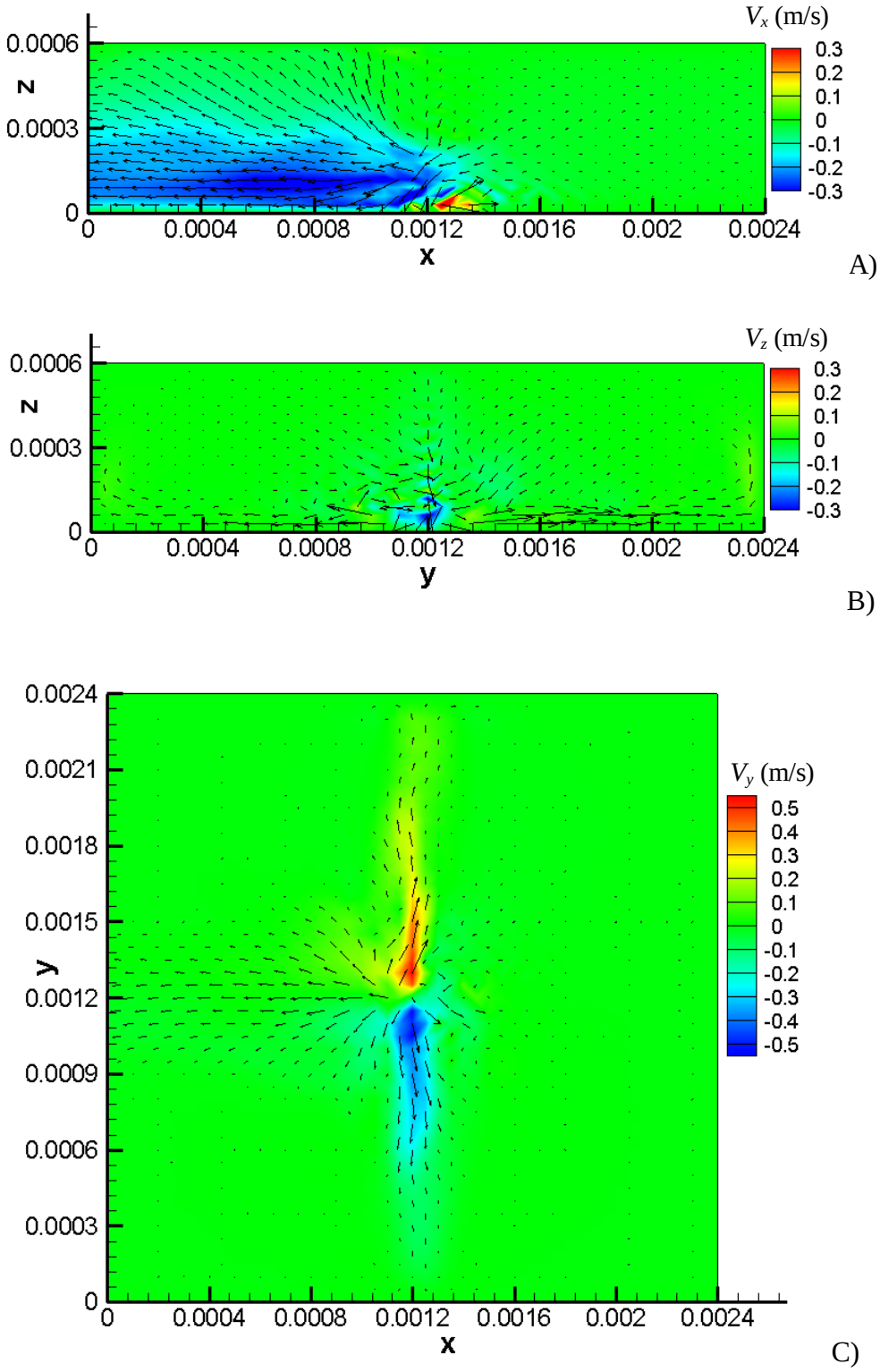

Figure 4-8. Velocity contour of horseshoe actuator for three different directions with force vectors. A) V_x-velocity contour at x-z plane (y = 1.2 mm). B) V_z-velocity contour at y-z plane (x = 1.2 mm). C) V_y-velocity contour at x-y plane (z = 0.03 mm)

Figure 4-9(A) plots the fluid lines with green color for the quiescent flow. The bottom wall is colored by potential (ϕ) for recognizing the location of the electrodes. We can see the electric force attracts the fluid from outside of the horseshoe actuator and trips the fluid lines in the plasma regime. Such a tripping mechanism creates plasma barriers to push the flow toward the central region and ejects the fluid normal to the plane of the actuator shown in Fig 4-9(B). The pressure coefficient shown in Fig 4-9(C) calculated based on the peak induced velocity also shows a sharp rise (stagnant point) followed by a quick drop denoting rapid change in the flow direction.

Corresponding plasma induced velocity components at three separate *x* locations along *z*-direction are plotted in Fig. 4-10. While the force density for such microscale actuator is calculated to be kN/m^3, the control volume in which this electric force is orders of magnitude smaller imparting 0.1 mN/m net force on the surface inducing 0.1 m/s velocity. For such microdischarge, the steady state current density near the cathode is estimated to be ~0.1 A/cm^2 [39]. Horseshoe discharge area is around 2.6×10^{-4} cm^2. So the real power is estimated as ~ 1.3 mW.

In conclusion, a three-dimensional plasma simulation based on first-principles method demonstrates flow shaping using a surface compliant horseshoe plasma generator. When the outer electrode is powered and the inner electrode is grounded, the electric force distribution is acting inward the center of the horseshoe actuator shown in Fig. 4-7. Results demonstrate that the induced electric force pinches the fluid inside the plasma generator to trip the flow field normal to the dielectric surface shown in Fig. 4-8. Such low power generators may be useful for many applications including flow shaping, thrust vectoring, and device cooling.

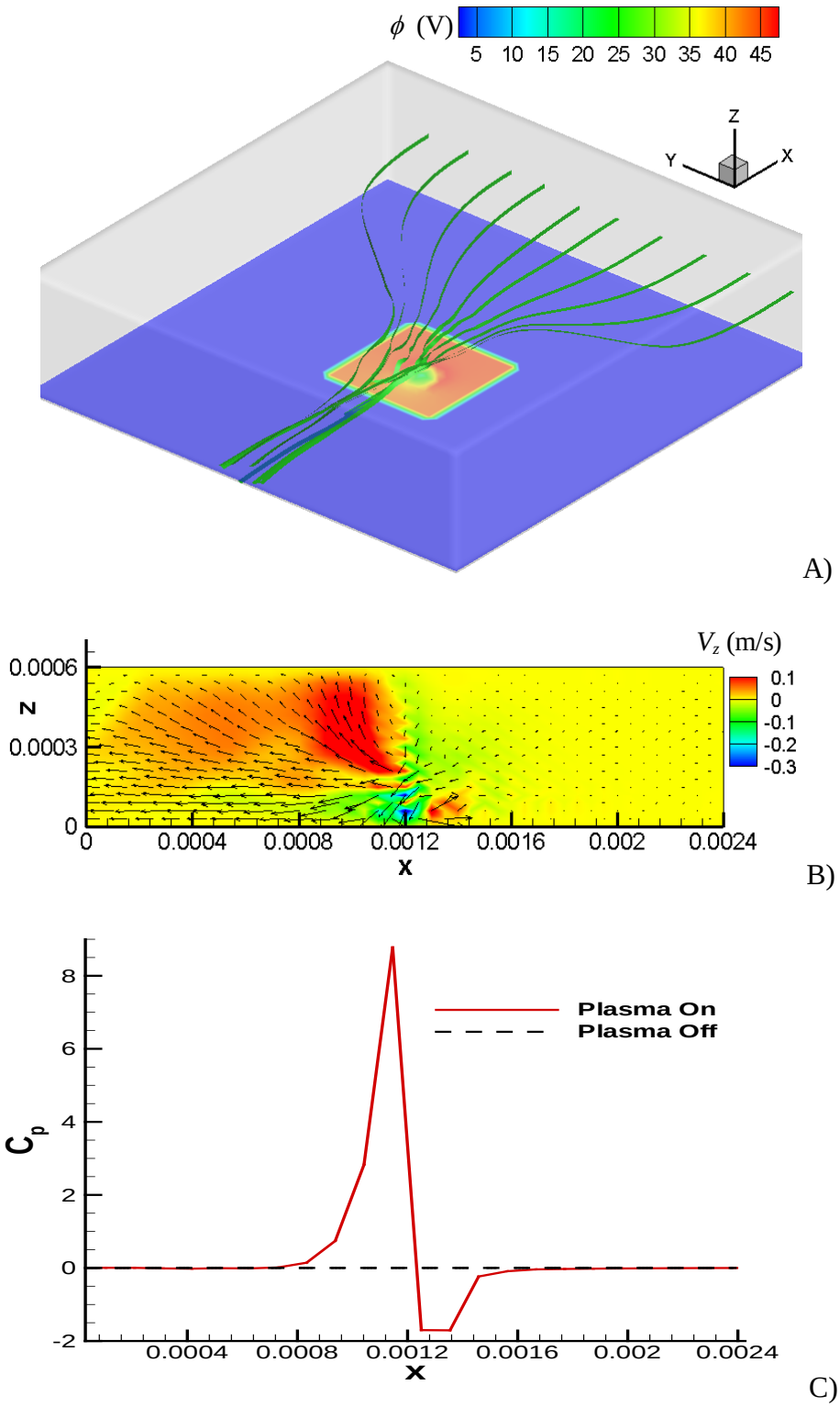

Figure 4-9. Results of detailed fluid flow simulation for velocity and pressure. A) Green fluid lines with potential (ϕ) contour at bottom for quiescent flow. B) V_z-velocity contour at x-z plane (y = 1.2 mm) with force vectors. C) Pressure coefficient along (x, 1.2, 0.03 mm).

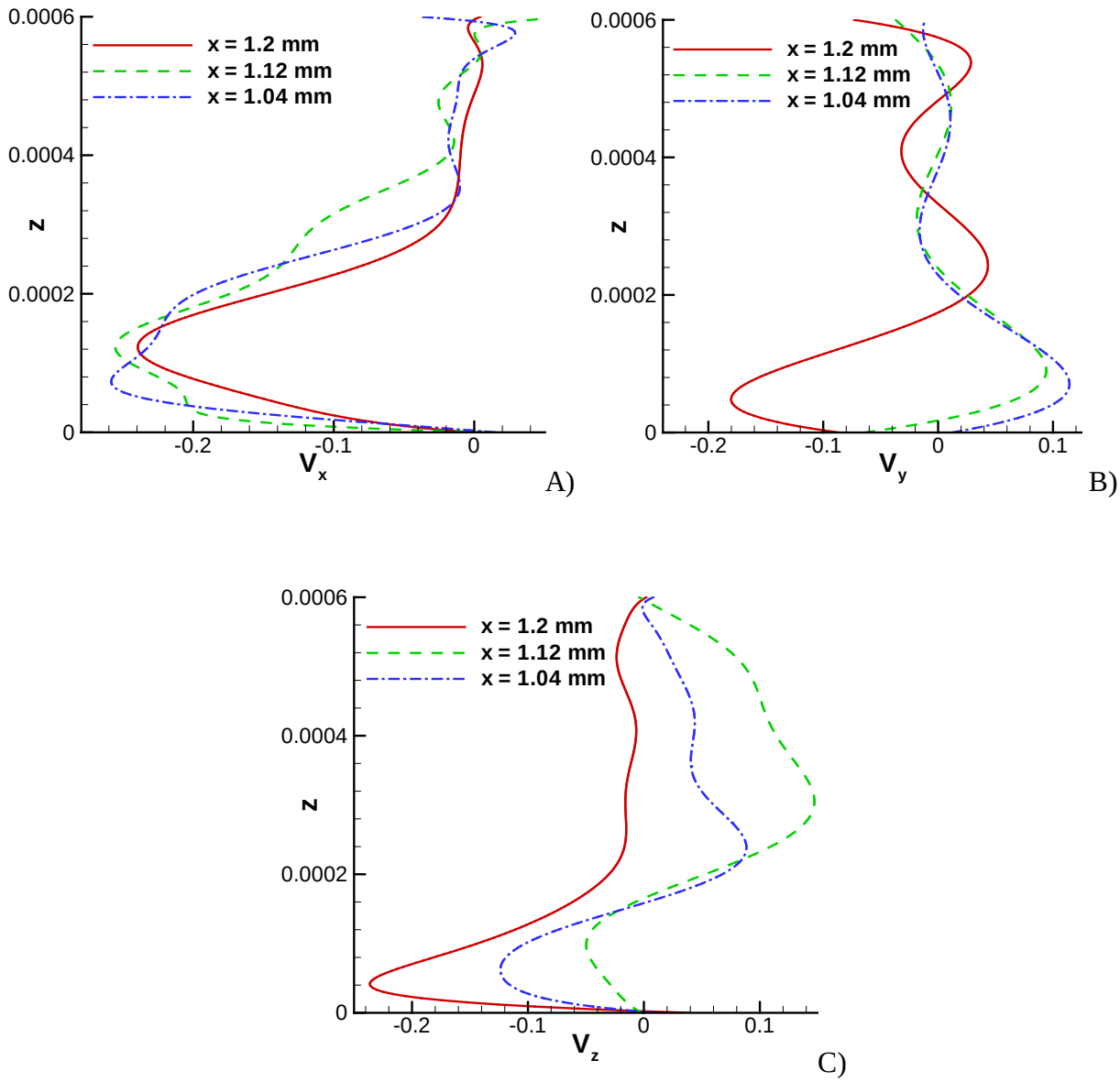

Figure 4-10. Induced velocity components along the *z*-direction at *y* =1.2 mm and three *x* locations for A) V_x-velocity, B) V_y-velocity, and C) V_z-velocity.

4.3 3D Micro Plasma Pump

Our two-dimensional hydrodynamic model of microscale direct current (DC) volume discharge [82] shows the force density is to be three orders of magnitude higher than the macro plasma actuator. However, the net flow inducement remains similar to that of standard actuator

due to orders of magnitude smaller plasma region than the traditional counterparts. A two-dimensional micro plasma pump model was simulated for the plasma-gas interactions predicting a reasonable ~ 28.5 ml/min flow rate of nitrogen gas. However, such two-dimensional models are limited especially for a three-dimensional geometry. In the 3D horseshoe plasma actuator simulation [83], we prove the fluid can be pinched and ejected normal to the plane of the actuator. That may help to increase the flow rate of the micro plasma pump. Thus, for a better design of the micro plasma pump, it is important to identify three-dimensional effects on plasma and gas flow fields.

Fig. 4-11 shows a schematic of micro plasma pump (A) cross-section and (B) isometric view. We can see this tri-directional plasma pump draws the fluid into the micro channel at the both inlets due to the attraction of parallel plasma actuators and drains the fluid upward to the outlet by means of horseshoe plasma actuators. Two cases described in Table 4-1 were simulated. The inlet openings of the pump for both cases are 0.1296 mm^2, while the outlet openings are 0.24 mm^2 for Case#1 and 0.39 mm^2 for Case#2. The volume of micro plasma pump is 2 mm^3. The length and width of the electrodes are 200 μm and 12.5 μm for the parallel actuator. The horseshoe actuator consists of two semi-circle electrodes with inner arc radius of 25 μm and outer arc radius of 100 μm. We neglect the thickness of the electrodes in vertical *z*-direction. The gap between electrodes is 50 μm in streamwise *x*-direction and 24 μm in vertical *z*-direction which is the dielectric thickness. We simulate the symmetric half of these micro plasma pumps in Table 4-1.

Table 4-1. Geometric parameter for Case#1 and Case#2.

Unit: mm	l_1	l_2	l_3	h_1	h_2	w
Case#1	1	0.4	1	0.216	0.144	0.6
Case#2	0.875	0.65	0.875	0.216	0.144	0.6

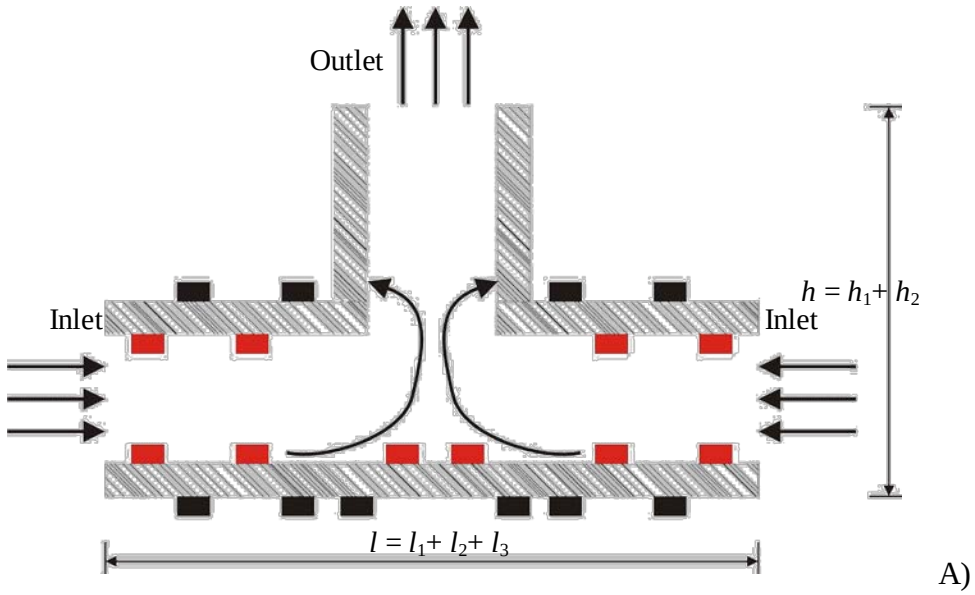

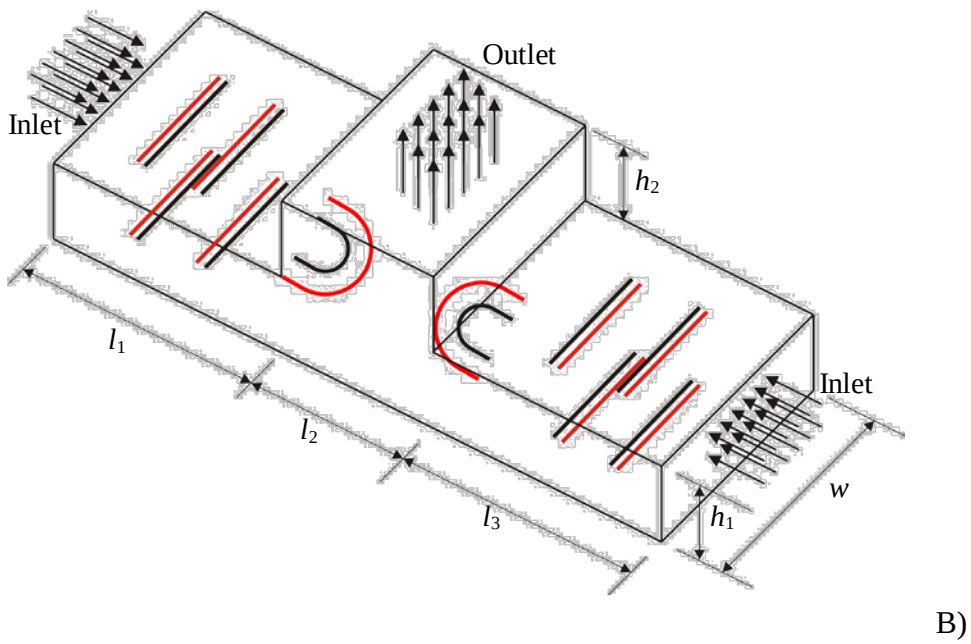

Figure 4-11. Schematic of three-dimensional micro plasma pump A) cross-section and B) isometric view.

Fig. 4-12 shows the computational mesh in two-dimensional cross-section and three-dimensional domain for (A) Case#1 and (B) Case#2. The domain size consists of 96×48×60 tri-linear elements with 289,933 nodes. The mesh density is of the order of Debye length which is sufficient to capture the physics of plasma dynamics. Fig. 4-12(A) shows the locations of all the actuators in a two-dimensional cross-section for Case#1. The powered electrodes (red color) are from x = 0.25 to 0.2625 mm, from x = 0.6 to 0.6125 mm, and from x = 1.375 to 1.5 mm. The dielectric surface is Teflon film between electrodes from z = 0 to 0.024 mm and from z = 0.216 to 0.24 mm. The grounded electrodes (black color) are from x = 0.3125 to 0.325 mm, from x = 0.6625 to 0.675 mm, and from x = 0.975 to 0.9875 mm. The mesh densities of Case#2 and Case#1 are same shown in Fig. 4-12(B), but the location of the actuators and the size of outlet opening are different.

The unsteady transport for ions and electrons is derived from the first-principles in the form of conservation of species continuity. The species momentum flux embedded in them using the drift-diffusion approximation under isothermal condition. Such approximation can predict general characteristics of plasma discharges in the pressure range from 1 to 50 Torr [65]. The working gas is nitrogen at 5 Torr. The discharge is maintained using a Townsend ionization scheme. The reference time t_0 and reference density n_0 are 10^{-8} second and 10^{15} m^{-3}, respectively. For the plasma boundary conditions, DC potential is applied to powered electrode of ϕ = 50 V for Case#1 and ϕ = 80 V for Case#2. For conditions stated in this problem, the mean free path of the nitrogen is 5.2 μm at 5 Torr, and Kn is validating the use of no-slip condition. For the fluid flow boundary conditions, we assume zero pressure (p = 0) at inlet and outlet openings and zero velocity for all three velocity components V_x, V_y, and V_z on the dielectric

surface and pump wall. We assume symmetric boundary condition at x = 1.2 mm which is the center of the micro plasma pump.

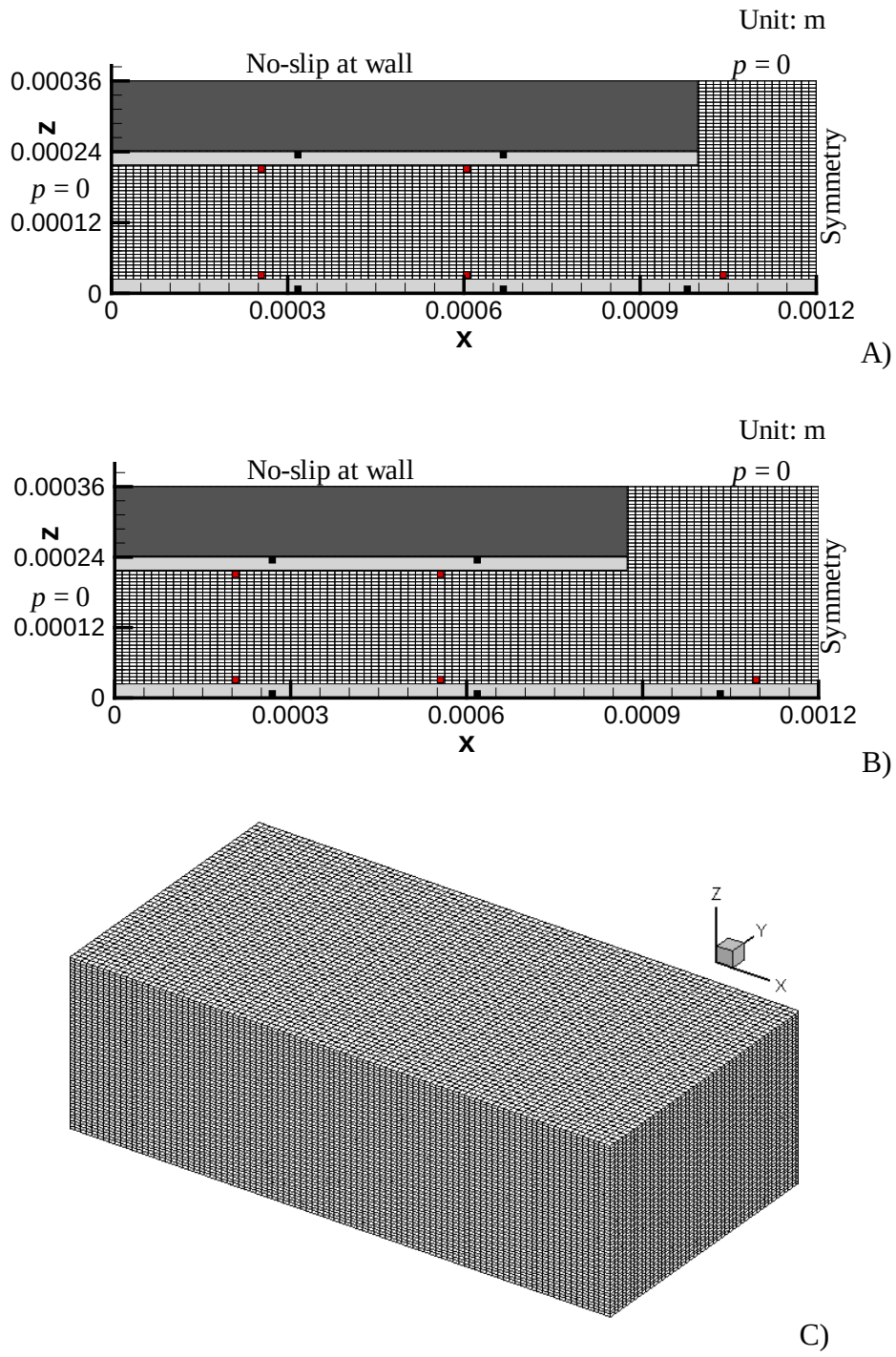

Figure 4-12. Computational mesh density for three-dimensional micro plasma pump. A) Cross-section of Case#1. B) Cross-section of Case#2. C) Computational mesh with 96×48×60 tri-linear elements and 289,933 nodes.

For Case#1 of small opening with 50 V, Fig. 4-13 shows the charge separation at y = 0.3 mm and potential contour plot at z = 0.03 mm with force vectors. The charge separation is given by $q = n_i - n_e$ shown in Fig. 4-13(A). The peak of charge separation is on top of the powered electrode. The strongest force vectors is also close to the powered electrode because the time average of electrostatic force per volume ($F_j = eqE_j$) is function of charge separation and electric field. We also can see that the force vectors are acting from the powered electrode to the grounded electrode which is matching electric field lines. Potential distribution is solved by Poisson equation and matches the boundary condition from 50 V to 0 V shown in Fig. 4-13(B).

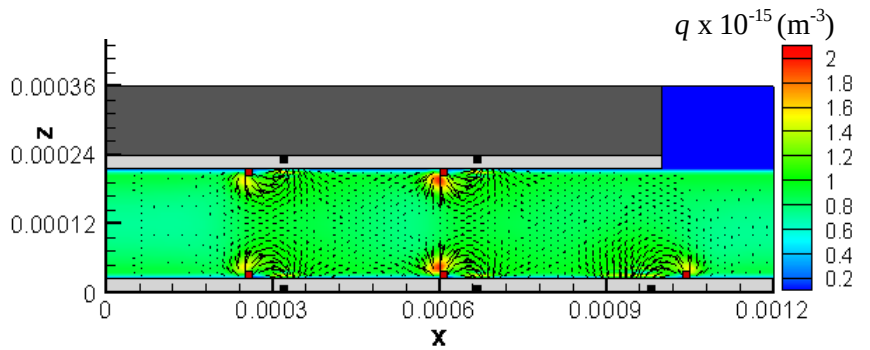

A)

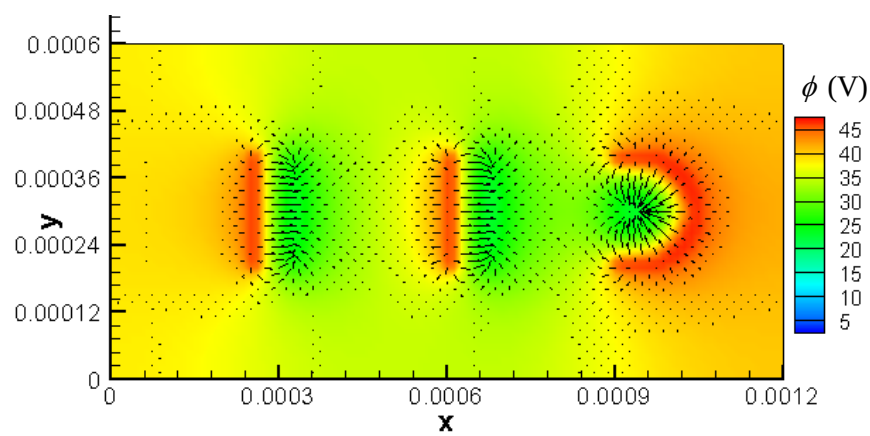

B)

Figure 4-13. Detailed plasma simulation of three-dimensional micro plasma pump for Case#1. A) Charge separation $q = n_i - n_e$ at x-z plane (y = 0.3 mm). B) Potential distribution at x-y plane (z = 0.03 mm) with force vectors.

The reasonable time averaged electric force density is solved by first-principles approach. The electric force density is the source momentum to actuate the fluid flow. Fig. 4-14 (A) shows that the electric force draws the fluid from inlet (x = 0) and drains the fluid upward to the outlet (z = 0.36 mm). The V_z-velocity contour shows the highest upward velocity close to the corner of the micro plasma pump. We can see a vortex at right boundary (x = 1.2 mm) because the horseshoe actuator entrains the fluid from top and pushes it from right to left and creates a plasma barrier. Fig. 4-14(B) shows the streamwise flow hits this plasmas barrier at x = 0.8 mm. Fig. 4-14 (A) depicts two vortical structures near the inlet not found in our reported two-dimensional simulation [82]. This is because we consider the limited length of the actuator along the y-direction instead of infinitely long for two-dimensional simulation.

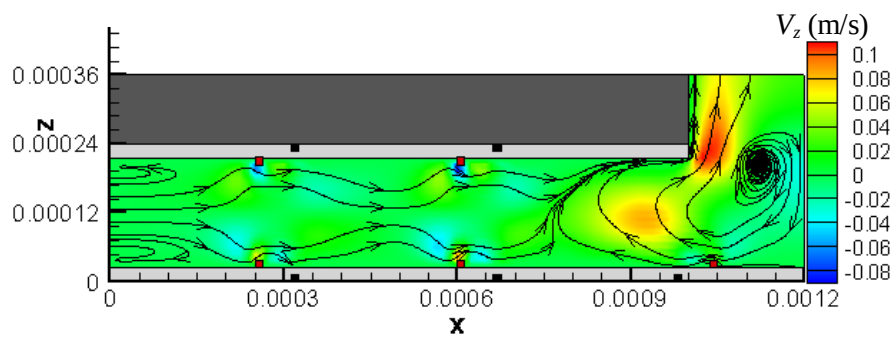

A)

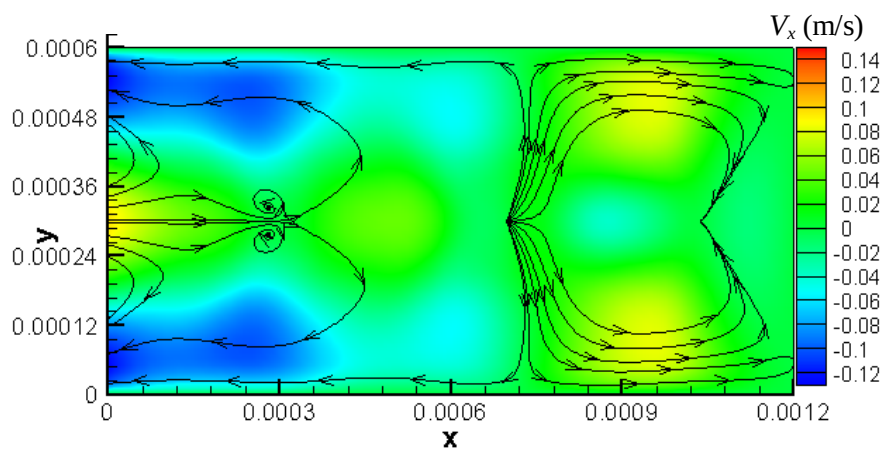

B)

Figure 4-14. Velocity contour with streamtraces at different plane for Case#1. A) V_z-velocity contour at x-z plane (y = 0.3 mm). B) V_x-velocity contour at x-y plane (z = 0.12 mm).

For Case#2 of large outlet opening with 80 V, Fig. 4-15 shows the charge separation and potential distribution with force vectors. We can see the highest value of the charge separation increase due to the potential increase on top of the powered electrode. The force vectors are acting from powered electrode to the grounded electrode due to the distribution of electric field lines and charge separation. Fig. 4-15 (B) shows the top view of the potential distribution at z = 0.03 mm. We can see two standard parallel actuators and one horseshoe actuator with opposite force vectors in x-direction.

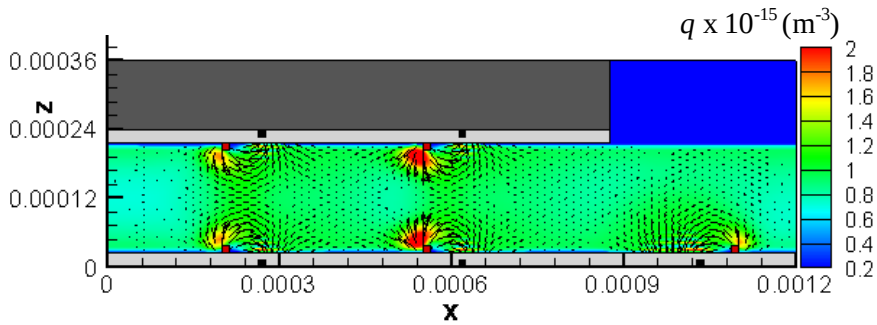

A)

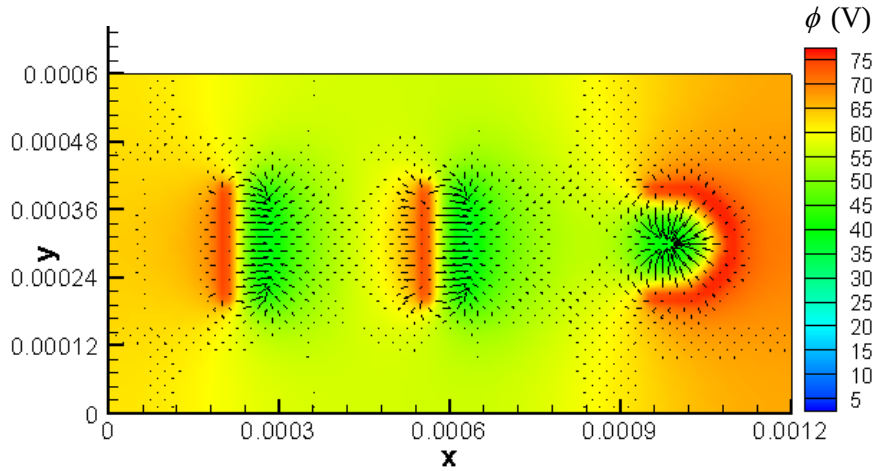

B)

Figure 4-15. Detailed plasma simulation of three-dimensional micro plasma pump for Case#2. A) Charge separation $q = n_i - n_e$ at x-z plane (y = 0.3 mm). B) Potential distribution at x-y plane (z = 0.03 mm) with force vectors.

Fig. 4-16 shows the fluid streamtraces at (A) y = 0.3 mm and (B) z = 0.12 mm. Fig. 4-16 (A) shows that the inlet vortices shown in Fig. 4-14(A) have been reduced due to the higher electric force than Case#1. Also, the location of the actuators may be another factor. However, we can see a bigger vortical structure at the outlet because the horseshoe plasma actuator sucks more fluid from the outlet and pushes it back to the outlet and creates a clockwise vortical structure. Fig. 4-16(B) shows the fluid moves right along the x-direction and hits this clockwise plasma barrier at x = 0.85 mm. So the fluid momentum changes its direction upward. It is obvious that the average flow rate of Case#2 is higher than Case#1 due to the fewer vortices inside the micro plasma pump.

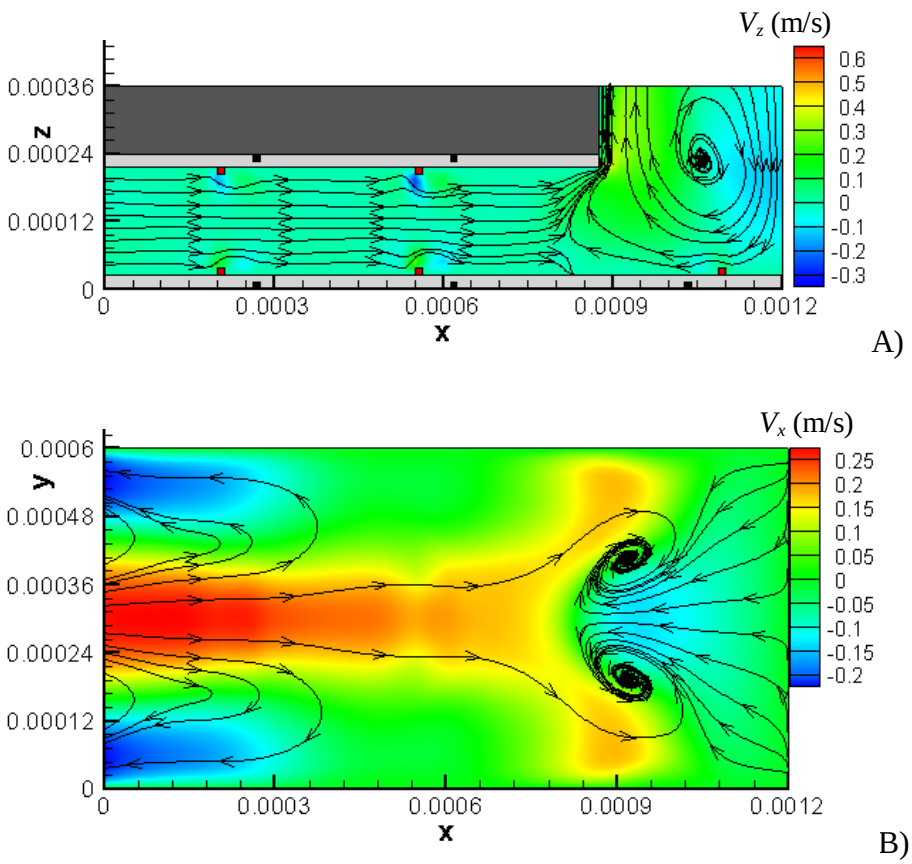

Figure 4-16. Velocity contour with streamtraces at different plane for Case#2. A) V_z-velocity contour at x-z plane (y = 0.3 mm). B) V_x-velocity contour at x-y plane (z = 0.12 mm).

Fig. 4-17 shows the comparison of fluid particles colored by velocity magnitude for (A) Case#1 and (B) Case#2 in isometric view. The top wall is colored by the velocity magnitude, while the bottom wall is colored by the potential. The velocity magnitude of particles for Case#2 (red) is much faster than that in Case#1 (near blue). Also, the streamtraces of fluid flow are smoother than Case#1. The average flow velocity component V_z at the outlet is 4.38 cm/s for Case#1 and is 6.48 cm/s for Case#2. For the calculation of average flow rate Q_{avg}, we find Q_1 = 0.63 ml/min and Q_2 = 1.5 ml/min. Importantly, the predicted average flow rate Q_{avg} for these EHD micropumps is one order of magnitude higher than the design reported in literature.

In conclusion, we have studied two cases of micro plasma pumps using two-species three-dimensional hydrodynamic plasma model coupled with Possion equation. Both plasma governing equations and Navier-Stokes equations are solved using a three-dimensional finite element based multiscale ionized gas (MIG) flow code. The results show the peak charge separation and electric force density on top of the powered electrodes. We find three vortical structures inside the pump which can not be found in our two-dimensional simulation. The locations of the actuators and the applied voltage are key factors to reduce the vortices inside the micro plasma pump. The three-dimensional flow simulation at 5 Torr predicts two orders of magnitude lower flow rate than that predicted earlier [82] for atmospheric condition. The predicted flow rate in Case#2 (Q_2 = 1.5 ml/min) is two times higher than that in Case#1 (Q_1 = 0.63 ml/min). Such flow rates are one order of magnitude higher than that previously reported data for the same level of input voltage and may be quite useful for a range of practical applications.

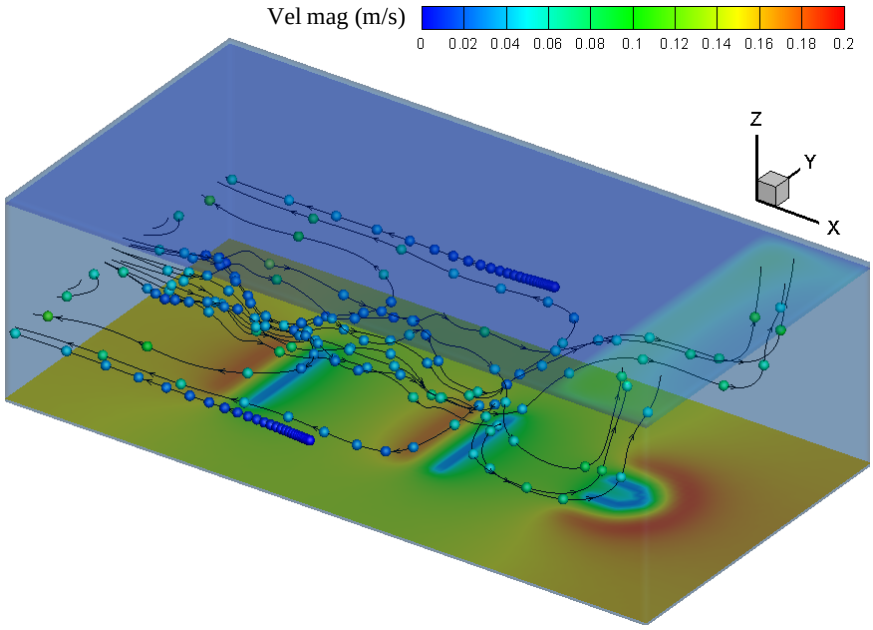

A)

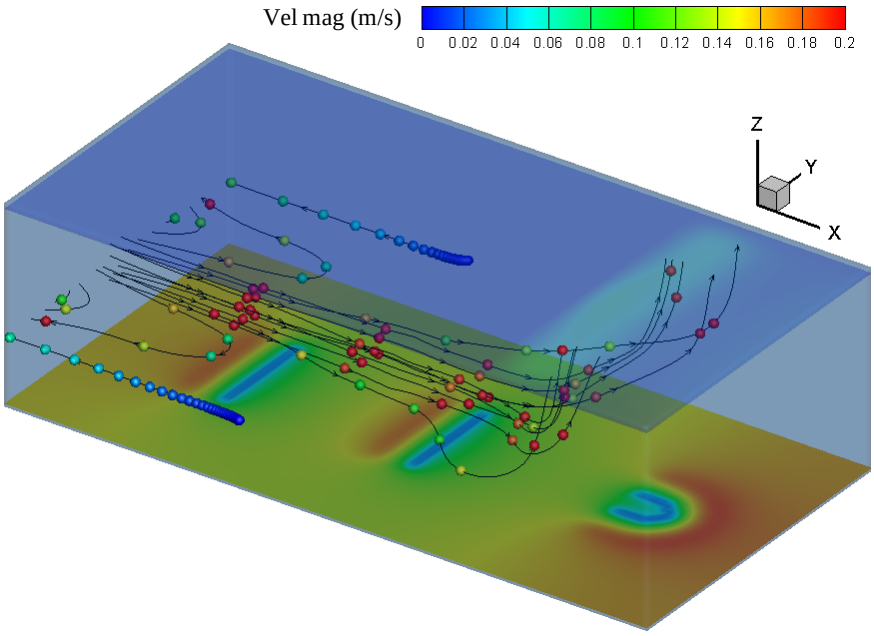

B)

Figure 4-17. Fluid particles distribution inside three-dimensional micro plasma pump for two different cases of A) Case#1 and B) Case#2. The top wall is colored with velocity magnitude and the bottom wall is colored with potential.

CHAPTER 5
SUMMARY AND FUTURE WORK

5.1 Summary and Conclusions

Plasma actuation at atmospheric pressure is getting more attention in aerodynamic applications. To understand the effects of discharge in the fluid region, we develop a local body force model based on a phenomenological modeling approach. We employ this force model for plasma actuated film cooling in gas turbine applications. We identify mechanisms to actuate essentially-stagnant fluid just downstream of the cooling hole by enforcing an active three-dimensional plasma actuation for different cooling hole geometries. Such methods utilize electrodynamic force inducing attachment of the cold jet to the work surface by actively altering the body force in the vicinity of an actuator. Results are compared with published experimental data and other numerical predictions for the latest film cooling technology. An improvement of above 100% over the standard baseline design was shown in Fig. 2-6 [16-17].

To integrate the plasma dynamics and fluid dynamics, a reduced order force model was developed by Singh and Roy [21] based on the first-principles approach. We introduce a modified reduced order force model for bulk flow control with novel designs of horseshoe and serpentine actuators [22]. These actuators are surface compliant and suitable for many flow applications. Such systems utilize forces in the vicinity of electrodes to alter flow structures further away using an electrodynamic mechanism. It is demonstrated that these actuators can not only induce attachment of cold jet to the work surface, but for certain configuration extract momentum from the upstream flow and inject it into the bulk to create turbulization shown in Fig. 2-15 and 2-16.

The primary weakness of DBD actuators is the relatively small actuation effect as characterized by the induced flow velocity. In order to enhance the electric force for realistic

applications, we study plasma discharge in microscale. A two-dimensional nitrogen volume discharge under applied DC potential has been modeled. It is based on first-principles using a self-consistent coupled system of hydrodynamic equations and Poisson equation. The high fidelity finite element procedure anchored in a Multi-scale Ionized Gas (MIG) flow code is employed for solving this problem. The intention of the MIG flow code is expected to ensure minimum error to complement experimental efforts by providing a suitable tool to explore future flow control concepts. Results show two distinct regions observed from Fig. 3-4, the quasi-neutral plasma where $N_i \approx N_e$ and the layer of sheath which is of several Debye lengths attached to the cathode where $N_i >> N_e$. We can see the electron density in the sheath region close to zero. The electric field arising out of this charge separation is plotted in Fig. 3-5. As one approaches the sheath edge, there is an abrupt drop in the charge difference within a small spatial extent. This is the region of pre-sheath where separation in ion and electron density curves begins and where electron density is much less than ion density. By decrease the gap d_g, the sheath becomes more dominant to the plasma region. The results of electric field match well with published experimental data [33] shown in Fig. 3-7. These results are expected to help interpret the plasma formation as the gap decreases to a few micro gaps.

Microscale plasma actuators may induce orders of magnitude higher force density. Such electric force may be beneficial to EHD micropump in microfludics. Based on the novel concept of micro plasma pump [62], we investigate a cross-section of micro plasma pump using the same microscale hydrodynamic plasma model. We find a flow rate is around 28.5 ml/min, which is on the same order of magnitude in literature for EHD micropump. Such micro plasma pumps may become useful in a wide range of applications from microbiology to space exploration and cooling of microelectronic devices [46-48].

Our study [22] showed that the horseshoe plasma actuator can modify the bulk flow through actively diverting the direction of injected momentum. Such actuator creates a purely three-dimensional electric force field because of the geometry. When the outer electrode is powered and the inner electrode is grounded, the electric force distribution is calculated based on the charge separation and the potential gradient. The plasma simulation based on first-principles method demonstrates flow shaping using a surface compliant horseshoe plasma generator. Results demonstrate that the induced electric force pinches the fluid inside the horseshoe actuator to trip the flow field normal to the dielectric surface. Such low power (mW) generators may be useful for many applications including flow shaping, thrust vectoring, and device cooling.

Two-dimensional micro plasma model is limited especially for a three-dimensional geometry. In the 3D horseshoe plasma actuator simulation [83], we prove the fluid can be pinched and ejected normal to the plane of the actuator. That may help to increase the flow rate of the micro plasma pump. Thus, for a better design of the micro plasma pump, it is important to identify three-dimensional effects on plasma and gas flow fields. We have studied two different cases of outlet openings and applied potential for micro plasma pumps. The results of Case#1 are shown in Fig. 4-13 and Fig. 4-14, while the results of Case#2 are shown in Fig. 4-15 and Fig. 4-16. Both plasma governing equations and Navier-Stokes equations are solved using a three-dimensional finite element based MIG flow code described in chapter 2. The ions and electrons are formed through impact ionization process. The recombination is also considered for the time averaged ion and electron densities. Due to the large time scale difference between plasma and fluid flow, we assume flow dynamics does not affect plasma dynamics and only consider plasma actuation of the fluid flow. The results show the highest charge separation and force close to the powered electrodes. Also, we find three vortical structures inside the pump which can not be

found in our two-dimensional simulation [82]. To reduce the vortices inside the micro plasma pump, the location of the actuators and the input voltage may be key factors. The three-dimensional flow simulation at 5 Torr predicts two orders of magnitude lower flow rate than that predicted earlier [82] for atmospheric condition. The predicted flow rate in Case#2 (Q_2 = 1.5 ml/min) is two times higher than that in Case#1 (Q_1 = 0.63 ml/min). Such flow rates are one order of magnitude higher than that previously reported data for the same level of input voltage and may be quite useful for a range of practical applications.

5.2 Contributions

Over the last few years, numerical simulations of microscale plasma actuators are very less in literature, especially for the actively flow control. This dissertation not only contributes to the physics of plasma actuator in both macro and microscale, but also gives an efficient way solving stiffness matrix for three-dimensional finite element problem from weeks to days. The benefits are as follows.

- Fundamental understanding of physics of macroscale and microscale plasma actuators (Chapter 1).
- Development a three-dimensional two species hydrodynamic plasma model in microscale (Chapter 2).
- Development an efficient GMRES solver to form a global matrix for saving computational time from weeks to days (Chapter 2).
- Improvement of the film cooling effectiveness using plasma actuators based on the phenomenological model (Chapter 2).
- Actively flow control for flow attachment and flow turbulization using horseshoe and serpentine plasma actuators based on the reduced order model (Chapter 2).
- Two-dimensional numerical simulation of microscale volume DC discharge for nitrogen gas under atmospheric pressure based on the first-principles method (Chapter 3).

- Two-dimensional multiscale computation of plasma-gas interaction for micro plasma pump based on the first-principles method (Chapter 4).
- Three-dimensional investigation of microscale horseshoe plasma actuator for actively flow control based on the first-principles method (Chapter 4).
- Three-dimensional simulation for physics of micro plasma pump based on the first-principles method (Chapter 4).
- Improvement of the first generation micro plasma pump on the order of ml/min for possible applications from biological analysis to micropropulsion in space.

5.3 Future Work

In the future, the three-dimensional numerical results may be beneficial for realistic applications. But exhaustive three-dimensional simulations based on the first-principles method are in rudimentary stages. There are still rooms for further improvement as follows.

- The two species three-dimensional microscale plasma model can be improved by adding air chemistry for the realistic flow condition.
- Parallel computation could considerably share work loading on different nodes to conduct a huge simulation, such as three-dimensional effective flow control with air chemistry.
- Fabrication and measurement of the flow rate for micro plasma pumps can be an important topic to validate the accuracy of numerical results.
- The estimation of power consumption is useful to improve the performance of the micro plasma pump.
- Realistic PIV experimentation is underway to validate the flow behaviors for these designs.

APPENDIX A
MIG INPUT FILE

The MIG code uses a finite element input format for: *HEADING (dimensions), *NODE (coordinates of each node), *ELEMENT (element-nodes connectivity data), *SOLVE (different solvers), *PRINT (convergence criteria), *TRANSIENT (time stepping), *MATERIAL (ten different material properties), *BOUNDARY (Dirichlet boundary conditions), *FLUX (Neumann or Robin boundary conditions), and *INITIAL (initial conditions). The following example is a two-dimensional microscale volume discharge problem with 3111 nodes and 750 elements in chapter 3.

```
*HEADING,DIMENSIONS=2,NONLINEAR
2d - microscale discharge
2
*NODE
1        0        0.000000000
2        0.004    0.000000000
......
3110     0.196    0.100953893
3111     0.2      0.100953893
*ELEMENT,TYPE=RFNXIANG,MATLABEL=1,RF=0
  1  1  3  105  103  2  54  104  52  53
  2  3  5  107  105  4  56  106  54  55
......
  749  3005  3007  3109  3107  3006  3058  3108  3056  3057
  750  3007  3009  3111  3109  3008  3060  3110  3058  3059
*SOLVE    ,SOLVER =2
*PRINT    ,MAXIMUM_ITER = 5,TOL_RES = 1.d-5, TOL_SOLUTION = 1.d-5
*TRANSIENT, FINAL TIME =0.3,DELTA TIME =1.e-4, WILSON= 1.0, FITER = 20000
*MATERIAL,MATLABEL=1
0. 0. 0. 0. 0  0. 0. 0. 0. 0.
*BOUNDARY
**GROUNDED
**Phi
  1   3  500.
  2   3  500.
...
  50  3  500.
  51  3  500.
**Ne
  3061   2   0.
```

```
  3062   2   0.
...
  3110   2   0.
  3111   2   0.
**POWERED
** Phi
  3061  3  0.0
  3062  3  0.0
...
  3110  3  0.0
  3111  3  0.0
**Ni
  1   1  0.0
  2   1  0.0
...
  50  1  0.0
  51  1  0.0
*FLUX
  1   1  0. 0.
  2   1  0. 0.
...
  25  1  0. 0.
*INITIAL
  1   1  0.10000E+01
  2   1  0.10000E+01
...
3110   1  0.57117E-01
3111   1  0.57117E-01
  1   2  0.10000E+01
  2   2  0.10000E+01
...
3110   2  0.0
3111   2  0.0
1         3         5.000000E+02
2         3         5.000000E+02
...
3110    3         0.000000E+00
3111    3         0.000000E+00
*STOP
```

APPENDIX B
MULTI-SCALE APPROACH

The most challenging problems in physics of a plasma actuator involve the plasma-gas interaction. This is due to length and time scales difference between the plasma and the fluid. For example, a one-dimensional helium discharge operating at 10 kHz and 1.5 kVrms [81], the time-scales of the charge process in the plasma are on the order of 10^{-9} second for electron and 10^{-7} second for ion, and the drift velocity is on the order of 10^5 m/s for electron and 10^3 m/s for ion. The plasma formation time is several orders of magnitude smaller than the time for fluid flow, e.g. time scale for neutral fluid is 10^{-3} second for a 10 m/s freestream velocity on a 100 mm characteristic length. The several orders of magnitude differences in time-scales allow us to assume that the plasma is operating in a quasi-steady regime. Our goal is to solve plasma-gas interaction at microscales in space and picoseconds in time. We develop a step by step procedure for dealing with multi-scale problems as follows.

1. First, build a non-uniform computational grid to capture both plasma and flow physics shown in Fig. 3-3.
2. Second, solve quasi-steady plasma equations to get the results for ion density, electron density and electric field distribution.
3. Third, check the sheath for every time step to make sure the results for ion density, electron density and electric field distribution are quasi-steady.
4. Forth, use the electric force ($F_j = eqE_j$) in the Navier-Stokes equations to run a flow simulation.
5. Go back and redo the step one through four to make sure quasi-steady state results.

LIST OF REFERENCES

1. Lieberman, M.A., and A.J. Lichtenberg. *Principles of Plasma Discharges and Materials Processing*. New York: Wiley, 1994.

2. I. Langmuir, "Oscillations in ionized gases," *Proceedings of the National Academy of Sciences* 14, 627-637(1928).

3. Goldston, R.J., and P.H. Rutherford. *Introduction to Plasma Physics*. Bristol and Philadelphia: Taylor & Francis, 1995.

4. Raizer, Y.P. *Gas Discharge Physics*. Berlin: Springer, 1997.

5. N. Kanda, M. Kogoma, H. Jinno, H. Uchiyama and S. Okazaki, "Atmospheric pressure glow plasma and its application to surface treatment and film deposition," Symposium Proceedings, vol. 3, Paper no. 3.2-20, *International Symposium on Plasma Chemistry*, Bochum, Germany, August 4-9 (1991).

6. J.R. Roth, D.M. Sherman and S.P. Wilkinson, "Boundary layer flow control with a one atmosphere uniform glow discharge surface plasma," AIAA-1998-0328, *36th AIAA Aerospace Sciences Meeting and Exhibit*, Reno, NV, January 12-15 (1998).

7. J.R. Roth and X. Dai, "Optimization of the aerodynamic plasma actuator as an electrohydrodynamic (EHD) electrical device," AIAA-2006-1203, *44th AIAA Aerospace Sciences Meeting and Exhibit*, Reno, NV, January 9-12 (2006).

8. C.L. Enloe, T.E. McLaughlin, R.D. VanDyken, K.D. Kachner, E.J. Jumper and T.C. Corke, "Mechanisms and responses of a single dielectric barrier plasma actuator: Geometric effects," *AIAA Journal* 42(3), 595-604 (2004).

9. C.L. Enloe, T.E. McLaughlin, R.D. VanDyken, K.D. Kachner, E.J. Jumper and T.C. Corke, "Mechanisms and responses of a single dielectric barrier plasma actuator: Plasma morphology," *AIAA Journal* 42(3), 589-594 (2004).

10. J.W. Gregory, C.L. Enloe, G.I. Font and T.E. McLaughlin, "Force production mechanisms of a dielectric-barrier discharge plasma actuator," AIAA-2007-185, *45th AIAA Aerospace Sciences Meeting and Exhibit*, Reno, NV, January 8-11 (2007).

11. C.O. Porter, J.W. Baughn, T.E. McLaughlin, C.L. Enloe and G.I. Font, "Plasma actuator force measurements," *AIAA Journal* 45 (7), 1562-1570 (2007).

12. W. Shyy, B. Jayaraman and A. Andersson, "Modeling of glow discharge-induced fluid dynamics," *Journal of Applied Physics* 92(11), 6434-6443 (2002).

13. D.M. Orlov and T.C. Corke, "Numerical simulation of aerodynamic plasma actuator effects," AIAA-2005-1083, *43rd AIAA Aerospace Sciences Meeting and Exhibit*, Reno, NV, January 10-13 (2005).

14. G.I. Font, “Boundary layer control with atmospheric plasma discharges,” AIAA-2004-3574, *40th AIAA/ASME/SAE/ASEE Joint Propulsion Conference and Exhibit*, Fort Lauderdale, FL, July 12-14 (2004).

15. D.V. Gaitonde, M.R. Visbal and S. Roy, “Control of flow past a wing section with plasma-based body forces,” AIAA-2005-5302, *36th AIAA Plasmadynamics and Lasers Conference*, Toronto, Canada, June 6-9 (2005).

16. S. Roy and C.C. Wang, “Plasma actuated heat transfer,” *Applied Physics Letters* 92, 231501 (2008).

17. C.C. Wang and S. Roy, “Electrodynamic enhancement of film cooling of turbine blades,” *Journal of Applied Physics* 104, 073305 (2008).

18. C.C. Wang and S. Roy, “Plasma actuated film cooling of a flat plate,” AIAA-2009-0679, *47th AIAA Aerospace Sciences Meeting*, Orlando, FL, January 5-8 (2009).

19. S. Roy and D. Gaintonde, “Force interaction of high pressure glow discharge with fluid flow for active separation control,” *Physics of Plasmas* 13, 023503 (2006).

20. D.V. Gaitonde, M.R. Visbal and S. Roy, “A coupled approach for plasma-based flow control simulations of wing sections,” AIAA-2006-1205, *44th AIAA Aerospace Sciences Meeting and Exhibit*, Reno, NV, January 9-12 (2006).

21. K.P. Singh and S. Roy, “Force approximation for a plasma actuator operating in atmospheric air,” *Journal of Applied Physics* 103, 013305 (2008).

22. S. Roy and C.C. Wang, “Bulk fluid modification with horseshoe and serpentine plasma actuator,” *Journal of Physics D: Applied Physics* 42, 032004 (2009).

23. S. Roy, “Flow actuation using radio frequency in partially ionized collisional plasmas,” *Applied Physics Letters* 86, 101502 (2005).

24. A.V. Likhanskii, M.N. Shneider, S.O. Macheret and R.B. Miles, “Modeling of dielectric barrier discharge plasma actuator in air,” *Journal of Applied Physics* 103, 053305 (2008).

25. K.P. Singh and S. Roy, “Modeling plasma actuators with air chemistry for effective flow control,” *Journal of Applied Physics* 101, 123308 (2007).

26. K.P. Singh and S. Roy, “Force generation due to three-dimensional plasma discharge on a conical forebody using pulsed direct current actuators,” *Journal of Applied Physics* 103, 103303 (2008).

27. K.H. Becker, K.H. Schoenbach and J.G. Eden, “Microplasmas and applications,” *Journal of Physics D: Applied Physics* 39, R55-R70 (2006).

28. L.D. Biborsch, O. Bilwatsch, S.I. Shalom, E. Dewald, U. Ernst and K. Frank, “Microdischarges with plane cathodes,” *Applied Physics Letters* 75, 25 (1999).

29. L.B. Hibbe, P Sichler, C. Schrader, N. Lucas, K.H. Gericke and S. Buttgenbach, "High frequency glow discharges at atmospheric pressure with micro-structured electrode arrays," *Journal of Physics D: Applied Physics* 38, 510-517 (2005).

30. T. Ono, D.Y. Sim and M. Esashi, "Micro-discharge and electric breakdown in a micro-gap," *Journal of Micromechanics and Microengineering* 10, 445-451 (2000).

31. J.M. Torres and R.S. Dhariwal, "Electric field breakdown at micrometre separations," *Nanotechnology* 10, 102-107 (1999).

32. E. Hourdakis, G.W. Bryant and N. M. Zimmerman, "Electrical breakdown in the microscale: Testing the standard theory," *Journal of Applied Physics* 100, 123306 (2006).

33. R.G. Longwitz, H. van Lintel, R. Carr, C. Hollenstein and P. Renaud, "Study of gas ionization schemes for micro devices," Proceedings of Transducers 01, 1258-1261, *11th International Conference on Solid-State Sensors and Actuators*, Munich, Germany, June 10-14 (2001).

34. F. Paschen, "Ueber die zum Funkenübergang in Luft, Wasserstoff und Kohlensäure bei verschiedenen Drucken erforderliche Potentialdifferenz," *Annalen der Physik* 273 (5), 69–75 (1889).

35. L.H. Germer, "Electrical breakdown between close electrodes in air," *Journal of Applied Physics* 30(1), 46-51 (1959).

36. F. Massines, N. Gherardi, N. Naude and P. Segur, "Glow and Townsend dielectric barrier discharge in various atmosphere," *Plasma Physics and Control Fusion* 47, B577–B588 (2005).

37. A. Sublet, C. Ding, J.L. Dorier, C. Hollenstein, P. Fayet and F. Coursimault, "Atmospheric and sub-atmospheric dielectric barrier discharges in helium and nitrogen," *Plasma Sources Science and Technology* 15, 627–634 (2006).

38. M.J. Kushner, "Modeling of microdischarge devices: Pyramidal structures," *Journal of Applied Physics* 95, 3 (2004).

39. M.J. Kushner, "Modeling of microdischarge devices: plasma and gas dynamics," *Journal of Physics D: Applied Physics* 38, 1633–1643 (2005).

40. J.P. Boeuf, L.C. Pitchforda and K.H. Schoenbach, "Predicted properties of microhollow cathode discharges in xenon," *Applied Physics Letters* 86, 071501 (2005).

41. Q. Wang, D.J. Economou and V.M. Donnelly, "Simulation of a direct current microplasma discharge in helium at atmospheric pressure," *Journal of Applied Physics* 100, 023301 (2006).

42. J. Choi, F. Iza, J.K. Lee and C.M. Ryu, "Electron and ion kinetics in a DC microplasma at atmospheric pressure," *IEEE Transactions on Plasma Science* 35, 5 (2007).

43. M.R. Radjenovic, J.K. Lee, F. Iza and G.Y. Park, “In Particle-in-cell simulation of gas breakdown in microgaps,” *Journal of Physics D: Applied Physics* 38, 950–954 (2005).

44. T. Farouk, B. Farouk, D. Staack, A. Gutsol and A. Fridman, “Simulation of DC atmospheric pressure argon micro glow-discharge,” *Plasma Sources Science and Technology* 15, 676–688 (2006).

45. L.J. Thomas and S.P. Bessman, “Micropump powered by piezoelectric disk benders,” *US Patent* 3963380 (1975).

46. N.T. Nguyen, X. Huang, and T.K. Chuan, “MEMS-micropumps : a review,” *Journal of Fluids Engineering* 124, 384-391(2002) .

47. D.J. Laser and J.G. Santiago, “A review of micropumps,” *Journal of Micromechanics and Microengineering* 14, R35–R64 (2004).

48. K.W. Oh and C.H. Ahn, “A review of microvalves,” *Journal of Micromechanics and Microengineering* 16, R13–R39 (2006).

49. O.M. Stuetzer, “Ion drag pressure generation,” *Journal of Applied Physics* 30, 7, 984–994 (1959).

50. W.F. Pickard, “Ion drag pumping. I. theory,” *Journal of Applied Physics* 34, 2, 246–250 (1963).

51. W.F. Pickard, “Ion drag pumping. II. theory,” *Journal of Applied Physics* 34, 2, 251–258 (1963).

52. A. Richter and H. Sandmaier, “An electrohydrodynamic pump,” *Proceedings of IEEE MEMS’90*, 99-104 (1990).

53. A. Richter, A. Plettener, K.A. Hofmann, and H. Sandmaier, “Electrohydrodynamic pumping and flow measurement,” *Proceedings of IEEE MEMS’91*, 271-276 (1991).

54. S.H. Ahn and Y.K. Kim, “Fabrication and experiment of a planar micro ion drag pump,” *Sensors and Actuators A* 70, 1-5 (1998).

55. J. Darabi, M. Rada, M. Ohadi, and J. Lawler, “Design, fabrication, and testing of an electrohydrodynamic ion-drag micropump,” *Journal of Microelectromechanical Systems* 11, 6, 684-690 (2002).

56. J. Darabi and C. Rhodes, “CFD modeling of an ion-drag micropump,” *Sensors and Actuators A* 127, 94-103 (2006).

57. G. Fuhr, T. Schnelle, and B. Wagner, “Traveling wave-driven microfabricated electrohydrodynamic pumps for liquids,” *Journal of Micromechanics and Microengineering* 4, 217-226 (1994).

58. G. Fuhr, R. Hagedorn, T. Muller, W. Benecke, and B. Wagner, "Microfabricated electrohydrodynamic (EHD) pumps for liquids of higher conductivity," *Journal of Microelectromechanical Systems* 3, 141-145 (1992).

59. J.W. Choi and Y.K. Kim, "Micro electrohydrodynamic pump driven by traveling electric fields," *Proceedings of the IEEE Industrial Applications Conference*, Conference Record, 1480–1484 (1995).

60. T. Bourouina, A. Bosseboeuf, and J.P. Grandchamp, "Design and simulation of an electrostatic micropump for drug-delivery applications," *Journal of Micromechanics and Microengineering* 7, 186-188 (1997).

61. P. Bruschi, A. Diligenti, and M. Piotto, "Micromachined gas flow regulator for ion propulsion systems," *IEEE Transactions on Aerospace and Electronic Systems* 38, 3, 982-988 (2002).

62. S. Roy, "Method and apparatus for efficient micropumping," *International Publication number* PCT WO 2009/015371S (2007).

63. H. Kumar and S. Roy, "Multidimensional hydrodynamic plasma-wall model for collisional plasma discharges with and without magnetic field effects," *Physics of Plasmas* 12, 093508 (2005).

64. I.A. Kossyi, A.Y. Kostinsky, A.A. Matveyev, and V.P. Silakov, "Kinetic scheme of the non-equilibrium discharge in nitrogen-oxygen mixtures," *Plasma Sources Science and Technology* 1, 207-220 (1992).

65. S.T. Surzhikov and J.S. Shang, "Two-component plasma model for two-dimensional glow discharge in magnetic field," *Journal of Computational Physics* 199, 437-464 (2004).

66. Panton, R.L. *Incompressible Flow*. 3rd ed. New York: Wiley, 2005.

67. *Fluent 6.3 User Guide*. New Hampshire: Fluent Inc, 2006.

68. B.E. Launder and B.I. Sharma, "Application of the energy dissipation model of turbulence to the calculation of flow near a spinning disc," *Letters in Heat and Mass Transfer* 1(2), 131-138 (1974).

69. J.C. Maxwell, "On stresses in rarefied gases arising from inequalities of temperature," *Philosophical Transactions of the Royal Society of London* 170, 231 (1879).

70. S. Roy, R. Raju, H.F. Chuang, B.A. Kruden and M. Meyyappan, "Modeling gas flow through microchannels and nanopores," *Journal of Applied Physics* 93, 8 (2003).

71. M von Smoluchowski, "Ueber Warmeleitung in Verdunnten Gasen," *Annalen der Physik und Chemie* 64, 101 (1898).

72. Carey, G.F, and J.T. Oden. *Finite Elements: A Second Course - Volume 2*. Prentice Hall, 1981.

73. Baker, A.J., and D.W. Pepper. *Finite Element 1-2-3*. Columbus: McGraw Hill, 1991.

74. Atkinson, K.E. *An Introduction to Numerical Analysis*. 2nd ed. New York: Wiley, 1989.

75. Y. Saad and M.H. Schultz, "GMRES: a generalized minimal residual algorithm for solving nonsymmetric linear systems," *SIAM Journal on Scientific and Statistical Computing* 7, 3 (1986).

76. X.Z. Zhang and I. Hassan, "Film cooling effectiveness of an advanced-louver cooling scheme for gas turbines," *Journal of Thermophysics and Heat Transfer* 20, 4, 754-64 (2006).

77. D.V. Gaitonde, M.R. Visbal and S. Roy, "Three-dimensional plasma-based stall control simulations with coupled first-principles approaches," Keynote Lecture FEDSM2006-98553, *ASME Joint U.S.-European Fluids Engineering Summer Meeting*, Miami (2006).

78. M.R. Visbal, D.V. Gaitonde and S. Roy, "Control of transitional and turbulent flows using plasma-based actuators," AIAA-2006-3230, *36th AIAA Fluid Dynamics and Flow Control Conference*, San Francisco, June (2006).

79. S. Roy and D. Gaitonde, "Radio frequency induced ionized collisional flow model for application at atmospheric pressures," *Journal of Applied Physics* 96, 51 (2004).

80. S.B. Wang and A.E. Wendt, "Sheath thickness evaluation for collisionless or weakly collisional bounded plasmas," *Transactions on Plasma Science* 25, 5 (1999).

81. D. Lee, J.M. Park, S.H. Hong and Y. Kim, "Numerical simulation on mode transition of atmospheric dielectric barrier discharge in helium-oxygen mixture," *IEEE Transactions on Plasma Science* 33, 2 (2005).

82. C.C. Wang and S. Roy, "Microscale plasma actuators for improved thrust density," *Journal of Applied Physics* 106, 013310 (2009).

83. C.C. Wang and S. Roy, "Flow shaping using three-dimensional microscale gas discharge," *Applied Physics Letters* 95, 081501 (2009).

84. C.C. Wang and S. Roy, "Three-dimensional simulation of a micro plasma pump," *Journal of Physics D: Applied Physics* 42, 185206 (2009).

BIOGRAPHICAL SKETCH

Chin-Cheng Wang was born in 1979 in Taipei, Taiwan. He received his Bachelor of Science degree in vehicle engineering from National Taipei University of Technology in 2001. He earned his M.S. degree in mechanical engineering from the National Taiwan University of Science and Technology in 2003. During 2003-2005, he served in the Army for his mandatory military service. After the service he worked for a year as an engineer at Motor Company. Since 2006, he has been working towards the doctorate here at the University of Florida under Dr. Subrata Roy. His research areas are microscale discharge, plasma-based active flow control, plasma-fluid interaction, fluid-structure interaction, micropumps, micropropulsion, microchannel flow, film cooling, plasma sterilization, plasma sheath physics, finite element method, granular flow, and computational fluid dynamics.